

The detection of deformation on vegetated dikes using InSAR

Master thesis

Joost Driebergen

TU Delft
Geoscience and Remote Sensing



The detection of deformation on vegetated dikes using InSAR

Master thesis

by

Joost Driebergen

Student number: 4509153
Thesis committee: Prof. dr. ir. R.F. Hanssen, TU Delft, Graduation Professor
Dr. ir. F.J. van Leijen, TU Delft, Supervisor
Dr. A. Askarinejad, TU Delft, External Examiner

Contents

Nomenclature	v
Preface	ix
Summary	xi
1 Introduction	1
1.1 Research objective	2
1.2 Methodology	2
1.3 Outline	3
2 Background	5
2.1 Dikes	5
2.1.1 Geology	6
2.1.2 Construction of a dike	6
2.1.3 Dike failure mechanisms.	7
2.1.4 Dike inspection	8
2.1.5 Measuring deformation	9
2.2 Radar interferometry	11
2.2.1 Geometry	11
2.2.2 Measurements	12
2.2.3 Resolution and pixel posting.	13
2.2.4 Interferometric SAR	14
2.2.5 Influence of phase contributors	16
3 Time Series interferometry	17
3.1 Persistent Scatterer Interferometry	18
3.2 Distributed Scattering Interferometry.	19
3.2.1 Adaptive multilooking	20
3.2.2 Computational performance.	21
3.2.3 Complex coherence	22
3.2.4 Small Baseline Subset Algorithm.	26
3.2.5 SqueeSAR	27
3.2.6 Advanced DSI technique.	29
3.3 Summary	31
4 SAR Data analysis	33
4.1 Case study	33
4.1.1 TerraSAR-X data	35
4.1.2 Radarsat-2	37
4.2 Double differences	39
4.3 Accessing spatial correlation in data	41
5 Methodology	43
5.1 Coherent interferogram selection.	43
5.2 Estimating relative deformation.	45
5.2.1 Observation equation	45
5.2.2 Testing the methods	48
5.3 Method evaluation	49

6	Results	51
6.1	State of the art	51
6.2	Statistical Homogeneous Pixel selection	52
6.3	Application on TerraSAR-X data.	55
6.3.1	Periodogram VS Least-Squares.	57
6.3.2	Comparison of interferogram selection methods	63
6.3.3	Increasing multilook window	66
6.3.4	Equivalent Single Master.	68
6.4	Application on Radarsat-2 data	70
6.5	Discussion	73
7	Conclusions and Recommendations	77
7.1	Conclusions.	77
7.2	Recommendations	80
	Bibliography	83

Nomenclature

List of acronyms

AD-test	Anderson Darling test
APS	Atmospheric Phase Screen
DePSI	Delft Persistent Scatterer Interferometry
DORIS	Delft Object-Oriented Radar Interferometric Software
DS	Distributed Scatterer
DSI	Distributed Scatterer Interferometry
ESM	Equivalent Single Master
GLRT	Generalized Likelihood Ratio Test
GPS	Global Positioning System
GRD	Ground Range Detected
HS	High Resolution SpotLight
ILS	Integer Least-Squares
InSAR	Satelite Radar Interferometry
KS-test	Kolmogorov Smirnov test
LOS	Lign Of Sight
LSQ	Least-Squares
MEMS	Micro-ElectroMagnetic Systems
MRM	Mean Reflectivity Map
NWP	Numerical Weather Prediction
PCA	Principle Components Analysis
PRF	Pulse Repitition Frequency
PS	Point Scatterer
PSC	Persistent Scatterer Candidates
PSI	Persistent Scatterer Interferometry
pdf	probability density function
RAR	Real Aperture Radar
RMSE	Root Mean Square Error
SAR	Synthetic Aperture Radar

SBAS	Small Baseline Subset Algorithm
SHP	Statistical Homogenous Pixels
SL	SpotLight
SLC	Single Look Complex
SM	StripMap
SNR	Signal to Noise Ratio
SRTM	Shuttle Radar Topography Mission
ST	Staring Spotlight mode
StaMPS	Stanford Method for PS
STC	Spatial Temporal Consistency
SVD	Singular Value Decomposition
WRF	Weather Research and Forecast

List of symbols

α_h	Satellite heading angle
ψ	Phase of the complex phasor
λ	Wavelength [m]
θ	Look angle with respect to the nadir direction
τ	Pulse length [μ s]
η	Spatial temporal consistency [mm]
σ_ϕ	Phase dispersion
σ_0	Standard deviation of the motion of scatterers in LOS direction per unit of time
σ_A	Standard deviation of the amplitude
σ_r	Standard deviation of the motion of scatterers in LOS direction
μ_a	Mean of the amplitude
$ \gamma $	Temporal coherence
γ^x	Phase stability parameter
γ_{ij}	Complex coherence between observations i and j
$\hat{\gamma}_{ij}$	Estimate of the complex coherence
ρ	Correlation coefficient
Ω	All pixels which are defined as SHP
$\phi_{DInSAR_{model}}^{i,k}$	Modeled phases
$\phi_{DInSAR_{obs}}^{i,k}$	Phase observations
Δa	Azimuth resolution

ΔH_{res}	Residual topographic height [m]
Δr	Range resolution
ΔV_{lin}	Relative linear deformation velocity with respect to closest PS [mm/year]
A	Amplitude of the complex phasor
\bar{A}	Estimated mean amplitude
A_{nm}^2	Test statistic for the Anderson Darling test
B_{\parallel}	Parallel component of the baseline [m]
B_{\perp}	Perpendicular component of the baseline [m]
B_T	Temporal baseline [years]
c	Speed of light
D	Physical length of the antenna
D_{LOS}	Displacement in the Lign Of Sight
d_a	Azimuth posting
d_r	Range posting
F_s	Sampling frequency in range direction [Hz]
F_{DC}	Difference in Doppler centroid
H	Topographic height [m]
H_0	Null hypothesis
H_a	Alternative hypothesis
j	Imaginary number
K_{σ}	Decorrelation rate [days]
L	Number of SHP
M	Number of interferograms
m	Size of the tested sample
m_v	Local deformation velocity gradients [mm/year/pixel]
m_h	Residual DEM gradients [m/pixel]
N	Amount of SLC images
n	Size of the reference sample
P	Complex phasor
Q_A	Approximation for the phase dispersion σ_v
Q_{yy}	Sample covariance matrix
q	Decorrelation rate [days]
R	Distance from the satellite to the Earth
$ T_{r,t} $ test	Test statistic for reference pixel r and tested pixel t for the Kolmogorov-Smirnov test
v	Velocity of satellite platform

List of functions and operators

$\{\}^*$	Complex conjugate
$\{\}^{-1}$	Inverse
$\{\}^T$	Transpose
$ \cdot $	Absolute value
$W\{\}$	Wrapping operator
$d(\cdot, \cdot)$	Distance operator (euclidean)
$E\{\}$	Expectation operator
exp	Exponential operator
$Im(\cdot)$	Complex part
min	Minimum operator
$Re(\cdot)$	Real part
$\Gamma(\cdot)$	Gamma function
K_{L-1}	Modified Bessel function of the third kind
$Li_2(\cdot)$	Euler's dilogarithm
$argmin_x(\cdot)$	Argument which minimizes a certain parameter

•

Preface

This thesis is the result of almost a year of research on the quest to estimate deformation time series on grass-covered dikes. Many ups and downs have led to the completion of the Geoscience and Remote Sensing master at the faculty of Civil Engineering and Applied Earth sciences from the TU Delft university. In particular I have learned a lot about the usage of large data sets obtained from satellites to estimate geophysical parameters of the Earth. This would not have been possible without my graduation committee, to which I would like to express my gratitude. I would like to thank my daily supervisor Freek van Leijen for his guidance in the InSAR processing technique. My gratitude also goes to professor Ramon Hanssen, who has asked critical questions which I hope have led to a higher quality of the thesis. I want to thank Amin Askarinejad for providing feedback to my thesis and for asking questions of how to relate the estimated deformation to the physical processes of dikes. Furthermore, I would like to thank my family, friends, colleagues and fellow students who have supported me during my studies. Thanks for motivating me in difficult times and for the necessary distractions. Thanks for the many coffees we drank while complaining about daily difficulties in our graduation projects.

Joost Driebergen
Delft, Februari 5, 2019

Summary

In the Netherlands, 17000 km of dikes are used to protect the 3.9 million people who live below sea level against the rising water. To ensure the safety of the dikes it is important to constantly monitor parameters which can indicate a developing failure mechanism. One indicator of a developing failure mechanism is deformation, and can be estimated by using Radar interferometry (InSAR), a remote sensing technique which can provide mm accuracy of deformation. Monitoring of urban areas is facilitated by InSAR time series methodologies such as Persistent Scatterer Interferometry (PSI), which focuses on coherent reflections of Point Scatterers (PS). While this technique is successfully applied on urban areas, objects in rural areas are often not coherent over a longer time frame. These objects are called Distributed Scatterers (DS) and are strongly affected by temporal decorrelation, but may contain coherent information for interferograms with small temporal baselines. To extract this coherent information, several Distributed Scatterer Interferometry (DSI) methods have been developed such as SBAS and SqueeSAR. These DSI methodologies have mainly been applied to large homogeneous fields where large areas can be used for complex multilooking to reduce noise. However, a dike is relatively small in width (only covering a few radar resolution cells) but elongated in the other direction which makes it more difficult to reduce noise. Not much research has been done to estimate deformation time series on grass-covered dikes, but is important because it can be an indicator of a developing failure mechanism.

In this research project, a methodology is presented to detect coherent DS on the vegetated part of a dike and to estimate their deformation time series. An extensive review of existing time series InSAR techniques is performed with an emphasis on DS. To reduce the temporal decorrelation noise in DS, a spatially adaptive window can be used for multilooking. Different methods are presented to find Statistical Homogeneous Pixels (SHP), which compare two Empirical Cumulative Distribution Functions of the amplitude to detect pixels with similar amplitude behavior. The coherence matrix, which follows from the complex multilooking operation, contains a quality indicator for each interferogram which can be used to give a weight to each observation.

The developed methodology in this thesis is based on two pillars. First, for each pixel on the dike, the interferometric phase of the closest PS (as obtained by a PSI analysis) is subtracted to reduce terms such as the atmosphere, orbital errors and residual topography. Second, several threshold methods have been applied on the coherence matrix to select coherent interferograms and to exclude interferograms which have a coherence below a certain threshold. The observed phases (relative to the closest PS) are related to a linear deformation model. This observation equation is then solved with a periodogram method and Least Squares method. To assess whether an estimated deformation time series is significant, three criteria are imposed on the time series. First, the Root Mean Square Error (RMSE) of the estimation with respect to the observed phases must be lower than or equal to 1.25 radians (which is equal to 3 mm for TerraSAR-X). Secondly, more than 60 interferograms must be selected from the coherence matrix. Lastly, the distance with respect to the reference PS must be larger than six meters for an estimation to be significant. This is because of oversampling and pixel posting, nearby pixels are correlated.

As a case study, a part of the Marken island in the Netherlands is analyzed with the developed methodology. Both TerraSAR-X (X-band) data and Radarsat-2 data (C-band) were used to investigate whether a larger wavelength could decrease the decorrelation of the phases. The results demonstrate that, for this case study, it is possible to detect coherent DS on the vegetated part of the dike. However, the extent to which these points reach is limited and future work is needed to further investigate this research topic.

Introduction

Dikes play a crucial role in protecting the Netherlands, which is for a large part situated below sea level. Since 3.9 million people live below sea level (which is likely to increase to 6.6 million if the sea level increases with 1 meter) (Hoes and Hut, 2018), it is important to know how safe our storm surges and dikes are. The deformation of a dike may be an indicator of a developing failure mechanism (sliding of the dike will lead to horizontal deformation, piping can cause vertical deformation, to name a few), as has been shown by Dentz et al. (2006) and Özer et al. (2016).

Conventional techniques to monitor water defense structures such as dikes often relies on (yearly) visual inspections, performing in situ measurements if necessary. Although visual inspections can lead to detection of weak parts of the dike, it cannot detect the slowly changing subsidence of a dike which eventually can lead to dike failure. Furthermore, the larger spatial extent of flood defenses (17691 km), makes it labor intensive and time consuming to perform inspection. A supplementary technique to monitor dikes is Satellite Radar Interferometry (InSAR). With this technique it is possible to obtain high precision (mm accuracy) deformation estimates on a large scale with frequent observations.

This active remote sensing technique sends out an electromagnetic wave and measures both the amplitude and the phase of the backscattered signal. If, at a later time, a second measurement is performed, it is possible to estimate the deformation signal (after other phase contributions are estimated and removed) based on the phase difference between the two measurements. A comprehensive overview is given by Hanssen (2001). There are, however, a couple of other sources which interfere with the deformation signal. Because of different states of the atmosphere between two acquisitions, a residual phase will be present in the interferogram. Another problem is that scattering characteristics of the measured resolution cell changes over time which leads to temporal decorrelation. An approach which attempts to deal with the above described limitations is called Persistent Scatterer Interferometry (PSI) (Ferretti et al., 2000, 2001). This technique makes use of Point Scatterers (PS) which stay coherent over time to estimate the deformation. Here a stack of radar images is used to estimate deformation time series for a given area, which allows the atmospheric error to be removed since it is temporally uncorrelated (Ferretti et al., 2000).

This technique is currently used to monitor the deformation of hydraulic structures and dikes. Hanssen and van Leijen (2008a), for example, used PSI to monitor dikes around the Waddenzee and IJsselmeer and found coherent reflections for more than 90 percent of the primary water defense systems. However, as they point out, a reason for not having a coherent scatterer is perhaps the consequence of a major disturbance.

More recently, Ozer et al. (2018) investigated the possibility to monitor dikes with PSI. Using coherent points in time, it was possible to estimate deformation time series for different dikes in the Netherlands. However, a limitation of the PSI technique is that it will not work if there are no PS on the desired object (i.e the decorrelation time is short) (Morishita and Hanssen, 2015a). In rural areas, pixels often do not show a stable reflection over time but show a distributed scattering behavior. These pixels are called Distributed Scatterers (DS) and, while not coherent over the whole time frame, may contain coherent information for small temporal baselines. Methods which use these DS to extract coherent information are called Distributed Scatterer Interferometry (DSI) methods. An example is shown by Ferretti et al. (2011) who showed in their paper an algorithm (SqueeSAR) in which they processed DS together with PS to estimated Line Of Sight (LOS) deformation time series for a mountainous area with rough topography and vegetation. Here they use statistical homogeneous pixels to reduce noise and to estimate the coherence matrix (a square matrix with correlation

coefficients for the observations) which is used to give a weight to each observation. Other examples show the LOS deformation of pasture on peat soil (Morishita and Hanssen, 2015a) and a subsiding agriculture area around a salt mining area (Samiei-Esfahany, 2017). Above mentioned examples use large groups of pixels to extract statistical information of the low-coherent pixels. However, the area over which to average pixels may be smaller for dikes and therefore the question is if a similar approach can be taken to predict deformation of vegetated dikes.

1.1. Research objective

Using contemporary InSAR methodologies (such as PSI, SqueeSAR), it is already possible to estimate deformation time series of good reflecting objects on dikes. However, not much research has been done yet to estimate deformation on the grass-covered part of the dike. Therefore, the goal of this thesis is to answer the main research question:

How can InSAR techniques be optimized to detect coherent distributed scatterers and estimate their deformation time series on grass-covered dikes?

To answer the research question, several steps are assessed which will be presented as sub-questions. First, the amount of noise in so-called double differences is investigated to assess whether there is still coherent information over short arcs. In the second sub-question the extent of the spatial correlation, introduced by oversampling and pixel posting, is quantified which has to be taken into account when interpreting the results. The third sub-question deals with finding the optimal method for finding Statistical Homogeneous Pixels (SHP). Different selection methods for finding coherent interferograms are compared with each other to obtain the best selection method (sub-question four). The fifth question deals with comparing, and selecting the best method to estimate relative deformation. In the sixth sub-question, it is investigated whether the use of a larger wavelength is beneficial for the results.

The main research question is therefore subdivided into six sub-questions.

1. What is the magnitude of the phase noise in short arc double differences?
2. Over what length are pixels spatially correlated due to processing steps
3. What is the best statistical method to find Statistical Homogeneous Pixels ?
4. How can coherent interferograms be selected from the coherence matrix?
5. Which method is best suited for the estimation of relative deformation?
6. What is the influence of using a C-band sensor compared to a X-band sensor?

1.2. Methodology

The research is conducted by performing different steps, starting with a background review. Some basics principles about dikes and failure mechanisms will be provided as well as information about Radar Interferometry (InSAR). This review is extended by presenting different time series InSAR techniques, both Persistent Scatterer Interferometry (PSI) and Distributed Scatterer Interferometry (DSI). This review will be build upon in the developed methodology. The first two sub-questions will be answered by using existing mathematical techniques. By using results of a DePSI (Delft PSI, van Leijen (2014)) analysis, the magnitude of the noise in the double differences is analyzed. The extent of the spatial correlation is quantified by computing an empirical variogram. For sub-question three until six, software is written in Matlab. The main function of the software is to fit a predefined deformation model to the phase differences between a pixel and its closest PS. Different statistical tests can be used for the selection of SHP, which is the basis for answering sub-question three. The selected SHP form the basis for the computation of the coherence matrix. Based on the coherence matrix, then, the user can specify different selection methods to select coherent interferograms which will be used for the estimation of relative deformation. Two methods will be proposed to estimate relative deformation. These methods will be compared with each other based on some goodness-of-fit parameter.

The developed methodology will be applied on a case study on the Marken island by using two data sets, acquired by the TerraSAR-X and Radarsat-2 missions. The TerraSAR-X data set covers the period February 2009 until January 2016, revisiting every 11 days. This satellites operates at X-band (wavelength 0.031

m) and has resolution cells of 1.2 m in slant range and 3.3 m in azimuth direction in StripMap (SM) mode. The Radarsat-2 satellite is used to investigate the influence of a larger wavelength (C-band, 0.055 m) on the results. For the Radarsat-2 satellite, data is available from March 2015 up to March 2018 with a revisit time of 24 days. The resolution is 2.8 m in azimuth and 4.6 m in slant range direction in Extra Fine (XF) mode. For both data stacks, pre-processing (coregistration, flat earth phase removal, oversampling) is done using the DORIS (Delft Object-Oriented Radar Interferometric Software) InSAR processor. Since the time span of both data sets is different, the results cannot be compared directly with each other.

The new methodology is compared with existing software called DS Delft (Samiei-Esfahany, 2017). Here an Equivalent Single Master step is performed on the multi-looked data to further reduce the noise. Compared to the developed methodology, in which a deformation model was used to unwrap the phases, the daisy chain phases are unwrapped by taking the cumulative sum over time. Benefits of this unwrapping is that the true phase evolution is obtained, the risk being unwrapping errors. These unwrapped phase time series are then used for further analyses. One point which is investigated is whether the assumed deformation model in the developed methodology is correct. Another point is that it is investigated whether the temperature is correlated to the phase time series. This is done by referring the pixels to a nearby building for which it is assumed that the deep foundation is not influenced that much by temperature.

1.3. Outline

The first part of this thesis consists of a comprehensive literature review, which is divided into two chapters. In **Chapter 2**, some background information is presented about dikes and Radar Interferometry. The construction of a dike is discussed as well as several failure mechanisms. The purpose of the Radar Interferometry background is to lay a foundation which is build upon in the next chapters. Here the geometry of a (satellite) radar imaging system is presented as well as the different contributions of the interferometric (wrapped) phase. Next, in **Chapter 3**, time series interferometry methodologies are discussed which use a stack of image to estimate deformation time series. The chapter is split up into two parts, Persistent Scatter Interferometry (PSI) and Distributed Scatter Interferometry (DSI). Important terms in this chapter are *Statistical Homogenous Pixels* and *Complex coherence*. **Chapter 4** investigates the amount of noise in double differences and accesses the spatial correlation between pixels originating from data processing. Two data stacks will be used, TerraSAR-X and Radarsat-2, and will be applied on a crop of the Marken Island.

A developed methodology to detect coherent distributed scatterers and estimate their relative deformation time series is presented in **Chapter 5**. Two methods are proposed, one using a Least-Squares approximation while the other uses a periodogram fit. Both methods require coherent interferograms as input which are obtained by applying a threshold on the coherence matrix. The two methods are validated by comparing the results with a PSI analysis. Finally, an approach is presented to compare the different configurations with each other. In **Chapter 6**, the results of the developed methodology applied on the case study are presented. First, the Least-Squares method and periodogram method are compared with each other. Next, the best method to find coherent interferograms is presented together with the optimal threshold (applied on the coherence matrix). To analyze the influence of a larger wavelength, Radarsat-2 data is used. Conclusions and recommendations are presented in **Chapter 7**. Answers to the research sub-questions are made which will lead to the answering of the main research question. Following the conclusions, recommendations are presented for further research.

2

Background

This chapter provides some background information about both dikes and InSAR processing techniques. Since the objective of this thesis is to estimate deformation on vegetated dikes, it is important to understand how a dike is built as well as how a dike can fail. Some of these failure mechanisms can lead to deformation of the dike. Several techniques to measure deformation are explained in Section 2.1, of which the technique Radar Interferometry is further elaborated upon in Section 2.2.

2.1. Dikes

The earliest indications of dikes in the Netherlands date from around the late iron age (around 700 BC) (Dutchdikes.net, 2018). Small dikes with a height of around 70 cm constructed of peat sods were used to protect the land. It was a few thousand years later (1200-1500 period) that the effect of subsidence and rising sea levels meant that sea dikes were necessary to protect the inland from the rising sea level. In the period between 1500 and 1800 (the golden age), the population of the Netherlands increased rapidly and became much more prosperous which led to the construction of large scale hydraulic structures. However, this prosperity came to an abrupt end because the advent of the naval shipworm led to rotten wooden structures. This disastrous damage led the dike builders to use stone for the dike revetment. Furthermore, the invention of concrete in 1842 opened up a lot more possibilities of building new types of water defense structures.

In 1953, during the morning of 31 January, a combination of a storm, spring tide and high water levels in the rivers led to the flooding of 1650 square kilometers of land in the province of Zeeland (Southern part of the Netherlands). The 1800 fatalities were the incentive for the government to establish the Deltacommissie which had to make sure a disaster as in 1953 would never occur again. The Deltawerken, which were constructed after the 1953 storm surges, are a combination of 3 sluices, 6 dams and 5 storm surges were built to protect the provinces of Zeeland and South-Holland from the sea.

After extreme high river water levels in 1995 led to the evacuation of around 250.000 people, the attitude towards water protection changed. The nationwide project Ruimte voor de rivier changed the emphasis from strengthening and heightening the dikes towards providing more room for the river.

In the Netherlands there are about 3700km of primary water defenses (to protect land from water from the north-Sea, big rivers and lakes) and 14000 km of secondary water defenses (to protect the land from inland water coming from smaller rivers and lakes) (Infomil.nl, 2018). There are different types of water defense structures such as dunes, dams, sluices, storm surges and dikes. Since the goal of this thesis is to measure



Figure 2.1: Mayor flood event (Watersoondramp) in the province of Zeeland.
<https://historiek.net/watersnoodramp-1953/6913/>

deformation of dikes, this type of defense structure will be discussed somewhat more. In the next section the sub-surface of the Netherlands will be discussed, which is important for the development of (some) failure mechanisms.

2.1.1. Geology

The different soil types in the Netherlands can be subdivided in sea clay, river clay, sand, loess and peat (Figure 2.2). The dutch sea clay formed in the Holocene (about 10 000 years ago). The rising sea level as a result of the melting land ice, initiated the sinking of small particles in the sea which caused a clay layer to form on large areas near the Dutch coast. River clay is formed if, after a river flooding, the small sediment particles sink to the bottom and pile up to form a clay layer. The dutch sand landscape has been formed during the Pleistocene (2.58 million years until 10000 years ago) and is primary formed by river and glacier deposits.

Peat soil is formed by organic material which is partially decayed. The surface on which a dike is build can be of influence on the failure mechanism of a dike. Many of the dikes in the Netherlands were build centuries ago on the natural subsurface which is on some places very soft (van Geel et al., 1982). Fern et al. (2015) found that the stiffness of the subsoil played an important role in the failure mechanism of the dike (stiff subsoils allowed the dike to slide and soft subsoils lead to an excessive deformation which lead to diffused shear zones). In the next section, the construction of a dike is discussed.

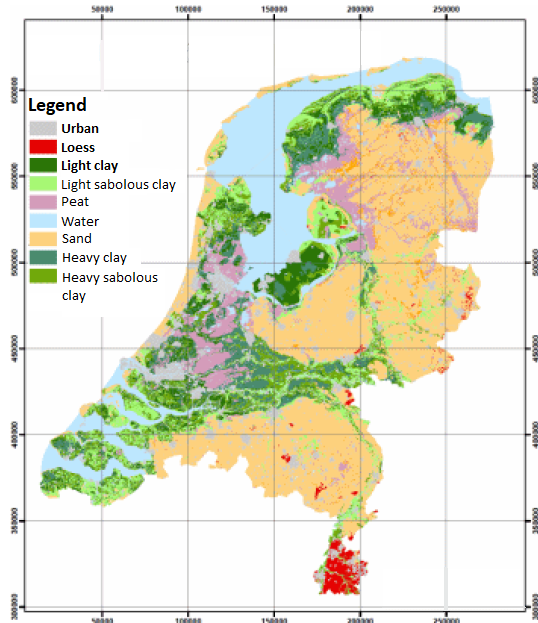


Figure 2.2: Different types of ground in the Netherlands www.wur.nl/nl/show/Grondsoortenkaart.htm

2.1.2. Construction of a dike

Depending on whether a dike has to protect water from the sea (sea dike) or from the river (river dike), the construction of the dike may be different. A cross section of a typical sea dike is shown in Figure 2.3. In the Netherlands, usually the dike consists of a inner sand core covered by a clay layer of about 0.5 m thick (van Hoven et al., 2010). A sea dike has to be able to withstand high water as well as wave induced impact. Because of the wave impact, the outer slope of the sea dike needs a revetment to protect it from the waves. Because coastal dikes are attacked by different water levels and considerable wave impact, the outer slope of the dike is relatively small. Usually a revetment is present at the height were the waves attack under a normal water level (to protect the dike against erosion) and on the height were the waves attack during a storm surge. The revetment can for example be made from concrete blocks, asphalt or natural stone. The inner slope of the dike is in general not exposed to wave impact and therefore it is enough to provide the inner slope of the dike with grass-cover.

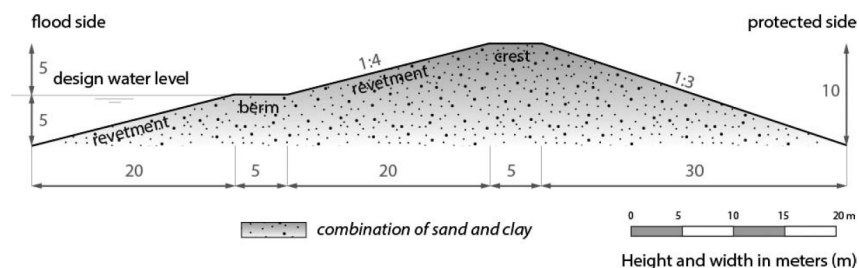


Figure 2.3: Typical cross section of a dutch sea dike (Jonkman et al., 2013). The outer slope can be steeper as compared to a sea dike because it is exposed to minor wave attack. The inner slope is usually smaller to keep the phreatic line inside the dike.

Contrary to coastal dikes, river dikes are exposed to a much slower varying water level and minor wave attack. Therefore the outer part of the dike can often be covered by grass, but sometimes revetment is necessary to protect the dike against erosion. The inner slope is in general quite gentle to be able to keep the phreatic line inside the dike. An example of a river dike is depicted in Figure 2.4.

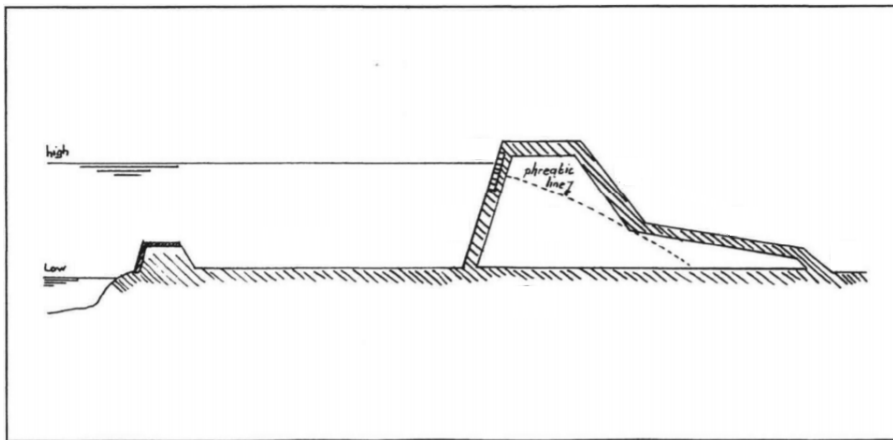


Figure 2.4: Typical cross section of a river dike (H.J.Verhagen, 1998).

2.1.3. Dike failure mechanisms

The primary function of a dike is to protect the land on the inner side of the dike against the water on the outer side of the dike. There are different ways in which a dike can fail to function, which are called failure mechanisms.

In this section the different failure mechanisms of dikes will be summarized. The four most important failure mechanisms in the Netherlands are depicted in figure 2.5 (Vergouwe, 2015).



Figure 2.5: The four most common failure mechanisms of dikes in the Netherlands (Vergouwe, 2015) .

Wave overtopping (a) can damage the inner part of the dike which can lead to erosion of the dike crest which eventually can lead to dike failure. The incoming wave can lead to damage on the inner slope which

can lead to a scour hole which increases in depth with each incoming wave. Especially transitions from a slope to a horizontal surface seem to be more vulnerable as well as concrete structures in the dike such as staircases (H.Verheij et al., 2012).

As a result of long lasting flood waves, the inner slope of the dike may become unstable **(b)**. The load on the dike increases as a result of the saturation of the dike material, while the resistance decreases because of water pressure inside the dike (Kanning, 2005). If the load becomes higher than the resistance, the dike fails. Outer slope instability **(c)** can lead to dike failure when the revetment of the outer slope is damaged. This failure mechanism is especially relevant in coastal area's (Vergouwe, 2015). Failure due to piping **(d)** occurs when soil particles below the dike are washed out due to excessive seepage (Kanning, 2012). Because of the difference in water level, pressure on the inner part of the dike will result in water flow from below the dike. Sand flows out and a channel starts to develop until there is a connection between the inner and outer part of the dike, which is defined as piping failure. The consequences of piping are subsiding of the dike and eventually disintegration.

In the Netherlands, 1735 dike failures have been recorded between 1134 and 2006 caused by 338 events (Baars and van Kempen, 2009). The most common cause of a dike failure are storm surges. In the past also ice drift caused dike failures (especially in the little ice age between 1784 and 1861), but this has declined because the quality of the dikes improved and the temperature of the rivers has increased significantly (Baars and van Kempen, 2009). Historically, the most common failure mechanism is the failure of the inner slope protection caused by wave overflow and run-over which is responsible for 66 percent of the listed dike failures (Baars and van Kempen, 2009). At present, failure mechanisms such as piping are considered more dangerous because dikes are build much higher to withstand wave overflow and run-over. Furthermore, the pore pressure of dikes is higher because of the rising sea level and the subsiding land.

As droughts will possibly occur more frequently in the future because of the changing climate, dike failures caused by drought might occur more frequently. In 2003, a peat dike in the Netherlands near the village Wilnis failed after a very warm and dry summer (see Figure 2.6). Because of the drought, the specific weight of the peat was very low. This makes that the peat dike has a higher risk of being pushed to the side by the pressure of the water, which is called a horizontal sliding mechanism. (Baars, 2004).

To reduce the risk of a dike failure, it should be regularly inspected and maintenance should be carried out accordingly. In the next subsection the procedure of dike inspection in the Netherlands is explained.

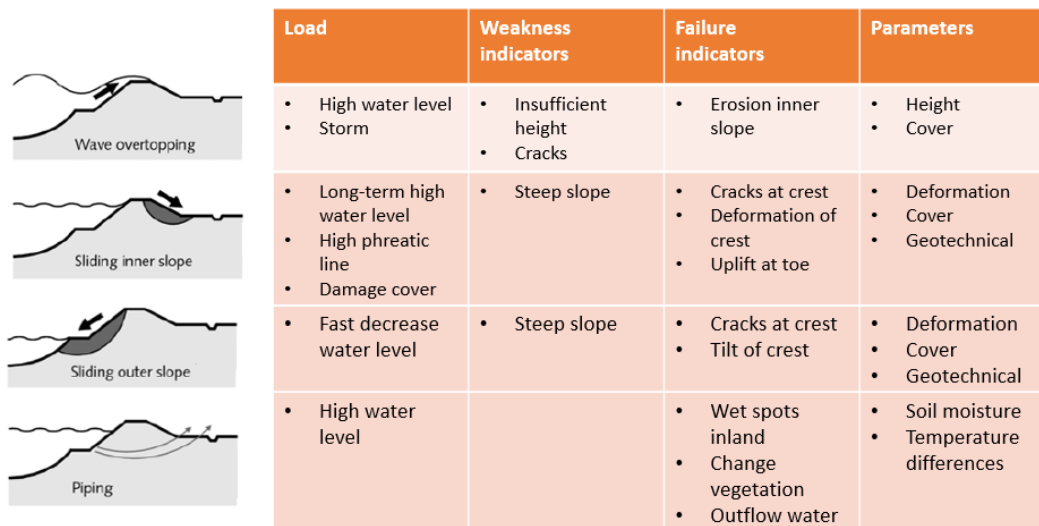


Figure 2.6: Wilnes failure of a peat dike in 2003.
[https://en.wikipedia.org/wiki/File:Failed_section_of_peat_levee_\(Wilnis,_August_2003\).jpg](https://en.wikipedia.org/wiki/File:Failed_section_of_peat_levee_(Wilnis,_August_2003).jpg)

2.1.4. Dike inspection

Once a dike is build, it should be regularly inspected to test whether it still fulfills its function. Maintainers of primary defense structures have to inspect them according to the Wettelijk BeoordelingsInstrumentarium (WBI) in the Netherlands (van Haegen, 2017). The maintainers have to report every twelve years to the minister. The specific requirements of this inspection are set up by the Dutch Ministry of Infrastructure and Environment. According to the WBI, it is tested whether the primary defense structures are strong enough to be able to withstand the (hydraulic) loads. The secondary defense structures are maintained by the provinces of the Netherlands. The laws and review of these secondary defense structures are made by the individual provinces (Rijkwaterstaat, 2009). Visual inspections are conducted periodically and are intensified during extreme conditions. In the Netherlands, the subjectivity of these inspections is reduced by the Digigids. Guidelines for different types of water defense structures can be found on their website. Among other things, it is inspected whether the condition of the grass cover is good, the revetment is still in place and whether there are holes in the dike because of animals. As described in the previous section, there are different mechanisms which can lead to failure of a dike. For each failure mechanism there are indicators which precede the failure of a dike. In Figure 2.7 these are shown in the form of a table for the main failure mechanisms as presented in Figure 2.5.

The failure indicators for a failure mechanism may or may not be observable with the human eye.



	Load	Weakness indicators	Failure indicators	Parameters
Wave overtopping	<ul style="list-style-type: none"> High water level Storm 	<ul style="list-style-type: none"> Insufficient height Cracks 	<ul style="list-style-type: none"> Erosion inner slope 	<ul style="list-style-type: none"> Height Cover
Sliding inner slope	<ul style="list-style-type: none"> Long-term high water level High phreatic line Damage cover 	<ul style="list-style-type: none"> Steep slope 	<ul style="list-style-type: none"> Cracks at crest Deformation of crest Uplift at toe 	<ul style="list-style-type: none"> Deformation Cover Geotechnical
Sliding outer slope	<ul style="list-style-type: none"> Fast decrease water level 	<ul style="list-style-type: none"> Steep slope 	<ul style="list-style-type: none"> Cracks at crest Tilt of crest 	<ul style="list-style-type: none"> Deformation Cover Geotechnical
Piping	<ul style="list-style-type: none"> High water level 		<ul style="list-style-type: none"> Wet spots inland Change vegetation Outflow water 	<ul style="list-style-type: none"> Soil moisture Temperature differences

Figure 2.7: Failure indicators for the four most common failure mechanisms of dikes in the Netherlands (Leijen, 2018).

Indicators such as erosion of the inner or outer slope can be detected by visual inspection (if the erosion is significant). Two of the failure mechanisms in Figure 2.7 can lead to deformation of the dike, which is less easy to observe with the human eye. However, deformation can be measured with several techniques and is described in the following section.

2.1.5. Measuring deformation

Because in this thesis the emphasis is placed on estimating deformation of dikes, in this sub-section different techniques are discussed to measure deformation. There are different ways in which deformation can be measured on dikes which are listed below.

- **Levelling:** This is probably one of the oldest methods to measure height and deformation. With a levelling rod, the height with respect to a datum is measured by using a spirit level. By obtaining height measurements on several epochs, deformation time series can be obtained with millimeter precision. Levelling is still used because often other techniques cannot obtain the same precision (Dentz et al., 2006). Levelling data can also be used to validate other techniques. For example, Clementini (2014) compared levelling data with deformation estimates obtained by a Radar Interferometry (see Section 2.2) analysis and found a large correlation between these two techniques.
- **Micro-ElectroMagnetic Systems (MEMS).** MEMS consists of a combination of electronic, mechanic and possibly chemical components and are capable of measuring deformation sub-centimeter accuracy (Danisch et al., 2008). The components are connected to a network cable which also supplies energy and takes care of the information transfer. The cable can be placed inside the dike by digging a slit in the longitudinal direction of the dike (which is restored with the same material, of course). The MEMS technique was applied by van den Berg et al. (2013) to realize a real time monitor system which lead to a Flood Early Warning System (FEWS) for dike stability alongside the Yellow river.
- **Terrestrial laser scanning:** A laser scanner measures distances to many points of an object. This results in a pointcloud of which each point has a x,y,z coordinate. By performing this measurement on different times, the geometry can be compared to see if the object (for example a dike) has been deformed (van Goor, 2011). An extreme example in which a laser scanner has been used to measure deformation of a dike is during the IJkdijk project. Here a dike was built and subjected to increasing forces by containers placed on the crest of the dike. The weight of the containers was increased until the dike failed. By using a 3D laser scanner, it was shown that weak points in the dike can be observed far ahead of a failure occurring (Weijers et al., 2009).
- **Global Positioning System:** The Global Positioning System (GPS) was invented in 1967 and originally had a military purpose for navigation. Since GPS became freely available in 1987, it has been used

for many other purposes than navigation. In geodesy, millimeter precision GPS has contributed to advances in geophysics, seismology, atmospheric science, hydrology and natural hazards (Bock and Melgar, 2016). Currently, 31 GPS satellites orbit the Earth and on any geographic location on any time there are at least 5 satellites visible (often up to 12 GPS satellites are visible). At least four satellites are needed to triangulate the 3D position of the receiver and to estimate the clock error. Continuous monitoring at a sample rate of (typically) 15-30 s makes it possible to determine displacements with respect to an initial epoch. Time series analysis of thousands of GPS stations over a 10-20 year period indicate standard deviations in the order of 0.1-0.3 mm/year for vertical motion (Bock and Melgar, 2016).

- Radar Interferometry: This radar technique measures phase differences between the emitted and received wave. By combining multiple images, it is possible to relate the interferometric phase to deformation. This technique will be further elaborated upon in the next section.

2.2. Radar interferometry

Radar interferometry is the technique which is used in this thesis to estimate deformation on dikes. Therefore, in this section an overview will be given of satellite radar systems. First, the geometry of a typical side-looking radar satellite will be discussed in Section 2.2.1, followed by an explanation of radar measurements (Section 2.2.2). In Section 2.2.3, the resolution of a Real Aperture Radar (RAR) and Synthetic Aperture Radar (SAR) will be discussed. Finally, in Section 2.2.4, the concept of interferometry is explained together with the different interferometric phase contributions.

2.2.1. Geometry

The general geometry of a radar imaging system is shown in Figure 2.8. An antenna is mounted on the satellite which is flying in azimuth direction with speed v . The radar beam is directed towards the surface in the range direction which has a look angle θ with respect to the nadir direction. This look angle is not constant but increases from near range (closest to the satellite) to far range (furthest away from the satellite), but often the look angle is referred to as the angle corresponding to the middle of the resolution cell. The azimuth and range coordinate system of the satellite can be projected on the ground, leading to ground range and azimuth coordinates. The swath width is dependent on the beam angle of the radar system, while the swath length is the length of the image in azimuth direction and depends on the time the radar is turned on.

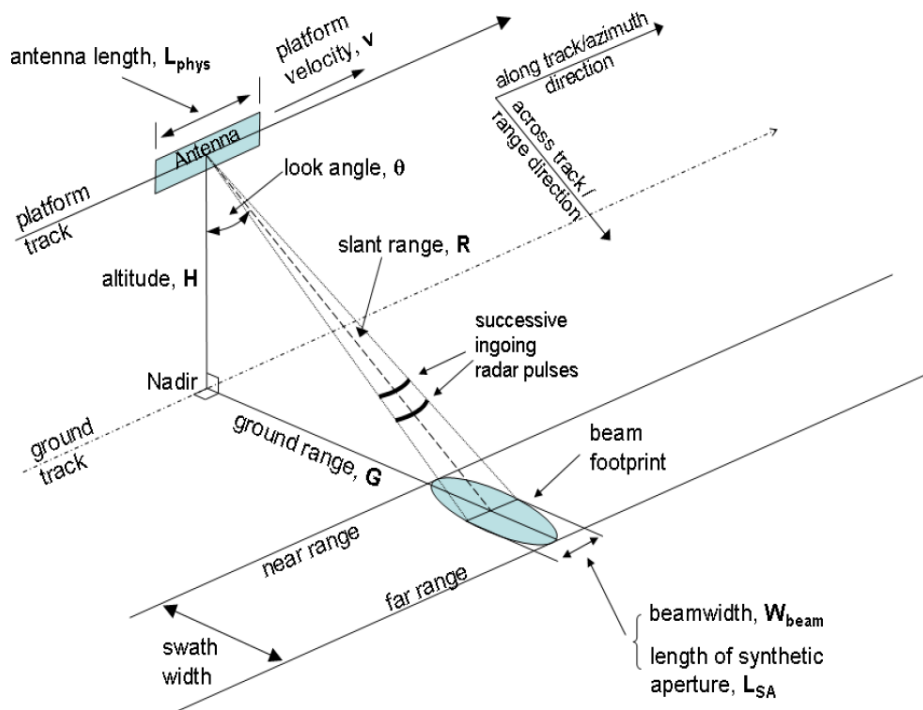


Figure 2.8: Geometry of side-looking imaging radars (Engdahl, 2013). Important parameters which will be used in this thesis are the look angle θ , azimuth and range direction, slant range R and platform velocity v .

An example of the transmitted signal from a satellite and the geometry of a dike is shown in Figure 2.9. The flight direction of the satellite is into the page. The dashed lines indicate the range bins (the spacing between those lines is equal to the range resolution) and the incidence angles of the different parts of the dike are shown in red. There are two remarks to be made which are important in analyzing and interpreting the data when a dike is measured with an InSAR system

- Pixel coverage: Depending on the slope of the dike, a pixel in slant range covers a certain area of the dike. For the blue slope in Figure 2.9, a relatively large length of the slope is imaged into a radar resolution cell (foreshortening). The whole slope, including a part of the crest and a part outside the dike boundaries, is imaged into one range bin. The green slope of the dike, however, is covered with more

than one resolution cell. In the next chapters, it is important to look at the flight direction of the satellite and on the slope which is measured with respect to the incoming signal.

- Deformation sensitivity: The sensitivity to the deformation of the dike is dependent on the incidence angle which is defined as the angle between the incoming signal with respect to the normal on the measured surface. The satellite is not sensitive to deformation which is perpendicular to the direction of signal propagation. For example, on the blue slope there is (almost) no sensitivity to deformation in the direction of the slope but large sensitivity to deformation perpendicular to the surface. For the green slope, the sensitivity to deformation in the direction of the slope is larger than the blue slope but the sensitivity to deformation perpendicular to the green slope is lower as compared to the blue slope.

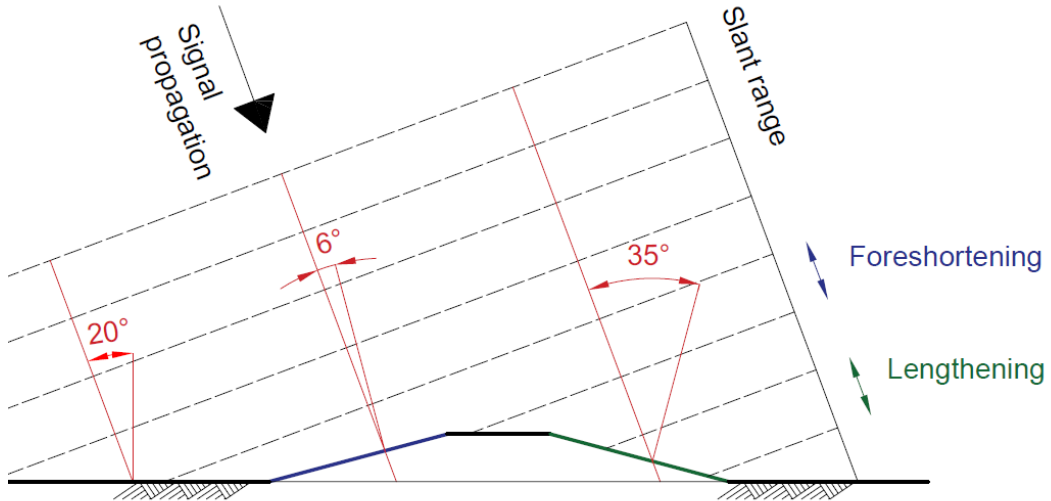


Figure 2.9: Visualization of the transmitted signal of a satellite (flight direction into the page) observing a dike with equal slopes to illustrate the difference in pixel coverage and deformation sensitivity of the slopes. The dashed lines indicate the wave fronds and are separated by the range resolution of the sensor. The blue slope is subjected by foreshortening, which means that a larger length of the dike is projected into a range bin. The green slope (which is of equal length as the blue slope) is covered in more than one range bin (which is indicated as lengthening) (Pinel et al., 2014). The sensitivity to deformation is dependent on the incidence angle (angle between the incoming signal and the normal of the measured surface, in red). There is no sensitivity to deformation in the direction perpendicular to the direction of signal propagation (alongside the blue slope). When observing an object such as a dike, it is important to keep in mind how the surface is mapped into the range direction of the SAR system. Source: Own work.

2.2.2. Measurements

A satellite radar image is obtained by transmitting a radar pulse at an angle to the earth from which the back scattered signals are measured. The European Space Agency provides different level of data products. The level-0 products contain the compressed unfocused data and is usually used by scientists who want to test SAR processing. The level-0 products are used to generate level-0 data, by applying various algorithms (pre-processing, Doppler Centroid Estimation, SAR focusing and post processing). The output of these processing steps are Single Look Complex (SLC) data and Ground Range Detected (GRD) data. SLC data are represented in the original radar geometry, are geo-referenced, corrected for azimuth-bistatic delay, antenna pattern and range spreading loss. GRD data is represented in ground range and azimuth coordinates by a projection that uses the WGS 84 ellipsoid. Also, a complex multilook operation is performed on the GRD data (for multilooking, see Section 3.2.1).

This information is stored in a Real Aperture Radar (RAR) image. A pixel in a radar image is composed of an amplitude A and a phase ψ

$$P = A \cdot \exp(i\psi), \quad (2.1)$$

in which P is called a complex phasor and i represents the imaginary number. The real and imaginary part of the complex phasor are related to the amplitude and the phase as

$$A = \sqrt{\text{Re}(P)^2 + \text{Im}(P)^2}, \quad (2.2a)$$

and

$$\psi = \arctan \left(\frac{\text{Im}(P)}{\text{Re}(P)} \right), \quad (2.2b)$$

Where $\text{Re}(P) = A \cos(\psi)$ and $\text{Im}(P) = A \sin(\psi)$ are the real and complex part of the complex phasor P , respectively. The phase ψ which is measured with the radar system, represents the phase difference between the outgoing wave and the returned wave. This phase in general consists of

$$\psi = W \{ \psi_{\text{range}} + \psi_{\text{atmo}} + \psi_{\text{scat}} + \psi_{\text{noise}} \}, \quad (2.3)$$

Where $W\{\}$ is the wrapping operator, which wraps the phase modulo 2π in the interval $[-\pi, \pi]$, because the total amount of phase cycles is unknown. ψ_{range} is the phase component dependent on the distance between the satellite platform and the resolution cell center, ψ_{atmo} is the phase caused by atmospheric delay, ψ_{scat} the scattering phase and ψ_{noise} the system noise which is dependent on the sensor characteristics. More information about these phase components is given in Section 2.2.4.

2.2.3. Resolution and pixel posting

According to M. Born et al. (1959), resolution is defined as the minimal distance at which two distinct scatterers can be uniquely defined as separate signals. Pixel posting is the spatial distance between two centers of a resolution cell. The difference between resolution and posting is shown in Figure 2.10.

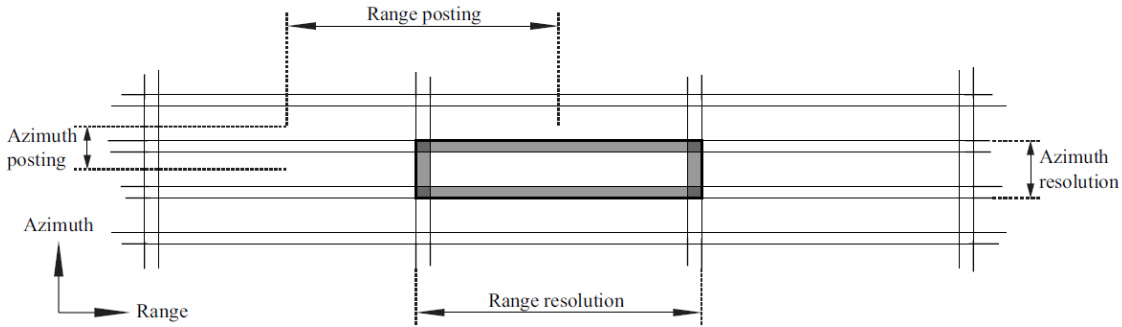


Figure 2.10: Illustration of resolution and pixel posting with overlapping areas in gray (Bermon, 2008). Overlapping of resolution cells leads to correlation between neighboring resolution cells. This introduced correlation is important to take into account in the developed methodology in this thesis.

The resolution in range direction is proportional to the pulse length τ and speed of light c

$$\Delta r = \frac{1}{2} c \tau. \quad (2.4)$$

For the ERS-1 satellite with a pulse length of $37 \mu s$, this corresponds to a range resolution of $\Delta r = 5500 m$. However, the range resolution can be significantly increased by decreasing the pulse length synthetically. This is done by transmitting a signal with increasing frequency, which is called a chirp. The pulse length is now inversely proportional to the bandwidth of the modulated signal. For the ERS-1 satellite the bandwidth is equal to 35.5 Mhz , leading to a pulse length of 64 ns and a range resolution of 9.7 m .

The range posting (distance in range between two resolution cell centers) is proportional to the sampling frequency F_s in the range direction.

$$d_r = \frac{c}{F_s}. \quad (2.5)$$

The azimuth resolution for a RAR is dependent on the wavelength λ and the physical length D of the antenna

$$\Delta a = \frac{\lambda R}{D}, \quad (2.6)$$

in which R is the distance of the satellite to the Earth. To obtain an azimuth resolution of 10 m , the physical length of the C-band antenna has to be ($\lambda = 5.8 \text{ cm}$, $R = 800 \text{ km}$) 4.6 km which is practically impossible.

However, the azimuth resolution can be improved by using a synthetically long antenna. Using the Doppler shifts of the surface while the satellite is passing, it is possible to improve the azimuth resolution to

$$\Delta a = \frac{D}{2}. \quad (2.7)$$

While this equation might suggest that the resolution can be improved indefinitely, the Signal to Noise Ratio (SNR) decreases with a shorter antenna length. The azimuth posting is dependent on the speed of the platform v and the Pulse Repetition Frequency (PRF)

$$d_a = \frac{v}{PRF}. \quad (2.8)$$

2.2.4. Interferometric SAR

The idea of Interferometric SAR (InSAR), is based on using the phase differences between two SLC images. Before calculating this phase difference, it is important to coregister the images because the images are not obtained at the same position. Using two SAR images it is possible to obtain phase differences between two acquisitions. An interferogram is obtained when two SAR images are coregistered and their complex values are multiplied (Hanssen, 2001)

$$I = P_1 \cdot P_2^* = A_1 A_2 \cdot \exp(i(\phi^1 - \phi^2)), \quad (2.9)$$

in which "*" is the complex conjugate operator, A_1 and A_2 are the amplitudes of the images and $\phi^1 - \phi^2$ is the interferometric phase. The interferometric phase consists of the following phase contributions:

$$\phi^{12} = W\{\phi^1 - \phi^2\} = W\{\phi_D + \phi_F + \phi_T + \phi_A + \phi_O + \phi_N\}, \quad (2.10)$$

Where ϕ_D is the change in phase as a result of a displacement between the two time intervals, ϕ_F (flat earth phase) is the change in phase due to a reference ellipsoid, ϕ_T is the effect of topography, ϕ_A represents the change in atmospheric state between the two acquisitions, ϕ_O is due to orbit errors and ϕ_N is a difference in phase because of the radar system noise and difference in scattering properties. $W\{\}$ is the wrapping operator. In the following subsections each of these phase contributions will be discussed.

Deformation phase

The deformation phase is the result of a displacement of the surface between two acquisitions. The deformation phase can be modeled as

$$\phi_D = \frac{-4\pi}{\lambda} D_{LOS}, \quad (2.11)$$

in which D_{LOS} is the displacement in the Line Of Sight (LOS) direction. If the incidence angle is larger than zero, the LOS displacement is a projection of the actual three dimensional deformation vector in Upward, North and East direction (Hanssen, 2001)

$$D_{LOS} = D_u \cos(\theta_{inc}) - \sin(\theta_{inc}) [D_n \cos(\alpha_h - 3\pi/2) + D_e \sin(\alpha_h - 3\pi/2)], \quad (2.12)$$

Where α_h is the satellite heading angle and D_u , D_n and D_e are the deformation components in Upward, North and East direction, respectively. However, there is no direct solution to the relation as presented in Eq. (2.12) because only one observation is available (van Leijen, 2014). Sometimes the the deformation in the longitudinal direction can be disregarded (for example for water defense structures such as dikes). To distinguish the vertical deformation from horizontal deformation, both ascending and descending orbits can be used. This leads to an extra observation which can be used to decompose the LOS deformation vector into horizontal and vertical deformation.

Flat earth phase

Even without any topographic variations between two points, there will still be phase differences present in the interferogram because of the range difference (see Figure 2.11). The flat earth phase for point P_0 on the reference surface is equal to (Samiei-Esfahany, 2017):

$$\phi_F = \frac{-4\pi}{\lambda} \left(d(\vec{P}_0, \vec{M}) - d(\vec{P}_0, \vec{S}) \right), \quad (2.13)$$

in which λ is the wavelength and $d(\dots)$ the distance operator. Using the far-field approximation in which it is assumed that the rays of the two satellites are parallel, Eq. (2.13) can be approximated as (Hanssen, 2001)

$$\begin{aligned}\phi_F &= \frac{-4\pi}{\lambda} \sin(\theta - \alpha), \\ \phi_F &= \frac{-4\pi}{\lambda} B_{\parallel},\end{aligned}\tag{2.14}$$

with θ the look angle, α the angle between the baseline and the horizontal surface and B_{\parallel} the parallel baseline component.

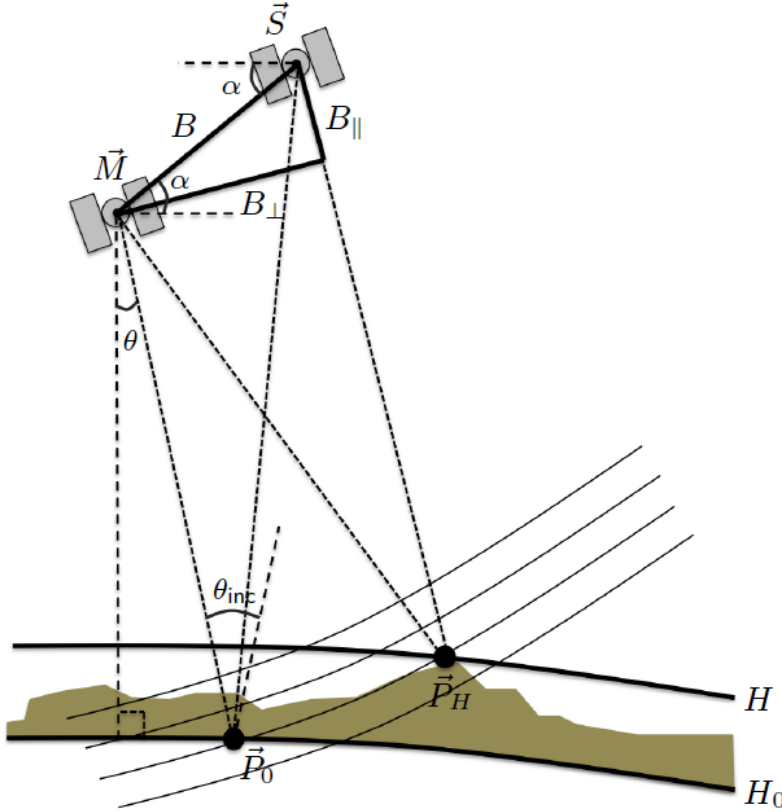


Figure 2.11: Master (\vec{M}) and slave (\vec{S}) satellite configuration to illustrate the flat earth and topographic phase components. The points \vec{P}_H (with topographic height H) and \vec{P}_0 (with topographic height H_0) are both on the same distance from the master antenna \vec{M} . The parallel baseline B_{\parallel} influences the flat-earth phase component and the topographic phase is linearly dependent on the perpendicular baseline B_{\perp} (Samiei-Esfahany (2017)).

Topographic phase

The topographic phase component (ϕ_T in Eq. (2.10)) is the effect of surface height on top of the reference ellipsoid. The topographic phase can be calculated as (following the geometry in Figure 2.11)

$$\phi_T = \frac{-4\pi}{\lambda} \left(\left(d(\vec{M}, \vec{P}_H) - d(\vec{S}, \vec{P}_H) \right) - \left(d(\vec{M}, \vec{P}_0) - d(\vec{S}, \vec{P}_0) \right) \right).\tag{2.15}$$

Since the distance from the master antenna to point \vec{P}_H and \vec{P}_0 are the same, the above equation can be simplified to

$$\phi_T = \frac{-4\pi}{\lambda} \left(d(\vec{S}, \vec{P}_0) - d(\vec{S}, \vec{P}_H) \right).\tag{2.16}$$

Using again the far-field approximation, Eq (2.16) can be approximated as (Hanssen, 2001)

$$\phi_T = \frac{-4\pi}{\lambda} \frac{B_{\perp}}{R \sin(\theta_{\text{inc}})} H, \quad (2.17)$$

in which R is the distance to the master antenna and H the topographic height. As can be seen in Eq. (2.17), the topographic phase increases with increasing perpendicular baselines between master and slave antenna. As an example to show the sensitivity to topography, the characteristics of the TerraSAR-X satellite are chosen. For a wavelength of $\lambda = 0.031$ m, $\phi_{\text{inc}} = 30^\circ$, $B_{\perp} = 100$ m and $R = 514$ km, the height ambiguity (the height difference between two points which leads to a 2π phase difference in an interferogram) is equal to 40m.

Atmospheric phase delay

Different states of the atmosphere on the times of image acquisition can lead to a differential atmospheric phase delay in the interferogram. There are different types of atmospheric delay which are summarized below (Liu, 2012)

- **Hydrostatic delay:** The hydrostatic delay is due to differences in pressure between two acquisitions which can be parameterized as a function of the surface pressure. It usually appears as a surface trend of a few millimeters in an interferogram (Hanssen, 2001).
- **Wet delay:** The wet delay is caused by atmospheric turbulence. Turbulent mixing has a large fluctuation in both time and space which makes it difficult to mitigate. Due to this high variability it is often modeled stochastically instead of deterministically.
- **Cloud droplets:** The interaction of the radar waves with the droplets in the clouds causes a delay of the signal. This delay is proportional on the liquid water content which is dependent on the cloud characteristics. If the liquid water content and the height of the cloud is known, the delay caused by the cloud droplets can be approximated which can be up to 3 cm for cumulonimbus clouds.
- **Vertical stratification:** The vertical stratification delay is a function of height which can be a large factor for areas with significant topography. If one point is situated higher compared to another point the electromagnetic waves have to travel farther through the atmosphere which introduces a longer path delay. One way to model this effect is to use radiosonde profiles to compute the refractivity of each layer and integrate their differences with height.

Liu (2012) uses a Numerical Weather Prediction (NWP) model to predict atmospheric delays in C-band SAR acquisitions. It was found that considerable reductions of the delay RMS error could be found for test cases with strong topography (i.e., Hawaii and Mexico City). However, in areas with no strong vertical stratification the Weather Research and Forecast (WRF) model cannot mitigate the delay and even can lead to a deterioration of the original images. This is because the WRF model is not able to resolve water vapor at the fine scales (< 50 km).

2.2.5. Influence of phase contributors

The accuracy of the parameter of interest, the deformation, depends on how good the other phase contributors can be estimated. The flat earth phase can be computed based on a reference ellipsoid and the topographic phase is usually subtracted using a Digital Elevation Model (DEM). Orbital errors are usually removed by subtracting a linear trend from the interferogram (Bähr and Hanssen, 2012). The error due to different scatter properties as well as different atmospheric phase are harder to estimate and interfere with the deformation signal (Samiei-Esfahany, 2017). Temporal and baseline decorrelation results in scattering noise in the interferogram, especially in vegetated areas where the properties of the scatterers change rapidly with respect to the time between two acquisitions (Hooper et al., 2007). Different atmospheric states can lead up to 10cm error (Zebker et al., 1996). For a single interferogram it is difficult to estimate the atmospheric phase contribution. In the next chapter, several Time Series Interferometry methods will be discussed which use a stack of interferograms to estimate atmospheric and orbital phase contributions.

3

Time Series interferometry

One of the main error sources in an interferogram is the differential atmospheric phase which is present in the interferogram because of the different states of the atmosphere between the two acquisitions. However, when a stack of interferograms is used, the atmospheric contribution can be separated from the interferogram because the different atmospheric states are uncorrelated in time.

Before going into the different time series methodologies, first it is important to distinguish between the different type of scatterers which these methods exploit. On one side of the spectrum there is the Point Scatterer (PS), while on the other side of the spectrum there is the Distributed Scatterer (DS) (see Figure 3.1). In Figure 3.1 (b) one object dominates the reflection of the resolution cell, called a PS, while the other objects just introduce noise and is known as clutter. If the reflection of this point scatterer is strong enough, it will be coherent even for large baselines. For DS (see Figure 3.1 (a)), however, the magnitude of the reflection for each object is about the same. DS are strongly affected by decorrelation, but may contain coherent information for shorter temporal baselines.

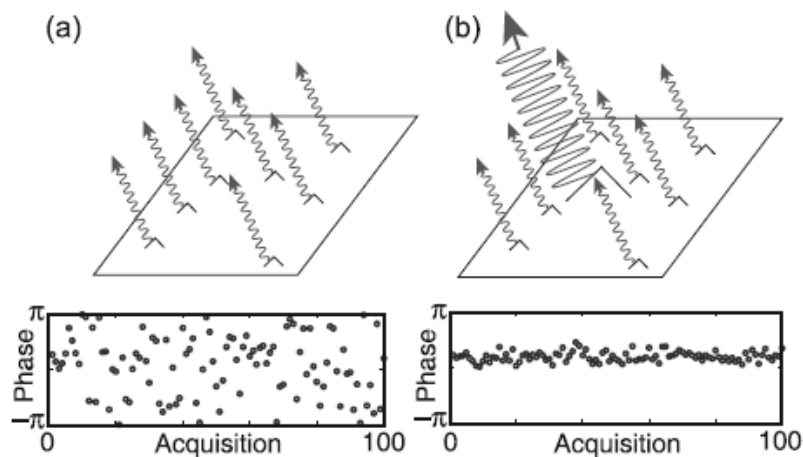


Figure 3.1: Distributed scattering (a) versus persistent scattering (b). In the top row it can be seen that for distributed scattering the magnitudes of the reflections are about equal and for persistent scattering there is one strong reflector which dominates the measurement. In the bottom row 100 phase simulations. The bottom row shows for the Distributed Scatterer a random distribution between $-\pi$ and π , while for the Point Scatterer the phases are distributed with a smaller dispersion (Hooper et al., 2007)

In Section 3.1 several time series interferometry methods are explained which make use of point scatterers. Time series interferometry methods which make use of Distributed Scatterers are explained in Section 3.2.

3.1. Persistent Scatterer Interferometry

The Persistent Scatterer Interferometry (PSI) methodology was first developed by Ferretti et al. (2001).

The principle is to process a single master stack of interferograms to estimate deformation time series. Interferograms with a large temporal baseline are affected by decorrelation and therefore only points that show scattering characteristics which are more or less constant in time can be used to estimate deformation time series.

The first step in the PSI processing chain is to select a set of Persistent Scatterer Candidates (PSC). One approach to find these PSC uses the normalized dispersion of the amplitude D_A as an approximation for the phase dispersion σ_ϕ (Ferretti et al., 2001)

$$\sigma_\phi \simeq \frac{\sigma_A}{\mu_A} = D_A, \quad (3.1)$$

where μ_A and σ_A are the mean and standard deviation of the amplitude. Pixels are classified as PSC when the dispersion index is below a certain threshold, typically $D_A < 0.25$ (Ferretti et al., 2001). After the PSC are selected, a first order network is constructed (e.g using a Delaunay triangulation, van Leijen (2014)). The choice of the master image can be made based on different parameters such as maximization of the stack coherence, minimization of atmospheric error or minimization of expected clutter (van Leijen, 2014). A first estimate of the deformation is made by for example the ambiguity function, which searches a solution space to find the parameters x that maximizes the temporal coherence $|\gamma|$

$$\operatorname{argmax}_x |\gamma| = \left| \frac{1}{M} \sum_{i=1}^M \exp \left(j \left(\phi_{\text{obs}}^{0i} - \phi_{\text{model}}(x)^{0i} \right) \right) \right|, \quad (3.2)$$

in which M is the number of interferograms and ϕ_{obs}^{0i} and ϕ_{model}^{0i} the observed and modeled phase with respect to the master image, respectively. The modeled deformation is a function of the unknown parameter(s) x which is estimated with the use of the periodogram by searching through a defined set of possible solutions. The solution with the highest temporal coherence $|\gamma|$ is then chosen as the optimal solution. In Eq.(3.3) a model is shown which assumes a linear deformation rate and a residual topography, but any other desired deformation model can be used.

$$\phi_{\text{model}}(x) = \phi_D + \phi_T = \frac{4\pi}{\lambda} B_T V_{\text{lin}} - \frac{4\pi}{\lambda} \frac{B_\perp}{R \sin(\theta_{\text{inc}})} \Delta H_{\text{res}}, \quad (3.3)$$

with ΔH_{res} the residual topographic height. The next step is then to remove the orbit errors by subtracting an estimated trend from each interferogram. After removing the orbital errors, and evaluating the ambiguity function in Eq.(3.2), possibly more PS can be detected. To separate the deformation from the remaining atmospheric delay and the noise, the different temporal and spatial behavior of these parameters is exploited. The atmospheric phase can be regarded correlated in space but uncorrelated in time if the acquisitions are at least a few hours apart (Hanssen, 2001). The noise is assumed to be uncorrelated in space and time and the deformation is assumed to be correlated in time. By applying a low-pass filter, the deformation signal can be separated from the noise and the atmospheric phase. The noise is then separated from the atmospheric phase by applying a spatial low-pass filter. The Atmospheric Phase Screen (APS) can now be subtracted from the measured phase to further decrease the noise. Just as after the orbital phase removal, possibly more PS can be selected after evaluating the ambiguity function in Eq.(3.2).

The PSI technique is able to provide precise estimates of deformation of many objects such as railway bridges (Huang et al., 2017), buildings (Ciampalini et al., 2014) and landslides (Tofani et al., 2013). Another example is from Barends et al. (2005, Chapter 4.5) who were able to estimate linear deformation rates of the Hondsbosche zeekering, a sea dike in the Netherlands. The revetment at the sea side of the dike provides a good surface for stable reflections, which leads to many PS points on the seaside of the dike.

StaMPS

The PSI method works usually quite well in areas with structures which provide stable reflections over time. However, if these stable reflections are not present in a certain scene, this method might not work that well. For example, Hooper et al. (2004) failed to obtain reliable deformation rates for non-urban volcanic areas because not enough PS pixels were found to form a good network, using the method of Ferretti et al. (2001). Another problem is that a deformation model is needed to separate the the deformation signal from error sources such as the atmosphere and topography. Hooper et al. (2007) therefore developed a model called StaMPS (Stanford Method for PS), which uses spatial correlation of the interferometric phases to select those

pixels with low phase variance in terrains with or without buildings. In this method, there are four aspects (Hooper et al., 2007) in which StaMPS differs from the PSI technique as is known by Ferretti et al. (2001):

1. Interferogram formation: The master image is chosen such that the correlation is maximized for all interferograms. The total correlation is modeled as the product dependent on time interval (T), perpendicular baseline (B_{\perp}), difference in Doppler centroid (F_{DC}) and thermal noise

$$\begin{aligned} \rho_{\text{total}} &= \rho_{\text{temporal}} \rho_{\text{spatial}} \rho_{\text{doppler}} \rho_{\text{thermal}}, \\ &\approx \left[1 - f\left(\frac{T}{T^c}\right) \right] \left[1 - f\left(\frac{B_{\perp}}{B_{\perp}^c}\right) \right] \left[1 - f\left(\frac{F_{DC}}{F_{DC}^c}\right) \right] \rho_{\text{thermal}} \end{aligned} \quad (3.4)$$

with

$$f(x) = \begin{cases} x, & \text{for } x \leq 1 \\ 1, & \text{for } x > 1 \end{cases},$$

where c stands for some critical value for the parameters. The master image is chosen such that the total correlation $\sum_{i=1}^N \rho_{\text{total}}$ is maximized.

2. Phase stability estimation: The amplitude dispersion as depicted in Eq.(3.1) is used different in the sense that a higher threshold (about 0.4) is set to the dispersion such that almost all PS points are selected. The next step is to apply a band-pass filtering step in the frequency domain. The resulting filtered phase $\hat{\phi}_{12}$ contains the spatially correlated parts of ϕ_{12} . Subtracting this estimated filtered phase from Eq.(2.10) will result in the spatially uncorrelated part of ϕ_{12} . Based on the variation of the residual phase of each pixel γ_x it is then decided whether a pixel can be considered as PS.
3. PS selection: A two-dimensional probability density distribution is obtained by binning the amplitude dispersion D_A and the phase stability parameter γ_x . Some threshold for the phase stability parameter is defined based on a linear relationship with the amplitude dispersion:

$$\gamma^{thresh} = \kappa \hat{D}_A \quad (3.5)$$

In which the constant κ is determined by Least-Squares inversion. Pixels are then selected as PS pixels for which $\gamma_x < \gamma^{thresh}$.

4. Displacement estimation: For unwrapping the wrapped interferograms, a three dimensional unwrapping algorithm is applied. To obtain $\Delta\phi_D$, still some noise terms have to be removed after the unwrapping step. To estimate the contribution of the noise caused by the master image (which is correlated in time), a low-pass filter operation is performed in time. Assumed is that the integer ambiguity is the same for most pixels in an interferogram. Therefore, phase differences are used before the low-pass filter to cancel this term. For the noise estimation caused by the slave images, a high-pass filter is used since it is assumed that the slave contributions are temporally uncorrelated.

Using this new approach, Hooper et al. (2007) were able to estimate deformation on the Volcán Alcedo for which the method of Ferretti et al. (2001) failed to obtain reliable deformation (Hooper et al., 2004). In the next sub-section first some theoretical background on adaptive multilooking and coherence is presented, after which some Distributed Scatterer Interferometry time-series methodologies are discussed.

3.2. Distributed Scattering Interferometry

As described in the beginning of this chapter, Distributed Scatterers (DS) are usually only coherent for short baselines. The amount of decorrelation of DS can, however, be reduced by applying adaptive multilooking (Section 3.2.1). A metric for the amount of correlation between interferograms is called the coherence, which is explained in Section (3.2.3). Section 3.2.4, 3.2.5 and 3.2.6 then illustrates some Distributed Scatterer Interferometry (DSI) methods.

3.2.1. Adaptive multilooking

The selection of Statistical Homogenous Pixels (SHP) is based on the amplitude behavior in time as a proxy for phase homogeneity. Usually a square (or rectangular) window is selected around a pixel (reference pixel) in which all other pixels (test pixels) are compared to the reference pixel based on a statistical test. There are several methods to test for these SHP, of which three will be shortly explained in this chapter (the Mean, Kolmogorov-Smirnov and Anderson-Darling test).

Mean test

In the mean test it is assumed that the amplitude of a SAR image is Rayleigh distributed (assuming a distributed scattering system with circular Gaussian distribution). The estimated mean amplitude \bar{A} from the data then has, according to the central limit theorem, a Gaussian distribution. Following Samiei-Esfahany (2017):

$$\bar{A} = \frac{1}{N} \sum_{i=1}^N A_i, \quad (3.6)$$

where N is the amount of SAR acquisitions, and A_i the amplitude of the considered pixel for image i . The estimated mean amplitude for the reference pixel is then compared with other pixels in the selected window (tested pixels). The null hypothesis H_0 and alternative hypothesis H_a are defined as

$$H_0 : E\{A_t\} = A_r \quad H_a : E\{A_t\} \neq A_r \quad (3.7)$$

in which the subscripts t and r indicate the pixel which is tested and the reference pixel, respectively. The test statistic for the mean test, which has a standard normal distribution, can then be formulated as

$$|T_{\text{mean}}| > k_{\alpha/2}, \quad (3.8)$$

where

$$T_{\text{mean}} = \frac{\bar{A}_t - \bar{A}_r}{\frac{1}{\sqrt{N}} \sigma_{A_r}}, \quad (3.9)$$

the null hypothesis being rejected if the absolute value of the test statistic T_{mean} is larger than $k_{\alpha/2}$ (the $\alpha/2$ percentile of the standard normal distribution).

Kolmogorov-Smirnov test

The Kolmogorov-Smirnov (KS) test was introduced by Kolmogorov (1933) and Smirnov (1936) and was originally used to compare an Empirical Cumulative Distribution Function (ECDF) with a reference distribution function. For selecting SHP pixels, the same test can be used to test whether the ECDF of a reference pixel is the same as the ECDF of a neighbor pixel. The test statistic is defined as

$$T_{r,t} = \sup_x |F_r(x) - F_t(x)|, \quad (3.10)$$

Where T is the test statistic, \sup is the supremum operator, $F_r(X)$ is the reference ECDF and $F_t(x)$ is the ECDF to be tested. An example of the KS test for two pixels is visualized in Figure 3.2. The ECDF is calculated for the reference pixel (in red) and for a pixel which is to be tested (in blue). The supremum of the difference between these two ECDF's is defined as the maximum distance between the two curves.

The null hypothesis that the two samples arise from the same distribution function is rejected at significance level α is

$$T_{r,t} > c(\alpha) \sqrt{\frac{n+m}{nm}}, \quad (3.11)$$

where

$$c(\alpha) = \sqrt{-\frac{1}{2} \ln\left(\frac{\alpha}{2}\right)}, \quad (3.12)$$

and n and m are the sizes of the reference sample and tested sample, respectively. In the case this test is applied on a stack of radar images, the sizes of the reference sample n and tested sample m are the same and are equal to the amount of SLC images that are taken into account.

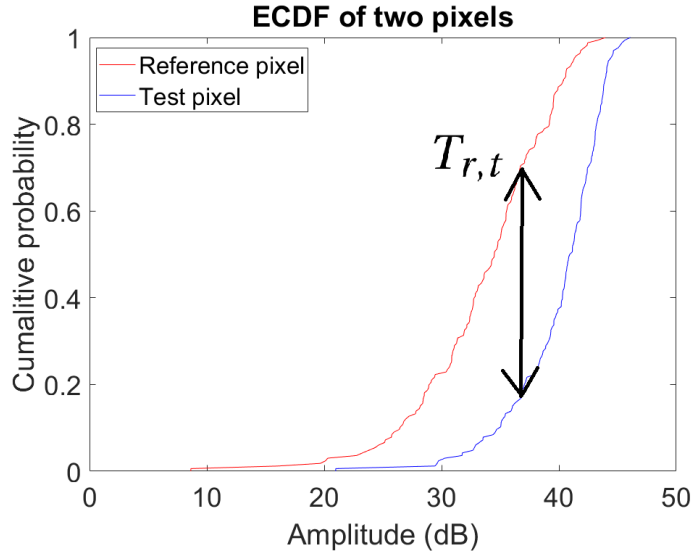


Figure 3.2: Illustration of the Kolmogorov-Smirnov test. The ECDF of two pixels on the Marken dike are plotted. $T_{r,t}$ is the test statistic and is equal to the maximal distance between the ECDF of the reference pixel (in red) and the ECDF of the tested pixel (in blue)

Anderson-Darling test

Anderson and Darling (1952) developed a new statistical method to test whether a sample of data is drawn from a given probability function. This test can easily be modified to a two-sample test, as shown by Pettitt (1976):

$$A_{nm}^2 = n \int_{-\infty}^{\infty} \frac{[F_n(x) - G_m(x)]^2}{H_N(x)[1 - H_N(x)]} dH_N(x), \quad (3.13)$$

Where F_n and G_m are the two distribution functions (with n and m samples, respectively) used to test the null hypothesis that the two samples arise from the same distribution function. H_N ($N = n+m$) is the combined distribution function which is related to the two samples as

$$H_N(x) = [nF_n(x) + mG_m(x)] / N. \quad (3.14)$$

Compared to the Kolmogorov-Smirnov test, the Anderson-Darling test places more emphasis on the tails of the distribution. For radar applications this property is important because the tails of the distribution (which influence the higher order moments) play an important role (Parizzi and Brcic, 2011). In their paper, Parizzi and Brcic (2011) compared different statistical tests (Kullback-Leibler Divergence, Kolmogorov-Smirnov, Anderson-Darling and the Generalized Likelihood Ratio Test GLRT) in which they found that the Anderson-Darling test proved to be the most powerful.

3.2.2. Computational performance

While the Anderson-Darling test was found to be the most powerful test, it is also computationally expensive for large stacks. Samiei-Esfahany (2017) made a comprehensive overview of the properties of the tests mentioned in the previous paragraphs. The AD test has a better performance compared to the KS test and is best suited for medium size stacks ($10 < N < 100$), while the mean test is recommended for large stacks ($N > 100$). Here a trade-off is made between computational time and quality of the test. The AD test still performs better for $N > 100$ but becomes too expensive in terms of computation time. The mean test is then a good choice, since it becomes more powerful for large stacks and is relatively fast in terms of computation time.

In the next section, the SHP which were found by one of the statistical tests will be used to estimate the complex coherence.

3.2.3. Complex coherence

A metric for the amount of correlation between two SAR measurements is called the complex coherence. The complex coherence between images P_i and P_j is defined as (Just and Bamler, 1994)

$$\gamma_{ij} = \frac{E[P_i P_j^*]}{\sqrt{E[|P_i|^2]E[|P_j|^2]}} = |\gamma_{ij}| \exp(j\phi_{0_{i,j}}), \quad (3.15)$$

in which $|\gamma_{ij}|$ is the absolute coherence which defines the amount of correlation between the two measurements P_i and P_j and $\phi_{0_{i,j}}$ is the phase of the complex number γ_{ij} and represents the expectation of the interferometric phase between P_i and P_j . In practical situations, the expectation values in Eq.(3.15) cannot be obtained by averaging over multiple measurements because there is only one measurement per acquisition (i.e only one value for P_i and P_j). Instead of averaging over samples in time, it is also possible to apply spatial averaging if one assumes ergodicity (statistical properties of neighboring pixels are the same). To do so, only pixels within the multilooking window that are defined as SHP are used for estimating the complex coherence. In this way the assumption of ergodicity is justified because only pixels for which the ECDF (or mean) of the amplitude is similar to the reference pixel are taken into account. Eq.(3.15) can then be approximated as

$$\hat{\gamma}_{ij} \approx \frac{\sum_{k \in \Omega} P_{ik} P_{jk}^*}{\sqrt{\left(\sum_{k \in \Omega} |P_{ik}|^2 \right) \left(\sum_{k \in \Omega} |P_{jk}|^2 \right)}}, \quad (3.16)$$

where Ω defines all the pixels in the window of the reference pixel which are defined as SHP using a statistical test. If the assumption of ergodicity holds, $\hat{\gamma}_{ij}$ is the maximum likelihood-estimator of γ_{ij} (Touzi et al., 1996). However, in the same paper it is also shown that the absolute value of the coherence is biased, especially for lower coherence values and lower number of looks. Especially for lower coherence areas, the number of looks should be high enough to minimize the bias of the coherence estimation.

If the absolute value of the complex coherence (Eq. (3.16)) is estimated for each interferometric combination in a data stack, one obtains the coherence matrix

$$\Gamma = \begin{bmatrix} 1 & \gamma_{12} & \dots & \gamma_{1N} \\ \gamma_{21} & 1 & \dots & \gamma_{2N} \\ \vdots & \vdots & \ddots & \vdots \\ \gamma_{N1} & \gamma_{N2} & \dots & 1 \end{bmatrix}, \quad (3.17)$$

This matrix displays for each possible interferogram the absolute coherence, indicating the quality of each interferometric combination. In Figure 3.3 two examples of coherence matrices are shown.

Figure 3.3a shows the coherence matrix for a pixel on the revetment part of the dike. Reflections on this part of the dike are usually stable in time, leading to high coherence for most of the interferometric combinations (even for large temporal baselines). In Figure 3.3b a coherence matrix is depicted for a pixel on the vegetated part of the dike. Because of the constantly changing surface, the coherence is in general quite low, only a few interferometric combinations being highly coherent.

The coherence matrix can be used as a weight matrix, such that highly coherent interferograms get more weight as compared to interferograms with lower coherence to (for example) estimate deformation velocities. Furthermore, the coherence matrix could be used to completely exclude low coherent interferograms based on a threshold (see Section 5.1).

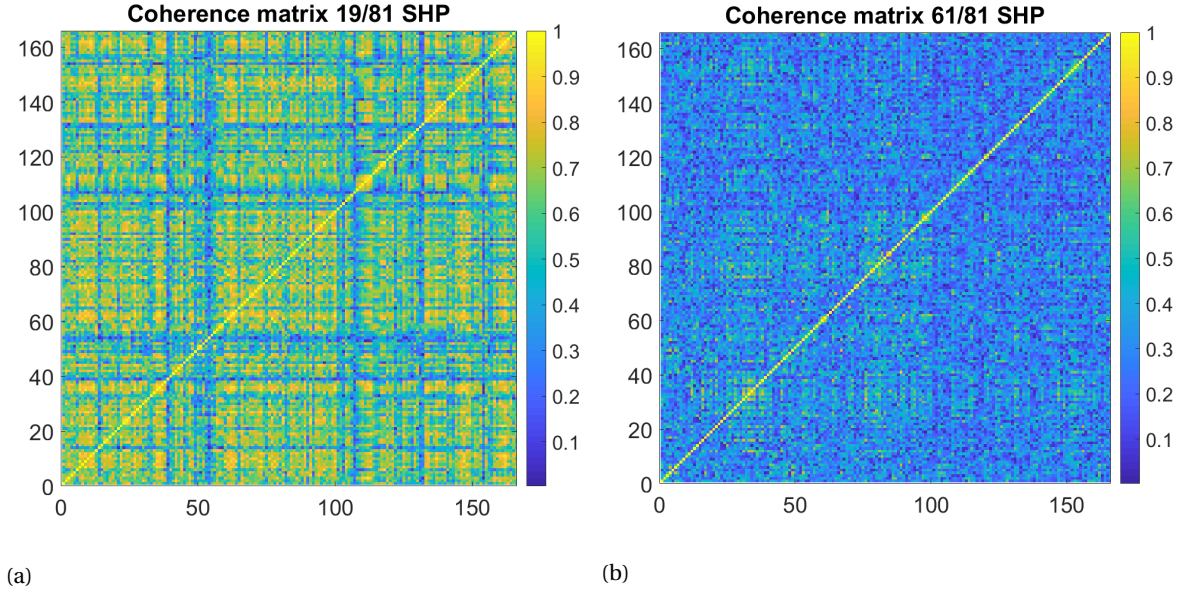


Figure 3.3: Two examples of coherence matrices. **(a)** Coherence matrix of a pixel of the Marken dike with revetment. **(b)** Coherence matrix of a vegetated pixel of the Marken dike. TerraSAR-X data is used from the fifth of February, 2009, until the first of February, 2016. It can be observed that the coherence for a pixel on the vegetated part of the dike is (in general) much lower as compared to a pixel on the revetment part of the dike. While the coherence values of the vegetated pixel are in general low, there are coherent interferograms which contain information.

Modelling the absolute coherence

The coherence matrix can be estimated from the data by using Eq. (3.16), or can be modelled theoretically. The total coherence γ_{tot} (decorrelation) can be calculated using the following formula (Zebker and Villasenor, 1992).

$$\gamma_{tot} = \gamma_{spatial} \cdot \gamma_{thermal} \cdot \gamma_{temporal}, \quad (3.18)$$

where $\gamma_{spatial}$ represents the spatial decorrelation which is dependent on the perpendicular baseline and viewing geometry, $\gamma_{thermal}$ represents the thermal decorrelation due to system noise related to the SNR and $\gamma_{temporal}$ is related to physical changes of the surface between two acquisitions.

- Thermal decorrelation: The thermal decorrelation can be calculated as

$$\gamma_{thermal} = \frac{1}{1 + SNR^{-1}}, \quad (3.19)$$

Where SNR is the Signal to Noise Ratio, which is dependent on system parameters of the satellite.

- Spatial decorrelation: Spatial decorrelation is dependent on the perpendicular baseline between two passes at acquisition time. The spatial correlation between two images can be calculated as (Wei and Sandwell, 2010)

$$\gamma_{spatial} = 1 - \frac{2|B_{\perp}|R_y \cos^2(\theta - \alpha)}{\lambda R}, \quad (3.20)$$

in which B_{\perp} is the perpendicular baseline, R_y is the resolution in range direction, θ is the incidence angle, α the local surface slope in range direction, λ the wavelength of the sensor and R the distance between the satellite and the Earth.

- Temporal decorrelation: This term is caused by the change in scattering mechanisms of a scattering cell between two acquisitions. For example; vegetation growth, change in soil moisture, grazing animals and wind caused movement of vegetation can cause this type of decorrelation. Morishita and Hanssen (2015b) modelled the temporal decorrelation term on pasture on drained peat soils as

$$\gamma_{temp} = \exp\left(-\frac{1}{2}\left(\frac{4\pi}{\lambda}\right)^2 \sigma_r^2\right), \quad (3.21)$$

with λ the wavelength and σ_r^2 the variance of the motion of scatterers in the line of sight. In their paper, the decorrelation is divided into a short term component (due to e.g. wind) and a long term component (due to vegetation growth) which is dependent on time. This leads to the following equation

$$\gamma_{temp}(t) = \gamma_{t,short} \cdot e^{-t/q}, \quad (3.22a)$$

with

$$\gamma_{t,short} = \exp\left(-\frac{1}{2}\left(\frac{4\pi}{\lambda}\right)^2 \sigma_{r,short}^2\right), \quad (3.22b)$$

and

$$q = \frac{2}{\sigma_{r,long}^2} \left(\frac{\lambda}{4\pi}\right)^2. \quad (3.22c)$$

q is the decorrelation rate, which becomes quadratically larger with the wavelength. In Figure 3.4a, the temporal decorrelation term is calculated according to Eq. (3.21) for different wavelengths as a function of the standard deviation of the LOS motion of the scatterer.

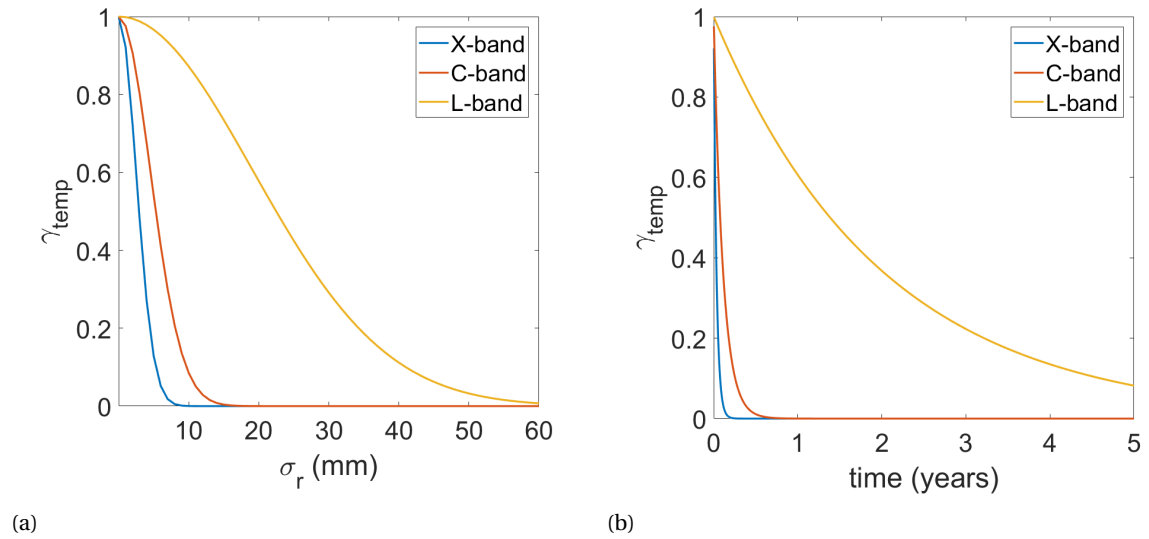


Figure 3.4: **(a)** Standard deviation of the motion of a scatterer in the Line Of Sight vs temporal decorrelation. **(b)** Temporal decorrelation vs time calculated according to Eq.(3.22a). The different curves indicate X,C and L band wavelengths.

It can be noted that shorter wavelengths decorrelate much quicker as compared to larger wavelengths. X-band is completely decorrelated at around $\sigma_r = 7$ mm, C-band at $\sigma_r = 14$ mm while L-band decorrelates at $\sigma_r = 55$ mm. To get an impression of the decorrelation as function of time, Samiei-Esfahany (2017) modeled σ_r^2 as

$$\sigma_r^2(t) = \int_{t_1}^{t_2} \sigma_0^2 dt = \sigma_0^2(t_2 - t_1) = \sigma_0^2 t, \quad (3.23)$$

where σ_0^2 is the variance of the motion of the scatterer per unit of time and t is the time between acquisitions. Because the long-term decorrelation term becomes dominant in InSAR satellites, we focus on this term. Inserting Eq. (3.23) in Eq. (3.21) leads to

$$\gamma_{temp}(t) = \exp\left(-\frac{1}{2}\left(\frac{4\pi}{\lambda}\right)^2 \sigma_0^2 t\right) \quad (3.24)$$

In Figure 3.4b the temporal decorrelation is plotted as function of time for X,C and L-band. The coherence (only temporal decorrelation taken into account) is reduced to 0.4 after 11 days for X-band, 37 days for C-band and 668 days for L-band. For σ_0 a value of $1 \text{ mm}^2/\text{day}$ is used (Samiei-Esfahany, 2017).

Morishita and Hanssen (2015b) found that the temporal decorrelation in winter months (October-March) is lower as compared to the summer months (April-September), based on a pasture area South of

Delft. Furthermore they concluded that although longer wavelengths are better for a longer decorrelation time, it is the combination of longer wavelengths, shorter revisit times and higher spatial resolution which leads to minimal decorrelation.

Estimating standard deviation of interferometric phase

The estimated coherence based on (3.16), is a metric for the quality of two interferograms for a considered pixel. This quality indicator, however, is dimensionless and cannot be interpreted (directly) in terms of radians. However, the coherence is related to the standard deviation of the phase, which is expressed in radians. This relation will be derived using the probability density functions of two pixels with zero-mean circular Gaussian distribution. The joint probability density function (pdf) of two SLC pixels is defined as (Tough et al., 1995)

$$f_{\underline{A},\phi}(A, \phi) = \frac{2L(LA)^L}{\pi\zeta^{L+1}(1-|\gamma|^2)\Gamma(L)} \exp\left(\frac{2|\gamma|LA\cos(\phi-\phi_0)}{\zeta(1-|\gamma|^2)}\right) K_{L-1}\left(\frac{2LA}{\zeta(1-|\gamma|^2)}\right), \quad (3.25)$$

where L is the number of SHP, $\zeta = \sqrt{E\{|P_1|^2\} + E\{|P_2|^2\}}$, K_{L-1} represents the modified Bessel function of the third kind (Idris et al., 2016) and $\Gamma()$ is the Gamma function defined as $\Gamma(L) = (L-1)!$ in which L is a positive integer. The pdf of the interferometric phase ϕ can now be obtained by integrating over the amplitudes A (Tough et al., 1995)

$$f_{\phi}(\phi) = \frac{(1-|\gamma|^2)^L}{2\pi} \left[\frac{\Gamma(2L-1)}{(\Gamma(L))^2 2^{2(L-1)}} \cdot \left(\frac{(2L-1)\beta}{(1-\beta^2)^{L+0.5}} \right) \left(\frac{2}{\pi} + \arcsin(\beta) + \frac{1}{(1-\beta^2)^L} \right) \right] \\ + \frac{(1-|\gamma|^2)^L}{4\pi(L-1)} \sum_{i=0}^{L-2} \frac{\Gamma(L-0.5)}{\Gamma(L-0.5-i)} \frac{\Gamma(L-1-i)}{\Gamma(L-1)} \frac{1+(2i+1)\beta^2}{(1-\beta^2)^{i+1}}, \quad (3.26)$$

with $\beta = |\gamma|\cos(\phi-\phi_0)$ and ϕ_0 the expected interferometric phase. The distribution of the interferometric phase is fully dependent on the (absolute) coherence $|\gamma|$ and on the number of SHP L . Note that for large numbers of L , evaluating $\gamma(2L-1)$ can be cumbersome by using double precision. In Matlab, a workaround can be created with the use of the Symbolic toolbox which uses symbolic numbers (Matlab, 2018). In Figure 3.5, some examples are shown for the pdf, using different values for the coherence and the number of SHP.

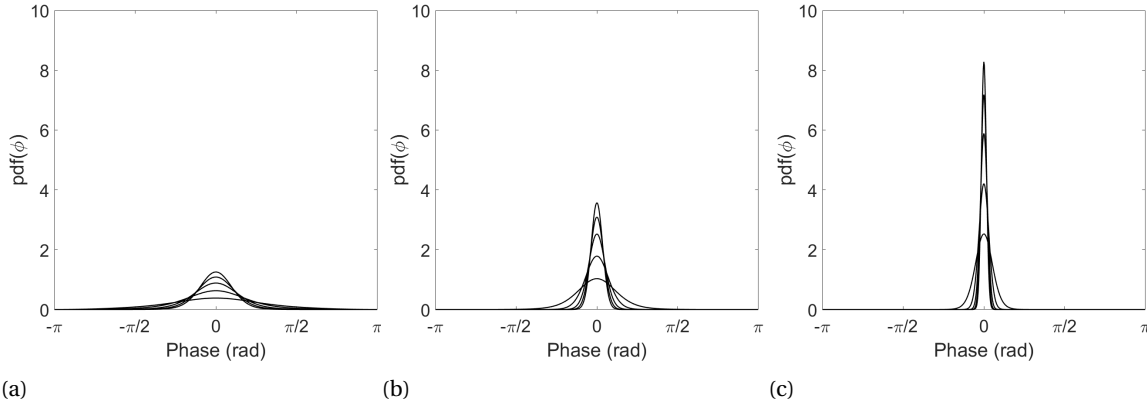


Figure 3.5: Visualization of probability density function of the interferometric phase (based on Eq. (3.26)) for different values of the absolute coherence γ and number of looks L . (a) $|\gamma| = 0.2$, (b) $|\gamma| = 0.5$ and (c) $|\gamma| = 0.8$. The number of looks (amount of SHP) are 10,30,60,90,120 (the higher the peak of the PDF, the more looks are used). After Hanssen (2001).

For lower coherence values, the PDF is more flat as compared to higher coherence values. Increasing the number of looks (amount of SHP) leads to a higher peak of the PDF. For the extreme case of $|\gamma| = 0$, Eq. (3.26) reduces to $\frac{1}{2\pi}$ which is equivalent to a uniform distribution between $-\pi$ and π . For another extreme case, $|\gamma| = 1$, the density increases to infinity at $\phi = \phi_0$ and is zero otherwise (dirac-delta function with peak at ϕ_0). Under the assumption of ergodicity ($\phi_0 = 0$), the variance of the interferometric phase can be calculated as (Just and Bamler, 1994)

$$\begin{aligned}\sigma_{\underline{\phi}}^2 &= E\{(\phi - E\{\phi\})^2\} = \int_{\phi_0 - \pi}^{\phi_0 + \pi} (\phi - \phi_0)^2 f_{\underline{\phi}}(\phi) d\phi \\ &= \int_{-\pi}^{\pi} (\phi)^2 f_{\underline{\phi}}(\phi) d\phi.\end{aligned}\quad (3.27)$$

Since there is no closed form solution of Eq.(3.27), except for single look $L = 1$, it should be evaluated numerically. For single look cases, the solution to Eq. (3.27) is (Tough, 1991)

$$\sigma_{\underline{\phi}(L=1)} = \frac{\pi^2}{3} - \pi \arcsin(|\gamma| \cos(\phi_0)) + \pi \arcsin(|\gamma| \cos(\phi_0))^2 + Li_2(|\gamma|)^2, \quad (3.28)$$

where Li_2 is Euler's dilogarithm and is computed as

$$Li_2(x) = \sum_{k=1}^{\infty} \frac{x^k}{k^2}. \quad (3.29)$$

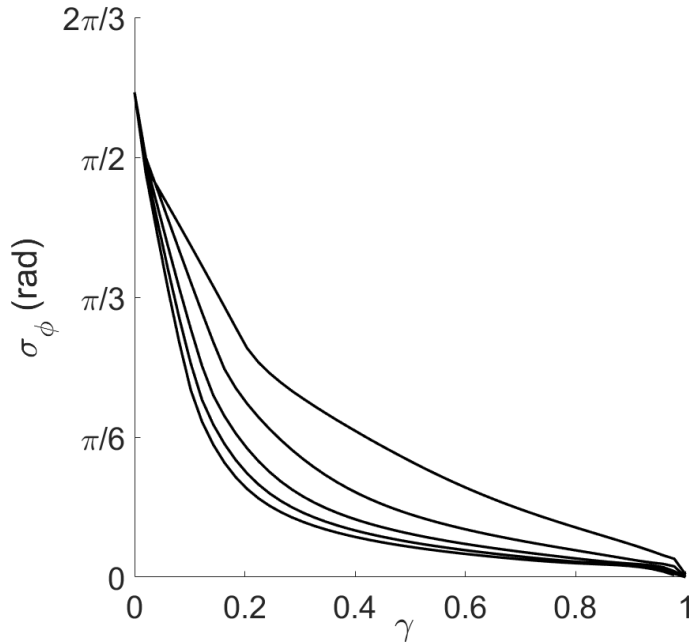


Figure 3.6: Standard deviation $\sigma_{\underline{\phi}}$ of the interferometric phase (based on Eq. (3.27)) as a function of coherence. Different values for the multilook factor L have been used ($L=10,30,60,90,120$ from top to bottom).

In Figure 3.6, Eq. (3.27) is evaluated numerically for different multilook values. It can be seen that the higher the multilook factor, the lower the standard deviation of the phase. However, the decrease in standard deviation from $L = 10$ to $L = 30$ is larger as compared to the decrease in standard deviation from $L = 30$ to $L = 60$. At zero coherence, all different curves have a phase standard deviation of $\pi/\sqrt{12}$ which is the standard deviation of a uniform distributed variable between $-\pi$ and π .

3.2.4. Small Baseline Subset Algorithm

One of the first DSI time series methodologies is called The Small Baseline Subset Algorithm (SBAS) and was developed by Berardino et al. (2002). The principle is to only use small baseline interferograms to limit the decorrelation and increase the spatial point density (with respect to PSI). $N+1$ SAR images are considered at the time epochs $(t_0, t_1, t_2, \dots, t_N)$, t_0 being the reference with zero deformation. The technique uses M unwrapped interferograms which are corrected for topography using a Digital Elevation Model (DEM). These interferograms form the linear model

$$A\phi = \delta\phi, \quad (3.30a)$$

$$\phi = [\phi^1, \dots, \phi^N], \quad (3.30b)$$

$$\delta\phi = [\delta\phi^1, \dots, \delta\phi^M], \quad (3.30c)$$

in which ϕ is a vector with the N unknown phase values and $\delta\phi$ is a vector containing the M computed interferograms. The A-matrix in Eq. (3.30a) is an incidence matrix used to define the combinations of phases to produce the interferograms. Suppose we would have $\delta\phi^1 = \phi^3 - \phi^2$, $\delta\phi^2 = \phi^4 - \phi^1$ and $\delta\phi^3 = \phi^2 - \phi^0$ then the A-matrix would look like

$$A = \begin{bmatrix} 0 & -1 & 1 & 0 & \dots \\ -1 & 0 & 0 & 1 & \dots \\ 0 & 1 & 0 & 0 & \dots \\ \vdots & \vdots & \vdots & \vdots & \ddots \end{bmatrix} \quad (3.31)$$

Depending on N and M, the system can be overdetermined ($M > N$), well determined solution ($M = N$) or is rank deficient ($M < N$). If M is equal or larger than N, the system is easily inverted using a general Least-Squares inversion

$$\hat{\phi} = (A^T A)^{-1} A^T. \quad (3.32)$$

However, if different small baseline subsets are created, A is rank deficient. Berardino et al. (2002) then uses a Singular Value Decomposition (SVD) with a minimum norm solution to invert the system. The atmospheric phase component is removed after the SVD procedure following a similar approach as with PSI. The model can easily be extended with a predefined deformation model.

In their paper, Berardino et al. (2002) applied their algorithm to the active caldera of Campi Flegrei using data from the ERS-1/ERS-2 (C-band) between June 8, 1992 and September 28, 2000. Using multilooking factors of four in range and 20 in azimuth, Berardino et al. (2002) were able to show significant deformation on the Campi Flegrei caldera.

Advanced SBAS

Disadvantages of the SBAS method are that the spatial resolution is low and that it is prone to phase unwrapping errors (Goel, 2012). In her PhD thesis, Goel developed an advanced SBAS approach with a focus on natural terrains. Goel (2012) made two improvements with respect to the SBAS method as introduced by Berardino et al. (2002). The first one is applying adaptive multilooking using only SHP to make sure only pixels which have the same statistical properties are used in the filtering. The second improvement is made in the estimation of deformation time series. The SBAS method as described in Berardino et al. (2002) uses a L2 minimum norm solution which can lead to phase unwrapping errors in decorrelated areas. A L1-minimum norm inversion resulted in higher residuals as compared to the L2 inversion. These residuals can be used to detect and correct outliers which makes the phase unwrapping more robust. A case study was performed on a natural gas storage reservoir located in Germany. The point density in the time series obtained with the advanced SBAS approach (with adaptive complex multilooking and using the L1-norm inversion) significantly improved with respect to the conventional SBAS method. A big advantage of this method is that no predefined deformation model is required, which makes the technique suitable for non-linear deformation estimation. However, coherent patches are separated by the decorrelated areas, which often leads to phase unwrapping errors.

3.2.5. SqueeSAR

A method which aims to combine the Point Scatterers (PS) together with Distributed Scatterers (DS) was introduced by Ferretti et al. (2011). If a strong reflecting object is present in a SAR image, which dominates the reflection, other objects just introduce noise which is called clutter. PS stay coherent over time, even for large baselines. DS are strongly affected by decorrelation, but for small baselines may still contain coherent information (Samiei-Esfahany, 2017). Just as for the advanced SBAS method, statistical homogenous pixels (SHP) are selected based on a statistical test. In their paper, Ferretti et al. (2011) select a window in which the two-sample Kolmogorov-Smirnov test is used (on amplitude data) to decide whether two pixels arise from the same distribution or not. They also mentioned that the KS test is probably the easiest option and that it might be interesting to consider the Anderson-Darling test for SHP selection. The following steps describe the selection of SHP.

- Define an estimation window for each image pixel P for which SHP have to be identified.
- Based on the Kolmogorov-Smirnov test, pixels are selected which show the same statistical behavior as P based on a certain level of significance.
- Image pixels which are not directly connected to P are discarded from the set.
- All selected SHP (including pixel P) within the estimation window (identified as Ω) are considered to belong to the same distribution and can be used for further analysis.

Having a set of SHP for pixel P (assuming a zero-mean complex Gaussian PDF), the sample covariance matrix can be estimated as

$$Q_{yy} \approx \frac{1}{\Omega} \sum_{P \in \Omega} d(P)d(P)^H, \quad (3.33)$$

in which $d(P)$ is a complex data vector which contains the complex reflectivity values of pixel P for all N images.

$$d(P) = [d_1(P), d_2(P), \dots, d_N(P)]^T. \quad (3.34)$$

The difficulty with filtered data is that the 3-D phase unwrapping algorithms cannot be applied (Ferretti et al., 2011). The coherence matrix is not redundant and phase consistency does not hold for the complex multi-looked pixels (see Figure 3.7).

$$\theta^{nj} \neq W\{\theta^{nm} - \theta^{mj}\}. \quad (3.35)$$

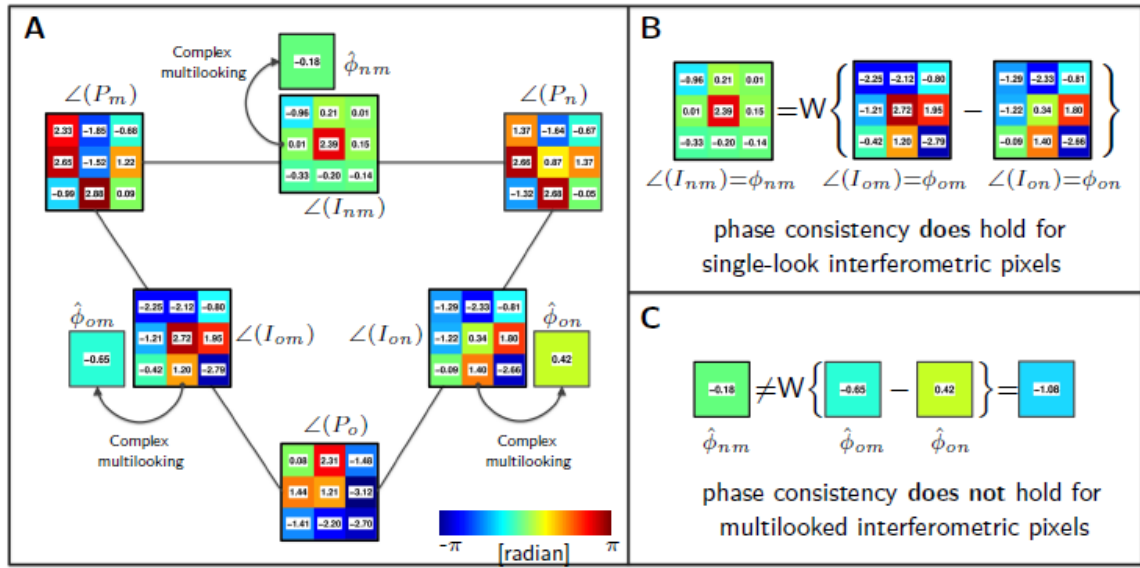


Figure 3.7: Illustration of phase inconsistency. **A** Three interferograms constructed from the SLC's $\langle P_m \rangle$, $\langle P_n \rangle$, $\langle P_o \rangle$ with the corresponding multi-looked phases. **B** Illustration of phase consistency for non multi-looked pixels. **C** Illustration of phase inconsistency for multi-looked pixels. Figure from Samiei-Esfahany (2017).

Assuming that the signal components are constant within the averaging window, Eq.(3.35) can be written as the expectation of the phase consistency (Samiei-Esfahany, 2017).

$$E[\hat{\theta}^{nj}] = W[\theta^{nm} - \theta^{mj}]. \quad (3.36)$$

This expectation holds for every interferogram and can be written in the form of a system of equations

$$E[y] = W[Ax], \quad (3.37)$$

in which the observation vector y contains the known multi-looked phases, A is the matrix which defines the interferometric combinations (maximum of $N(N-1)/2$) and x is the vector with unknown parameters

to be estimated. This system of equations is highly non-linear and the process of finding the optimal estimate for the multi-looked phase is called Equivalent Single Master (ESM) phase estimation. There are several approaches to solve this problem. Ferretti et al. (2011) uses an approach in which the solution to Eq.(3.37) is found by a maximum-likelihood approach which is called "phase-linking". Fornaro et al. (2015) uses Principle Components Analysis (PCA) not only to restore the phase inconsistency but also to extract possible multiple scattering mechanisms. Samiei-Esfahany (2017) uses Integer Least-Squares (ILS) in which the non-linear system is made linear by introducing integer ambiguities. Only pixels which have more SHP than a threshold are considered as DS pixels such that the phases of PS pixels are preserved. After the ESM phase estimation step, the phases of DS pixels are changed in the original interferograms which can then be used in a traditional PSI algorithm.

3.2.6. Advanced DSI technique

Goel (2012) proposed a new technique to process DS pixels because of limitations of existing methodology. The SBAS methodology is prone to local phase unwrapping errors which are difficult to detect in data with fringe discontinuities. Also, offsets of integer multiples of 2π can occur if coherent patches are separated by severely decorrelated areas such as forests or water. The SqueeSAR approach on the other hand, uses all possible interferograms which makes it computationally expensive. Therefore, Goel (2012) developed a new model to process DSI pixels, hereafter called the advanced DSI-method. The advantages of this new method with respect to algorithms such as SBAS and SqueeSAR are:

- No spatial phase unwrapping is necessary because the approach estimates velocity gradients which are then integrated to obtain the 2D velocity field.
- The computational complexity is reduced compared to SqueeSAR because only small baseline differential interferograms are used.
- DEM errors and atmospheric artifacts are compensated, even if the data contains high noise values.
- The deformation and topographic components can be used directly for integration, in contrast to SBAS where the need for deformation estimation after phase unwrapping is susceptible to errors.

The first step of the algorithm is (comparable to SqueeSAR) to group pixels with similar scattering properties. For this the Anderson-Darling test is used. The minimum patch size is equal to 20 pixels and for the coherence a threshold of 0.3 has been set. A bigger patch size (e.g. 400 pixels) is used in the case studies to obtain a more precise estimation.

The second step is to estimate for each DS the LOS deformation velocity and residual DEM. The local gradients of the deformation velocity are estimated for each SHP, approximating the deformation velocities in range and azimuth as being linear. A phase model is used for the parameter estimation, which consists of deformation and residual topography phase components

$$\phi_{DInSAR_model}^{i,k} = \left(\frac{4\pi}{\lambda} B_t^k m_{v_x} p_x^i + \frac{4\pi}{\lambda} B_t^k m_{v_y} p_y^i \right) + \left(\frac{4\pi}{\lambda} \frac{B_{\perp}^k}{R \sin \theta} m_{h_x} p_x^i + \frac{4\pi}{\lambda} \frac{B_{\perp}^k}{R \sin \theta} m_{h_y} p_y^i \right), \quad (3.38)$$

where m_{v_x} and m_{v_y} are the local deformation velocity gradients (mm/year/pixel) and m_{h_x} and m_{h_y} are the residual DEM local gradients (m/pixel) in range (x) and azimuth (y) directions. p_x^i and p_y^i are the pixel indices relative to the reference pixel indices. $i = 1, \dots, L$ (L is the number of SHP pixels in the window) and $k = 1, \dots, M$ (M being the number of interferograms). All SHP pixels within the window are then used for parameter estimation using the following periodogram function which maximizes the coherence.

$$\zeta(m_{v_x}, m_{v_y}, m_{h_x}, m_{h_y}) = \frac{1}{M} \sum_{k=1}^M \left(\frac{1}{L} \left| \sum_{i=1}^L e^{j(\phi_{DInSAR_obs}^{i,k} - \phi_{DInSAR_model}^{i,k})} \right| \right). \quad (3.39)$$

The maximum of ζ is then the temporal coherence of a DS window. The range of values for m_v and m_h for which a maximum is searched in the periodogram function can be based on prior knowledge or (if no prior knowledge is available) a range of [-1, 1] mm/year/pixel is a good search range. The estimation precision is dependent on the amount of SHP, the number of interferograms and the average spatial coherence of the patch.

The last step is to obtain the deformation velocity by integration of the 2D deformation field under the assumption that the deformation velocity between neighboring windows varies smoothly. As an example, in Figure 3.8 a visualization is depicted of a 1D integration of the velocity field. Under the assumption that the deformation varies smoothly, the linear deformation estimates of the different patches can be integrated to obtain an absolute estimate.

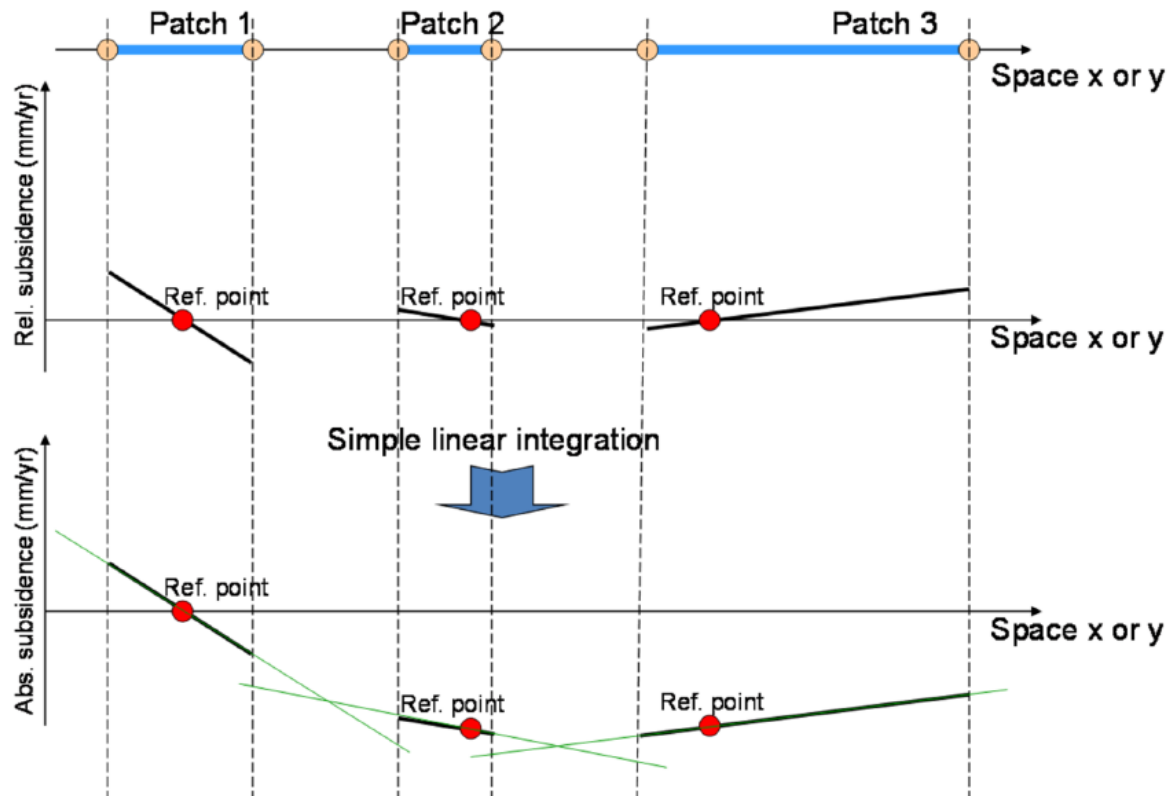


Figure 3.8: Example of 1D velocity integration, using the advanced DSI technique (Goel, 2012). The different isolated patches are connected by using a simple linear integration technique to obtain an estimate of the deformation with respect to a single reference point.

In the test case, Goel (2012) uses a predefined elliptical subsidence bowl to estimate the deformation of an area in Germany which is used for salt mining. To estimate the parameters of the assumed model, a Bayesian interference approach has been used. A minimum number of 400 SHP was set to estimate the deformation, using windows of 24m by 24m. Compared to the advanced SBAS method in their study, the advanced DSI method provided much denser deformation velocity estimates because of the deformation model of the area was known. Also, precision of the deformation velocity estimates can be obtained because of the Bayesian interference method. The need to provide a deformation model is also a disadvantage of this method because information of the considered area is needed. In her paper, Goel (2012) acknowledges this limitation and states that future work should concentrate on making this new method model-free.

3.3. Summary

In this chapter we have discussed two types of time series interferometry methodologies, Persistent Scatterer Interferometry (PSI) and Distributed Scatterer Interferometry (DSI). PSI can be, and is already, used to estimate deformation time series for objects which have stable radar reflections in the considered time frame. The deformation signal can be separated from the other phase contributions by making use of the different temporal and spatial behavior of these parameters. StaMPS is an alternative of PSI and is able to estimate deformation on bare grounds.

Often, with PSI techniques, no coherent phase information can be obtained on vegetated areas because of temporal decorrelation. These pixels can be classified as Distributed Scatterers (DS) and techniques which exploit these DS are called Distributed Scatter Interferometry (DSI) methods. The Small Baseline Subset Algorithm (SBAS) is such a DSI method which only uses small temporal baselines to reduce the temporal decorrelation. If this restriction of small baselines leads to different subsets of interferograms, a Singular Value Decomposition is used to link the subsets together. Often the phases are multi-looked to decrease the phase noise. A spatial adaptive multilook window can be used in which the statistical properties of the pixels are used to find Statistical Homogenous Pixels (SHP). In this way, only pixels which show similar amplitude behavior over time are used for complex multilooking.

SqueeSAR is an algorithm in which DS are processed together with PS in a traditional PS InSAR processing chain. The phase inconsistency introduced by the multilook operation is restored by applying an Equivalent Single Master phase estimation step which reduces the decorrelation noise. Goel (2012) estimates local gradients of deformation velocity and residual topography, only using small baseline interferograms. The deformation map is then obtained by integrating the gradients based on a deformation model.

To estimate deformation velocity, in this thesis, use is made of both PS and DS. The DS are referred to the closest PS such that the atmospheric phase is canceled. Statistical Homogenous Pixel (SHP) selection is an important aspect that forms the basis for the estimation of the coherence matrix, which is extensively used in the derived methodology. In Chapter 4 it is tested whether indeed the atmospheric phase can be neglected when using phase differences over short distances. Next, in Chapter 5, a method is developed to estimate relative deformation of a DS with respect to a nearby PS. This model can be classified as a DSI technique, but uses results of a PSI analysis to locate the PS. The developed methodology will be applied on TerraSAR-X and Radarsat-2 data in Chapter 6.

4

SAR Data analysis

The goal of this research is to estimate a deformation signal on the vegetated part of a dike. To do so, pixels on the vegetated part of the dike are related to nearby PS to reduce the noise. The aim of this chapter is to get an understanding of the phase noise and spatial correlation. The phase noise is analyzed to justify the assumption that atmospheric effects and orbital errors are negligible over small distances. Understanding spatial correlation between pixels is important to determine if an estimate of relative deformation consists of independent observations. The Marken island is used as a case study, for which TerraSAR-X and Radarsat-2 data is available.

4.1. Case study

The PSI methodology has proven to be successful in deformation estimation on water defense structures (Hanssen and van Leijen, 2008b). However, the points for which these deformation time series are estimated (PS) are usually situated on the revetment part of the dike. The obtained deformation estimates may or may not be representative for the whole dike. Therefore, as a case study, the dike of Marken is chosen which has a revetment part at the outer side and grass cover at the inner side of the dike. Marken is located in the Netherlands and is a former Island in the IJssel Lake but is connected to land in 1957, making it a peninsula. 166 radar images obtained by the TerraSAR-X satellite in ascending orbit are used from February 2009 until February 2016. In Figure 4.2, an overview of the Marken Island is depicted as well as the cropped area which is used in this thesis to limit computation time. This crop is selected because the flight direction of the satellite (for both TerraSAR-X and Radarsat-2) is approximately perpendicular to the dike (see Figure 4.6 for the ground tracks of TerraSAR-X and Radarsat-2). In this way, there is a limited effect of foreshortening on the outer and inner slopes of the dikes which makes the interpretation of the results more convenient (see section 2.2.1). A cross section of the dike is shown in Figure 4.1.

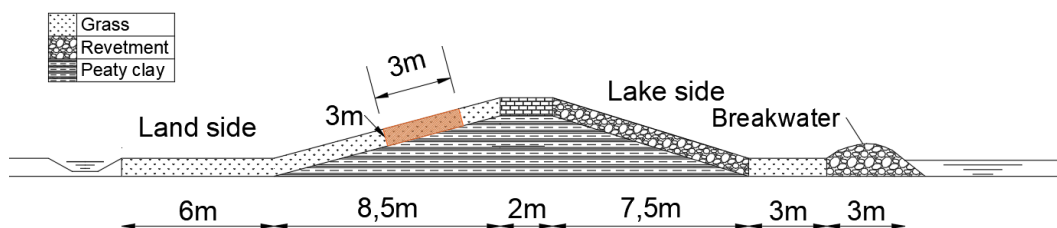
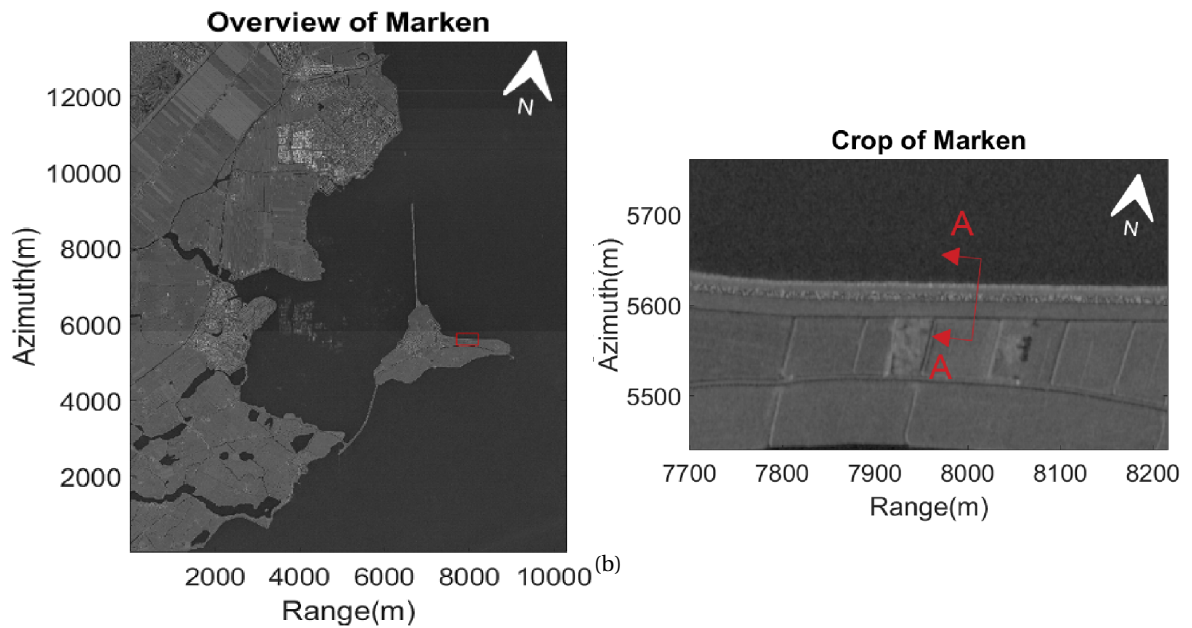


Figure 4.1: Marken dike cross section A-A (own work). In orange an example of a resolution cell from the TerraSAR-X satellite is shown (which has a resolution of 3 meter in range and 3 meter in azimuth).



(a)

Figure 4.2: Overview of the case study on the Marken island, in radar coordinates. **(a)** 166 TerraSAR-X images are used from February 2009 until 2016 to calculate the Mean Reflectivity Map (MRM) of Marken. **(b)** MRM of cropped area with the cross section A-A as shown in Figure 4.1.

Pictures of both the lake side (Figure 4.4a) and the land side (Figure 4.4b) show the different types of surface cover on the dike. At the outer side of the dike, the slope is covered with revetment which often provides stable radar reflections. On the inner side of the dike, the slope is grass-covered which makes the properties of the surface (and thus the radar reflections) variable within a year. On the top of the dike, a small road is made from stones for pedestrians and cyclists (Figure 4.3)



Figure 4.3: Top of Marken dike (Google Maps).



(a)

(b)

Figure 4.4: Pictures of the Marken dike. (a) Marken dike revetment outer side. (b) Marken dike grass cover inner side.

4.1.1.1. TerraSAR-X data

TerraSAR-X is a commercial SAR satellite and was launched at June 2007 with an initial life time expectancy of 7 years but was extended by 5 years, enabling SAR acquisitions until 2019. The TerraSAR-X mission (together with tanDEM-X) are realized by a combination between the German government and the German Aerospace Center (DLR). The orbit is Sun-synchronous with an repeat period of 11 days. The altitude at the equator is 514 km, the inclination angle is equal to 97.4 degrees (see Figure 4.6) and the sensor operates at X-band (0.03 m wavelength). Acquisitions in different imaging modes can be obtained, as is shown in Figure 4.5.

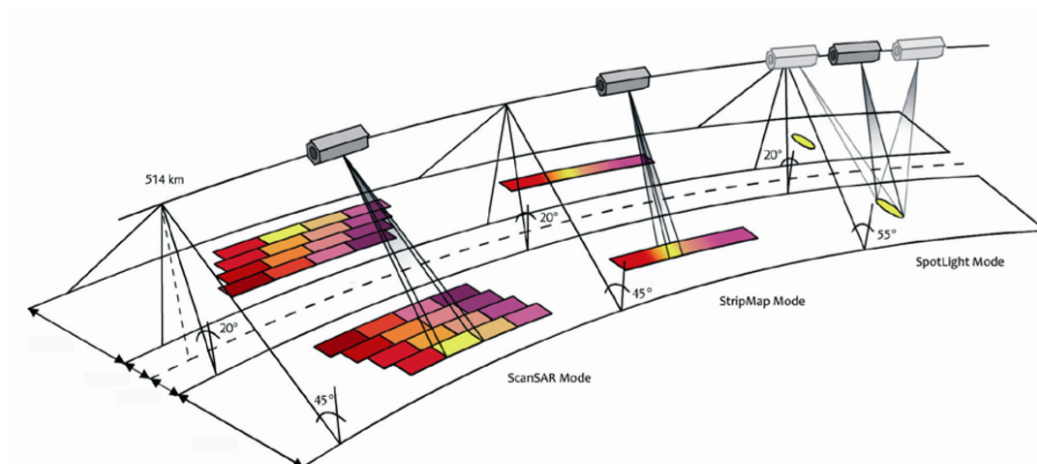


Figure 4.5: TerraSAR-X imaging modes (Airbus, 2014).

In the ScanSAR imaging mode, slightly overlapping images with different incidence angles are processed into one scene using electronic antenna elevation steering. The scene size is 100 x 150 km with range resolution of 1.2 m and azimuth resolution of 18.5 m. The StripMap (SM) mode is the basic SAR imaging mode. The antenna beam is fixed in azimuth and elevation and continuously illuminates the surface. The

scene size is 30km x 50km for single polarization (dual polarization 15 km x 50 km), with a range and azimuth resolution of 1.2 m and 3.3 m. The SpotLight (SL) mode increases the illumination time and has the highest resolution (1.2 m in range and 1.7 m in azimuth) but the scene size is restricted to 10 km x 10 km. Variants of the SL mode are High Resolution SpotLight (HS) mode (range resolution of 0.6 m and azimuth resolution of 1.1 m). and Staring Spotlight mode (ST) mode (range resolution 0.6 m and azimuth resolution 0.24 m). The products as delivered by DLR can be divided in two classes, Slant Range Products and Detected products. The Single Look Slant Range Complex (SSC) product is a single look product of the focused radar signal and is used for applications which require full bandwidth and phase information (SAR Interferometry). In the detected products the noise is decreased by performing a complex multilook operation, leading to a reduction in resolution. The detected products are all projected in ground range and azimuth coordinates with the WGS84 as reference ellipsoid.

In this thesis, the SSC products are acquired between 5 February, 2009 and 1 February, 2016. The centre of the scene is situated on 52.5 degrees latitude and 4.92 degrees longitude. The SSC's are processed by Delft object-oriented radar interferometric software (DORIS) to obtain interferograms. First, the images are oversampled and DORIS co-registers the slave images such that it has the same grid as the master image. The complex interferogram is computed from which the reference phase of the ellipsoid is subtracted. The reference phase of the SRTM Digital Elevation Model (DEM) is computed and subtracted from the interferogram. The interferograms as computed by DORIS can then be used for further analysis. In the next subsection, a DePSI (Delft Persistent Scatterer Interferometry) analysis is performed on the selected case study.



Figure 4.6: Example of satellite ground tracks projected on an aerial photo of Google Maps. In red, the track of the TerraSAR-X satellite is shown in ascending orbit (inclination angle 97.4 degrees). In blue, the track of the Radarsat-2 satellite is shown in descending orbit (inclination angle of 98.6 degrees).

PSI analysis

As an illustration of the current possibilities to estimate deformation on dikes, a PSI analysis is performed using the Delft software DePSI (Delft Persistent Scatterer Interferometry). Data from February 2009 until February 2016 are used with the master image acquired at the 12th of March, 2013. Figure 4.7a displays the estimated linear deformation velocities (mm/year) for a crop of the dike. Figure 4.7b displays the deformation time series for one PS (red arrow in Figure 4.7a) together with the estimated Least-Squares linear fit. The PS as found by DePSI are located at the lake side of the dike (above the green line), which is covered with revetment. The deformation velocities of the PS on the dike are all negative, which means the dike is subsiding with respect to the reference point. To compare sensors with different wavelengths, also Radarsat-2 data is used, of which characteristics will be explained in the following section.

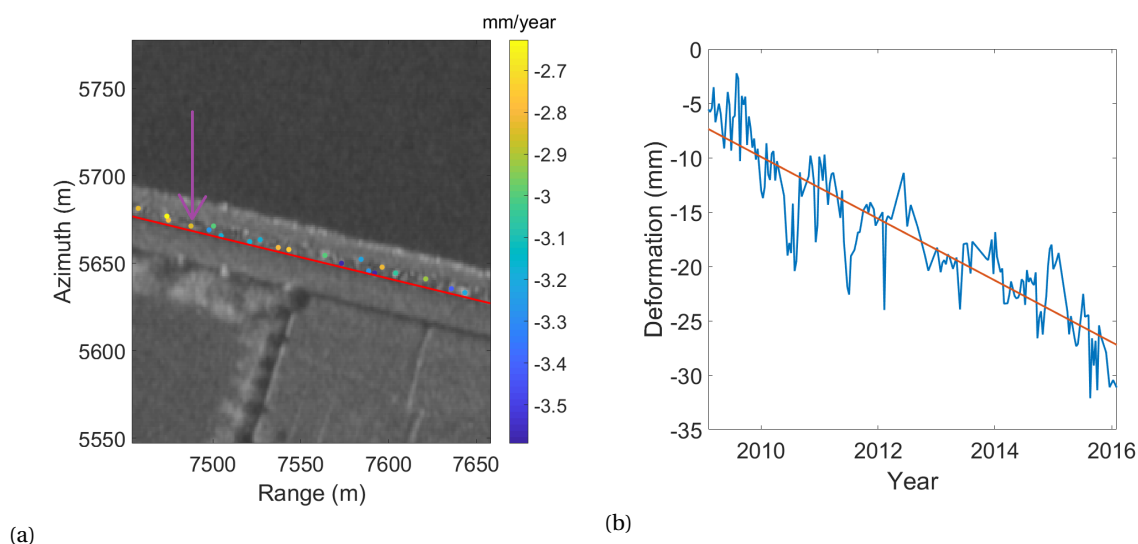


Figure 4.7: Visualization of a PSI analysis using the software Delft Persistent Scatterer Interferometry. 166 images from the TerraSAR-X satellite are used from February 2009 until February 2016. **(a)** Overview of estimated linear deformation rates on the Marken crop (the red line represents the intersection between the revetment and grass cover). **(b)** Example of one PS time series with the estimated linear trend.

4.1.2. Radarsat-2

Radarsat-2 is a Canadian commercial radar satellite launched in December 2007 to follow up Radarsat-1 (which orbited the Earth from 1995 up to 2013). The satellite has a C-band sensor (wavelength of 0.055 m) and has multiple polarization modes. The revisit time is 24 days and the satellite flies at an altitude of 800 km with an inclination of 98.6 degrees (see Figure 4.6). Application for which Radarsat-2 data is used are ice, marine surveillance, disaster management, Hydrology, Agriculture and Forestry (CSA, 2015). In Figure 4.8 the different imaging modes of the Radarsat-2 satellite are depicted, ranging from high resolution (Spotlight) to low resolution (ScanSAR wide). In this thesis, data is used from the Extra-Fine imaging mode. The resolution in range is 5.0 m and in azimuth 2.8 m. 48 Single Look Complex (SLC) images are used from March 2015 up to August 2018.

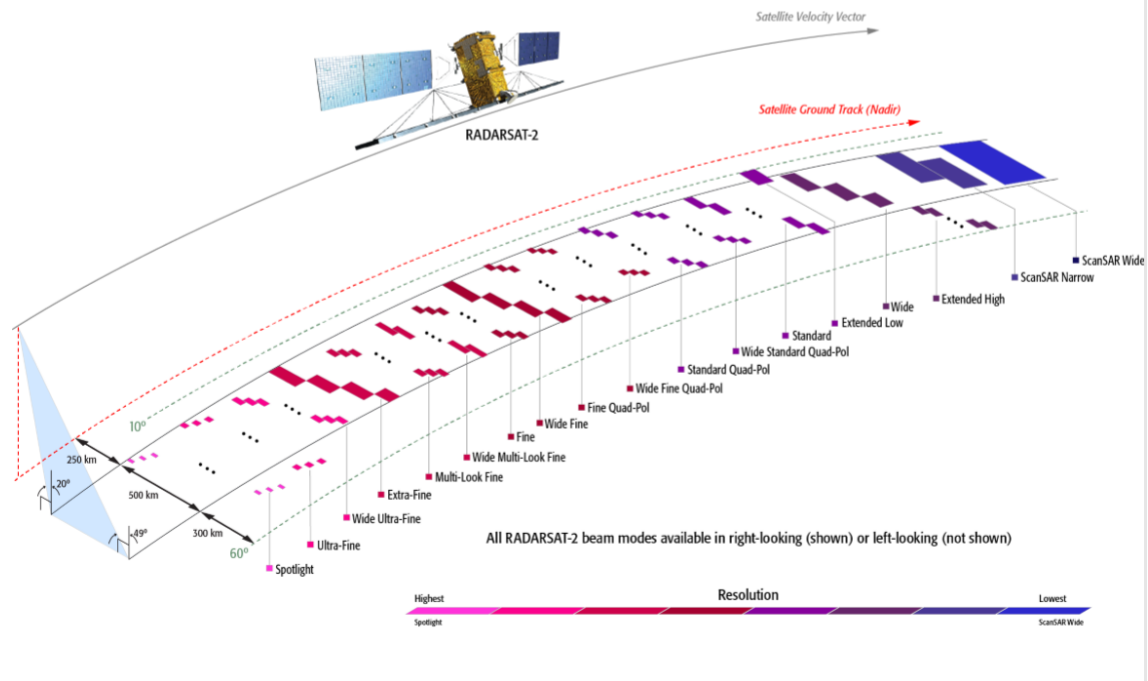


Figure 4.8: Radarsat-2 imaging modes (CSA, 2015).

PSI analysis

Just as for the TerraSAR-X stack, a PSI analysis is performed with the Radarsat-2 data stack. Estimated linear deformation rates are visualized in Figure 4.9a, of which for one point the time series is shown in Figure 4.9b. It is emphasized that the results of both calculations cannot be compared (directly) with each other due to the different time frame of the data stacks. Using the PSI analysis on the Radarsat-2 stack, PS are found on the crest of the dike as well as on the shore protection. The estimated deformation rates are all negative but have a somewhat larger spread as compared to the TerraSAR-X data. This may be the result of the different time intervals of the data stacks. The next subsection aims to quantify the amount of noise that is present in double differences. The PS points as found by DePSI are used as a reference to relate the phases of other pixels to.

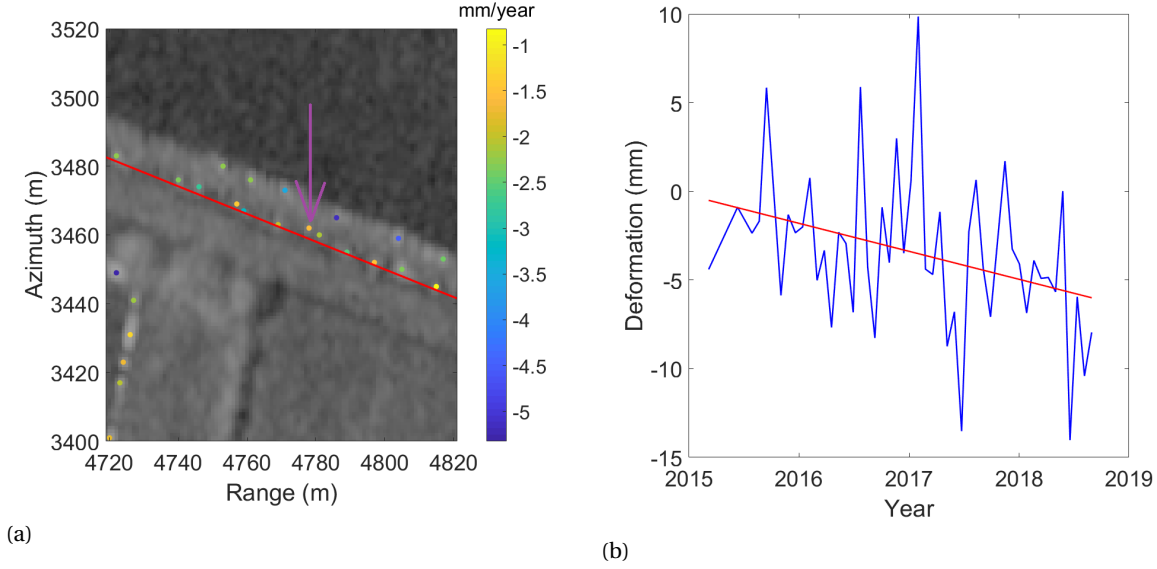


Figure 4.9: Visualization of a PSI analysis using the software Delft Persistent Scatterer Interferometry. 48 images acquired with the Radarsat-2 satellite from March 2015 until August 2018 are used. (a) Overview of estimated linear deformation rates on the Marken crop (the red line represents the intersection between the revetment and grass cover). (b) Example of one PS time series with the estimated linear trend.

4.2. Double differences

An interferogram is obtained if one SLC image is multiplied with the complex conjugate of another SLC image. However, this quantity does not contain any relevant geometric information. The atmospheric delay is in the order of several meters, orbit errors in the order of several centimeters and the ambiguities, which makes claims of sub-centimeter accuracy impossible (Hanssen, 2004). Relevant information is obtained only when differences of pixels within a resolution cell (double differences) are considered. These differences are called double differences because the differences are both in time and space. The smaller the distance between the pixels, the more noise (in terms of the atmospheric phase and orbital errors) are canceled. In Eq.(4.1), the double differences are formulated for SLC data which is corrected for the flat earth phase and for which a SRTM model is used to make a rough correction for topography (The subscripts indicate the spatial domain and the superscripts the temporal domain).

$$\phi_{12}^{12} = \phi_1^{12} - \phi_2^{12} = W\{\phi_{12,D}^{12} + \phi_{12,T}^{12} + \phi_{12,A}^{12} + \phi_{12,O}^{12} + \phi_{12,N}^{12}\}, \quad (4.1a)$$

where,

$$\phi_1^{12} = W\{\phi_1^1 - \phi_1^2\} = W\{\phi_{1,D}^{12} + \phi_{1,T}^{12} + \phi_{1,A}^{12} + \phi_{1,O}^{12} + \phi_{1,N}^{12}\}, \quad (4.1b)$$

and

$$\phi_2^{12} = W\{\phi_2^1 - \phi_2^2\} = W\{\phi_{2,D}^{12} + \phi_{2,T}^{12} + \phi_{2,A}^{12} + \phi_{2,O}^{12} + \phi_{2,N}^{12}\}, \quad (4.1c)$$

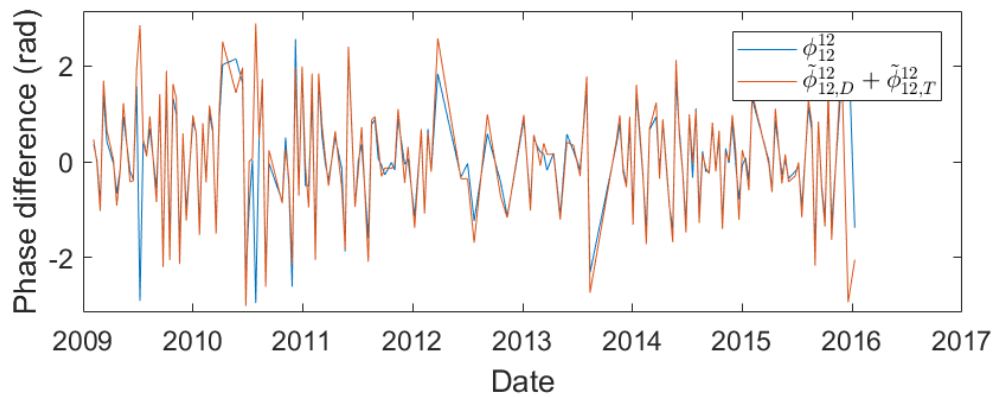
where ϕ_{12}^{12} is the interferometric phase difference between pixel 1 and 2 and consists of $\phi_{12,D}^{12}$, $\phi_{12,T}^{12}$, $\phi_{12,A}^{12}$, $\phi_{12,O}^{12}$ and $\phi_{12,N}^{12}$, which are the differences in interferometric phase between pixel 1 and pixel 2 due to deformation, topography, atmosphere, orbit errors and noise, respectively.

Separating the atmosphere and orbital errors from the data

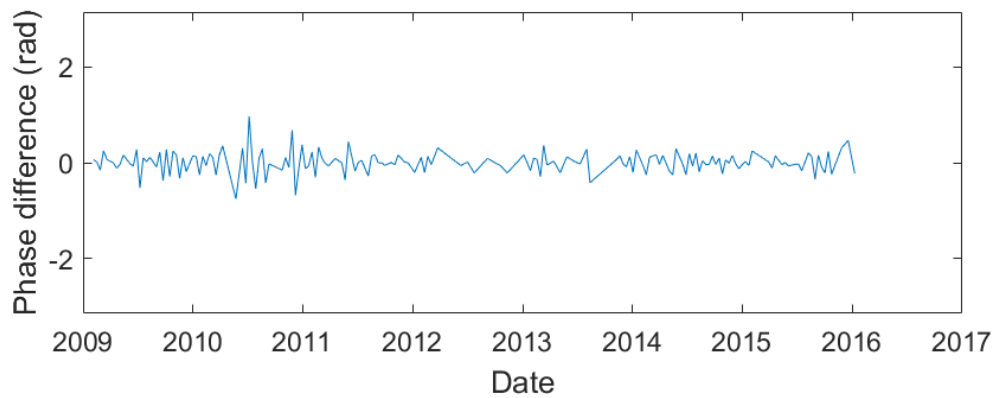
As described in the previous section, a large portion of noise terms is canceled by using double differences over short distances. In this section the magnitude of the residual phase between two pixels is investigated by using results of a PSI analysis. Using the DePSI processing, the deformation velocity as well as the residual topographic height is estimated, which can be formulated in the phase domain by using Eq. (2.11) and Eq. (2.17), respectively. In Eq. (4.2), the relative deformation and residual topographic phase are subtracted from Eq.(4.1a).

$$\phi_{12}^{12} - \tilde{\phi}_{12,D}^{12} - \tilde{\phi}_{12,T}^{12} \approx \phi_{12,A}^{12} + \phi_{12,O}^{12}, \quad (4.2)$$

In which $\tilde{\phi}_{12,D}^{12}$ and $\tilde{\phi}_{12,T}^{12}$ are the relative deformation and relative residual topographic phases between the two PS, estimated by DePSI. To assess the magnitude of the two terms $\phi_{12,A}^{12}$ and $\phi_{12,O}^{12}$, Eq. (4.2) is visualized in Figure 4.10 for two PS pixels in the area of interest.



(a)



(b)

Figure 4.10: Visualization of daisy chain interferometric phase differences between two PS pixels (Eq. (4.2)). (a) In blue, the relative deformation phase and relative residual topographic phase between two PS as estimated by DePSI. In red, the wrapped daisy chain interferometric phase between two PS for the original data. The correlation between the two curves is 0.77 (b) The wrapped difference between the two curves in (a). The standard deviation is equal to 0.23 radians, which indicates that (over short distances) the influence of the atmosphere and orbit errors are rather small.

The blue line in Figure 4.10a is the (wrapped) daisy chain interferometric phase between the two PS for the original data. In red, the difference in deformation between the two PS as estimated by DePSI is shown as the (wrapped) daisy chain interferometric phase. There is not much difference between the blue and red line, indicating that the magnitude of $\phi_{12,A}^{12}$, $\phi_{12,O}^{12}$ and $\phi_{12,N}^{12}$ is relatively small. On a few points in the graph, it seems that the difference between the red and blue line is quite large, but in reality this difference is small because the phases are wrapped. In Figure 4.10b the wrapped difference between the red and blue line is depicted. The phase terms left in this residual phase are the (relative) atmospheric phase, orbital phase, scattering noise and residues because the assumed deformation model does not exactly match with reality. As already could be seen in Figure 4.10a, the difference between the two curves is small (standard deviation of 0.23 radians). This analysis shows that when using the phase difference of two nearby (PS) pixels, the influence of the atmosphere and orbital errors are rather small. This is important, because in Chapter 5 extensive use is made of double differences between nearby pixels. When using double differences over short distances, pixels may be correlated due to several data processing steps. This spatial correlation is investigated in the next section.

4.3. Accessing spatial correlation in data

By using double differences, a large part of the spatial correlated signals such as the atmospheric phase and orbital errors are canceled. There are, however, not only physical reasons why two pixels may be spatially correlated. Due to SAR data pre-processing, spatial correlation is introduced between pixels which has no physical origin. In Chapter 5, double differences are used to estimate relative deformation for which independent measurements are needed. Therefore, in this section the length over which pixels are correlated due to data pre-processing is assessed using an empirical variogram. Two data processing steps which introduce spatial correlation are oversampling and the overlapping of resolution cells.

- **Oversampling:** As a consequence of image formation, the spectrum of the interferogram becomes twice as large as compared to the individual spectra. This results in an aliasing effect which leads to phase noise in the interferogram (Hanssen, 2001). To prevent this, both images have to be oversampled by a factor of two before interferogram formation, leading to correlation in double differences over short distances.
- **Overlapping of resolution cells:** If the sampling frequency is higher as compared to the bandwidth of the chirp (Section 2.2.3), resolution cells will overlap which introduces correlation (Bermon, 2008). This means that the pixel posting (Equation 2.5 and 2.7) is smaller than the pixel resolution (Eq.(2.4) and Eq.(2.6)). In the same thesis, Bermon (2008) found that the correlation in azimuth direction is higher as compared to the range direction, due to the antenna pattern.

Since in this thesis double differences are extensively used, it is important to differ between correlation as a result of oversampling/pixel posting and correlation because of similar scattering mechanisms. The amplitude dispersion of the considered crop is shown in Figure 4.11. Since the measured phases of pixels on water should be uniformly distributed between $-\pi$ and π , it is expected that these pixels are not correlated with each other. If there is correlation, however, this must be the results of above mentioned pre-processing steps.

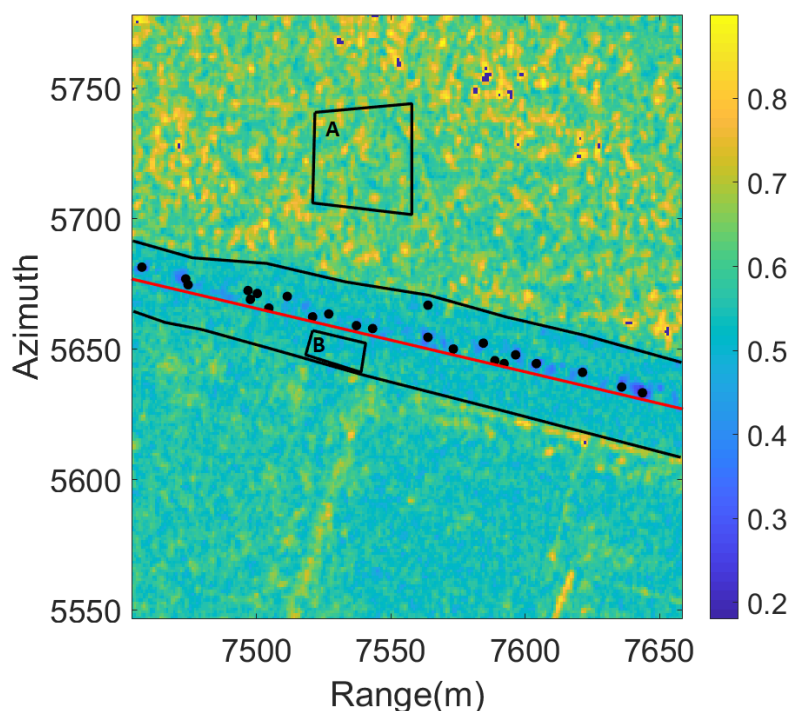


Figure 4.11: Crop selection for empirical variogram on a map with the amplitude dispersion. Two polygons (in black) are drawn in the image, one on the water (A) and one on the vegetated part of the dike (B). The amplitude dispersion is based on 166 acquisitions of TerraSAR-X and is calculated as the standard deviation of the amplitude divided by the mean of the amplitude (see Eq.(3.1)). the red line represents the intersection between the revetment and grass cover, the black dots the PS and the black lines indicate the water boundaries.

To access the length over which pixels are correlated, empirical variograms are estimated for both a crop on the water (A) as well as on the vegetated part of the dike (B) (see Figure 4.11). Pixels on water are expected to be uncorrelated in space (and time) and are therefore suitable to find the distance over which pixels are correlated due to oversampling and posting.

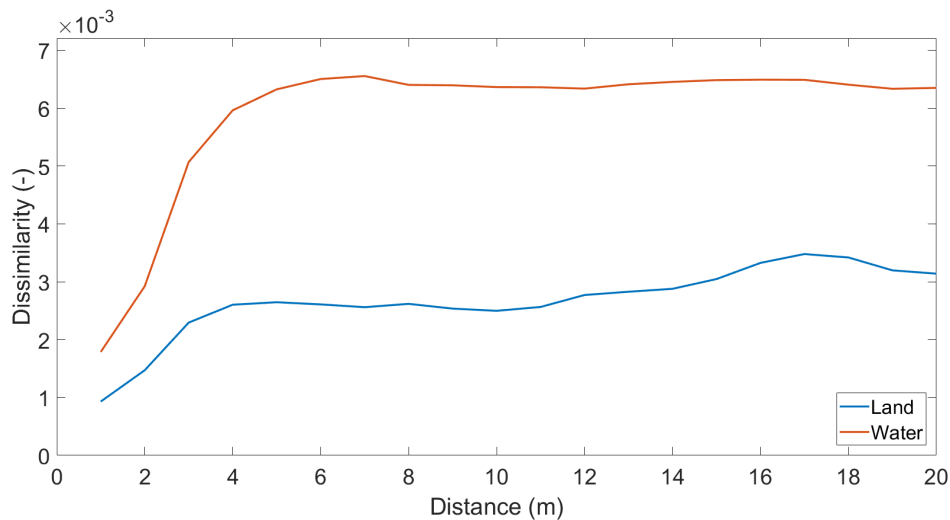


Figure 4.12: Empirical variograms of the amplitude dispersion for an area on water and an area on land (see Figure 4.11). On the x-axis, the distance between the two measurements for which the dissimilarities are calculated. On the y-axis the dissimilarity which is calculated as the squared difference between two measurements (amplitude dispersion). After six meters the dissimilarity stabilizes for the water crop, indicating that after this distance the measurements are independent. This distance is important in analyzing results of the developed methodology.

The variogram is constructed as follows. For each pixel in the considered crop, the dissimilarity is estimated between the pixel and all other pixels. The distance is defined in meters and the dissimilarity is binned in intervals of one meter. The lines in Figure 4.12 are then estimated as the mean of all the dissimilarities per binned interval. It can be seen that the amount of dissimilarity stabilizes after about six meters which means that for smaller distances there is correlation between pixels. The magnitude of the dissimilarity is about 2.5 times larger for pixels on water as compared to pixels on land, indicating that there is information present in the vegetated part of the dike.

The most important conclusions which can be drawn from this chapter are twofold. First, it was shown that by using double differences, the influence of the atmosphere and orbital errors are small. By using results of a PSI analysis, the estimated deformation and residual topography could be subtracted from the data. The standard deviation of the remaining phase contributions (atmospheric phase, orbital errors and noise terms) was relatively low (0.23 radians). This analysis proofed that over small distances, the influence of the atmospheric phase, orbital errors and noise terms are rather small. Secondly, as calculated by using an experimental variogram, there is correlation between two pixels separated by six meters although there is no physical correlation between these pixels. This means that, when observing double differences over short arcs, the phases are not independent. Consequently, as will be shown in Chapter 6, the estimated deformation is close to zero. The RMSE of this fitted deformation is low which would indicate a good fit of the assumed deformation model, while this is actually because of the correlation of these pixels. Keeping these conclusions in mind, the next chapter investigates how double differences can be used to estimate deformation.

5

Methodology

In this chapter a method is proposed which uses coherent interferograms to estimate relative deformation. In Section 5.1 it is investigated how coherent information can be extracted from pixels which in general have low coherence. Subsequently, in Section 5.2, these coherent interferograms are used to estimate relative deformation with respect to PS points which are found with a PSI analysis. In Section 5.3, an approach to evaluate and compare the methods is proposed.

5.1. Coherent interferogram selection

Some pixels are not coherent over the whole time frame but are more coherent for some interferometric combinations. Pixels in vegetated areas could be more coherent in winter as compared to summer because of vegetation growth. As depicted in Figure 5.1a and 5.1b, the coherence on some places changes significantly between two interferograms (The red circle marks the area in which the coherence is changed the most).

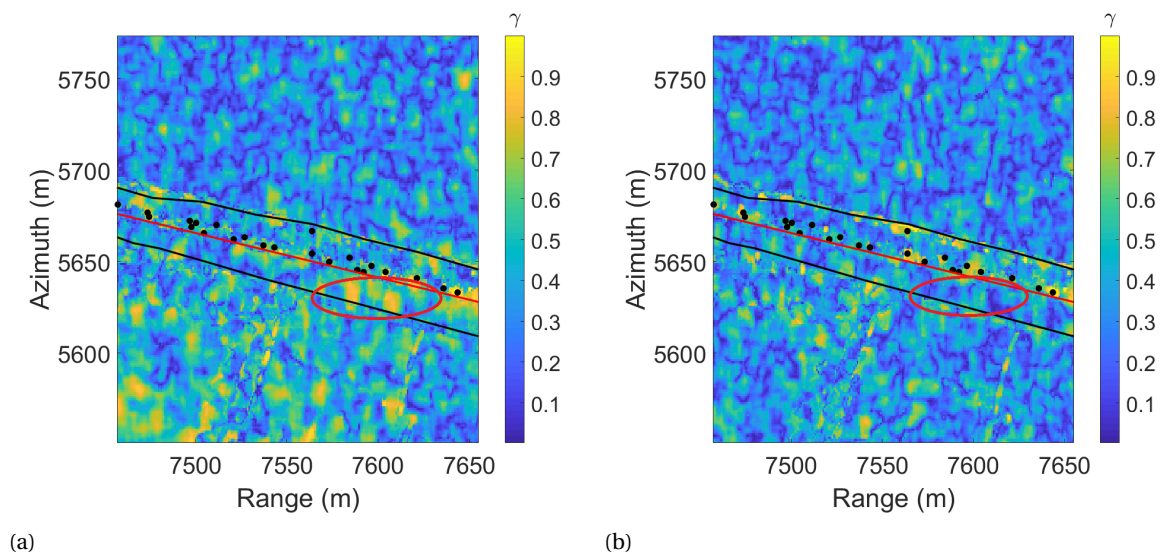


Figure 5.1: Two plots of the estimated coherence, using a 9x9 window and the KS test to select SHP. (a) Coherence between 3 February 2010 and 14 February 2010 and (b) Coherence between 7 July 2010 and 18 July 2010. As depicted in the red ellipses, the coherence can change significantly for two interferograms. the red line represents the intersection between the revetment and grass cover, the black dots the PS and the black lines indicate the water boundaries.

While the pixels within the red circle are not assigned as a Persistent Scatterer, there might still be information in these pixels which can be exploited. To extract these coherent patches from the coherence matrix, three approaches have been investigated (Figure 5.2):

1. **Threshold method:** In this method a threshold is applied on the coherence. All interferograms with a coherence higher than this threshold will be used in the computations (see Figure 5.2a).
2. **Diagonal method:** Only interferograms which have a short temporal baseline (close to the diagonal) are taken into account. These interferograms are most likely to contain coherent information and in this way interferograms far off the diagonal with coincidentally high coherence values are neglected. To prevent interferograms with very low coherence to be taken into account, also a threshold is applied on the coherence values (see Figure 5.2b).
3. **Mean method:** The mean of the coherence matrix (along the rows and columns) must be higher than a certain threshold. In this way, only interferograms are taken into account of SLC's which in general form high coherent interferograms. Just as with the Diagonal method, also a threshold is applied on the coherence values (see Figure 5.2d and 5.2d).

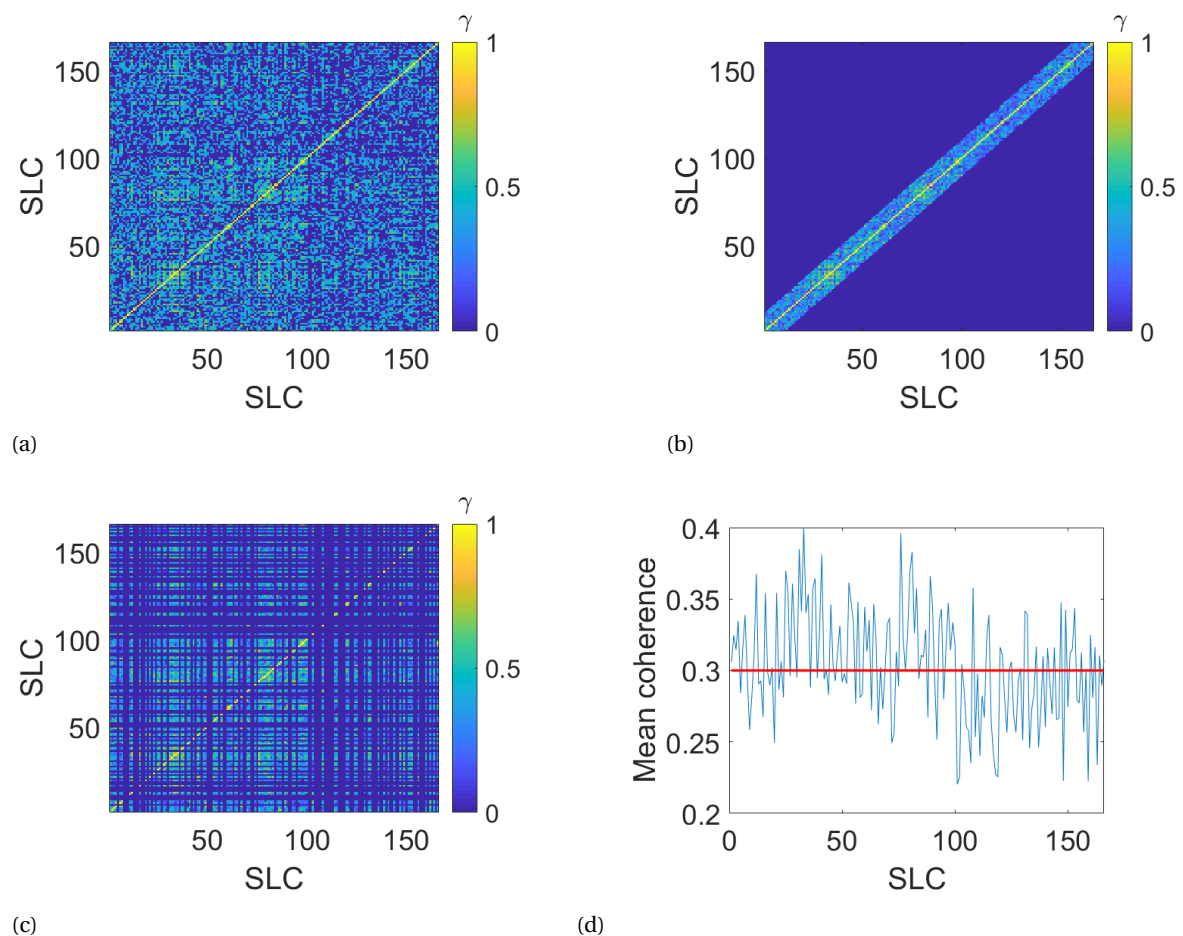


Figure 5.2: Different methods to extract coherent interferograms from coherence matrices. **(a)** Coherence threshold method: Coherence threshold = 0.3, **(b)** Diagonal method: Number of diagonals = 10, **(c)** Mean method: Threshold = 0.3 and **(d)** the mean of the coherence matrix with the red line indicating the threshold above which interferograms are taken into account for the estimation of relative deformation.

The Threshold method is chosen because it directly applies a threshold on the quality of the interferograms. In this way, only combinations of SLC's are used for which it is believed that they contain relevant interferometric phase information. For the Diagonal method, the reasoning is that by only selecting interferograms which have a short baseline, the magnitude of the temporal decorrelation is limited. In this way (in

contrast to the Threshold method), no interferograms are taken into account which have accidentally high coherence. The Mean method applies the most severe restriction, because the mean coherence for all interferograms formed with one SLC should be high enough. The benefit from this method is that only good quality SLC's are used. The three described approaches to select coherent interferograms will be used in Chapter 6 to estimate relative deformation.

5.2. Estimating relative deformation

In this section, equations are presented to estimate relative deformation of a pixel with respect to a nearby Point Scatterer. In Section 5.2.1 the observation equation is shown in which the observed phase differences are related to a relative deformation velocity and relative residual topography. This observation equation is solved using a Least-Squares method and a periodogram method, respectively. The two methods are then tested on PS pixels and the results are compared with a PSI calculation (Section 5.2.2). In Section 5.3, a method is proposed to evaluate and compare the methods with each other.

5.2.1. Observation equation

To increase the InSAR point density on the dike, the relative deformation with respect to a nearby PS is estimated. Results of a PSI analysis (in this thesis DePSI) are used to obtain deformation time series of PS's. Next, the deformation of pixels on the vegetated part of the dike is estimated by relating the deformation of this pixel to the closest PS pixel. Because of the short distance between the considered pixel and the PS, the assumption is that the atmosphere and orbit errors will cancel when looking at double differences. The relative phase between pixel X and the PS is formulated as

$$\phi_X^{12} - \phi_{PS}^{12} = W \{ \Delta\phi_D^{12} + \Delta\phi_T^{12} + \Delta\phi_A^{12} + \Delta\phi_O^{12} + \Delta\phi_N^{12} \}, \quad (5.1a)$$

with

$$\phi_X^{12} = W \{ \phi_X^1 - \phi_X^2 \} = W \{ \phi_{D,X}^{12} + \phi_{T,X}^{12} + \phi_{X,A}^{12} + \phi_{O,X}^{12} + \phi_{N,X}^{12} \}, \quad (5.1b)$$

and

$$\phi_{PS}^{12} = W \{ \phi_{PS}^1 - \phi_{PS}^2 \} = W \{ \phi_{D,PS}^{12} + \phi_{T,PS}^{12} + \phi_{A,PS}^{12} + \phi_{O,PS}^{12} + \phi_{N,PS}^{12} \}, \quad (5.1c)$$

in which Eq.(5.1c) is the observed phase at the location of the PS pixel as identified by DePSI and Eq.(5.1b) is the observed phase of another pixel X. The double phase difference between pixel X and the PS is formulated in Equation 5.1a, in which Δ indicates the spatial difference between point X and the PS. Next, we assume that the two terms $\Delta\phi_A^{12}$ and $\Delta\phi_O^{12}$ are negligible small due to the large correlation of these terms over short distances. Under this assumption, there are three terms left in Eq.(5.1a): relative deformation, relative residual topography and the relative noise. The deformation is modeled linearly according to Eq.(2.11) and the residual topography modeled according to Eq.(2.16). The observation equation then reads

$$\phi_X^{12} - \phi_{PS}^{12} = \frac{-4\pi}{\lambda} B_T \Delta V_{lin} - \frac{-4\pi}{\lambda} \frac{B_{\perp}}{R \sin(\theta_{inc})} \Delta H_{res}, \quad (5.2)$$

in which ΔV_{lin} is the relative linear deformation (mm/year) between point X and the nearest PS pixel and ΔH is the relative residual topographic component between point X and the nearest PS pixel. The model could easily be extended with other parameters such as temperature and excessive rainfall. Important to notice here is that the phase of the considered pixel X is multi-looked based on a spatial adaptive filter (SHP are found using the Kolmogorov-Smirnov test) to decrease the noise in Eq.(5.1a).

Least-squares

Under the assumption that there are no ambiguities over short distances, Eq.(5.2) can be solved by using the Least-Squares equation

$$y = Ax, \quad (5.3)$$

with y the observed double differences, A the design matrix and x the solution vector, formulated as

$$A = \begin{bmatrix} -\frac{4\pi}{\lambda} B_T^{14} & -\frac{4\pi}{\lambda} \frac{B_{\perp}^{14}}{R \sin(\theta_{inc})} \\ -\frac{4\pi}{\lambda} B_T^{36} & -\frac{4\pi}{\lambda} \frac{B_{\perp}^{36}}{R \sin(\theta_{inc})} \\ -\frac{4\pi}{\lambda} B_T^{25} & -\frac{4\pi}{\lambda} \frac{B_{\perp}^{25}}{R \sin(\theta_{inc})} \\ -\frac{4\pi}{\lambda} B_T^{45} & -\frac{4\pi}{\lambda} \frac{B_{\perp}^{47}}{R \sin(\theta_{inc})} \\ \vdots & \vdots \end{bmatrix}, \mathbf{x} = \begin{bmatrix} \Delta V_{lin} \\ \Delta H_{res} \end{bmatrix}, \mathbf{y} = \begin{bmatrix} \phi_X^{14} - \phi_{PS}^{14} \\ \phi_X^{36} - \phi_{PS}^{36} \\ \phi_X^{25} - \phi_{PS}^{25} \\ \phi_X^{47} - \phi_{PS}^{47} \\ \vdots \end{bmatrix}. \quad (5.4)$$

The observations can be weighted by using the variance matrix Q_{yy} , for which the variances are dependent on the magnitude of the coherence and on the number of SHP (see Section 3.2.3 for the estimation of interferometric standard deviation of the phase based on coherence and SHP). Using the variance matrix Q_{yy} , the solution \mathbf{x} can be calculated as

$$\mathbf{x} = (A^T Q_{yy} A)^{-1} (A^T Q_{yy} \mathbf{y}), \quad (5.5a)$$

with

$$Q_{yy} = \begin{bmatrix} \sigma_{\phi^{14}}^2 & 0 & 0 & 0 & \cdots \\ 0 & \sigma_{\phi^{36}}^2 & 0 & 0 & \cdots \\ 0 & 0 & \sigma_{\phi^{25}}^2 & 0 & \cdots \\ 0 & 0 & 0 & \sigma_{\phi^{47}}^2 & \cdots \\ \vdots & \vdots & \vdots & \vdots & \ddots \end{bmatrix}, \quad (5.5b)$$

where $\sigma_{\phi^{ij}}^2$ is the estimated variance of the interferometric phase (Eq. (3.27)) between acquisition i and j . Note that for completeness, also the covariances should be included in Q_{yy} . Due to the time-span of this thesis, this is not accounted for but should be considered in future research. The advantage of this method is that it is easy to add other parameters to the design matrix (such as temperature or excessive rainfall). The drawback is that this method is not able to solve ambiguities in the double differences.

Periodogram

When dealing with ambiguities in the double differences, an alternative approach is to estimate the parameters of interest using a periodogram function

$$\operatorname{argmin}_p (RMSE) = RMSE \left(\frac{1}{\sum K_{\sigma}} K_{\sigma} W \left\{ \phi_{X,PS}^{\text{obs}} - \phi_{X,PS}^{\text{model}}(p) \right\} \right), \quad (5.6)$$

where RMSE stands for the Root Mean Square Error, K_{σ} is the weight vector applied to the model for which the diagonal of Q_{yy} is used. $\phi_{X,PS}^{\text{obs}}$ are the observed phases of point X relative to the nearest PS point which have been selected based on an interferogram selection method. $\phi_{X,PS}^{\text{model}}$ are the estimated phases

$$\phi_{X,PS}^{\text{model}}(p) = \phi_{X,PS}^{\text{model}}(\Delta V_{lin}, \Delta H_{res}) = \frac{-4\pi}{\lambda} B_T \Delta V_{lin} - \frac{4\pi}{\lambda} \frac{B_{\perp}}{R \sin(\theta_{inc})} \Delta H_{res}, \quad (5.7)$$

Where B_T and B_{\perp} are the temporal and perpendicular baselines of the selected interferograms. To find the optimal solution with minimal RMSE, a range of combinations of the relative deformation velocity ΔV_{res} and relative residual topography ΔH_{res} is searched. In this research, the initial search space is chosen such that it spans a wide range of values for ΔV_{res} and ΔH_{res} with a coarse resolution. If the obtained solution is close to the edge of the search space, the center of the search space is placed around the obtained solution and Eq.(5.6) is evaluated again for the new search space. After a solution is found, the initial coarse resolution is refined and the periodogram is evaluated one more time to obtain the final solution. Note that in this formulation, the RMSE is minimized instead of the maximization of the temporal coherence which is often used (see for example van Leijen (2014)). The RMSE is used as minimization criterion to be able to compare the results of the Least-Squares method and periodogram method.

The advantage of this method is that it is able to deal with ambiguities in the phases. Downsides of this method are that the user has to specify the search space in which the optimal solution is to be found and the rapid increase of computational time if more parameters are added to the model.

In Figure 5.3, a flowchart is shown of the different steps and options which have been implemented using MATLAB. The algorithm uses as input SLC data which is processed by an InSAR processor (in this research, DORIS is used). The complex coherence is estimated using a spatial adaptive window for which the user can specify the statistical tests which is used for computing the SHP for each pixel. By computing the phase of the complex coherence, the multi-looked phase is obtained. The coherence matrix is constructed by using the absolute value of the complex coherence. From the coherence matrix, coherent interferograms are selected based on a threshold method. Three methods are implemented to find these coherent interferograms (Threshold method, Diagonal method and the Mean method). The relative phase is computed by finding the closest PS (as found by a PSI analysis) for each pixel. To estimate the relative deformation velocity as well as the relative residual topography, either the Least-Squares method or periodogram model is method. The results are visualized spatially on a map of the Marken island. Important are the maps with the estimated relative deformation velocity, relative residual topography, RMSE, amount of coherent interferograms and SHP.

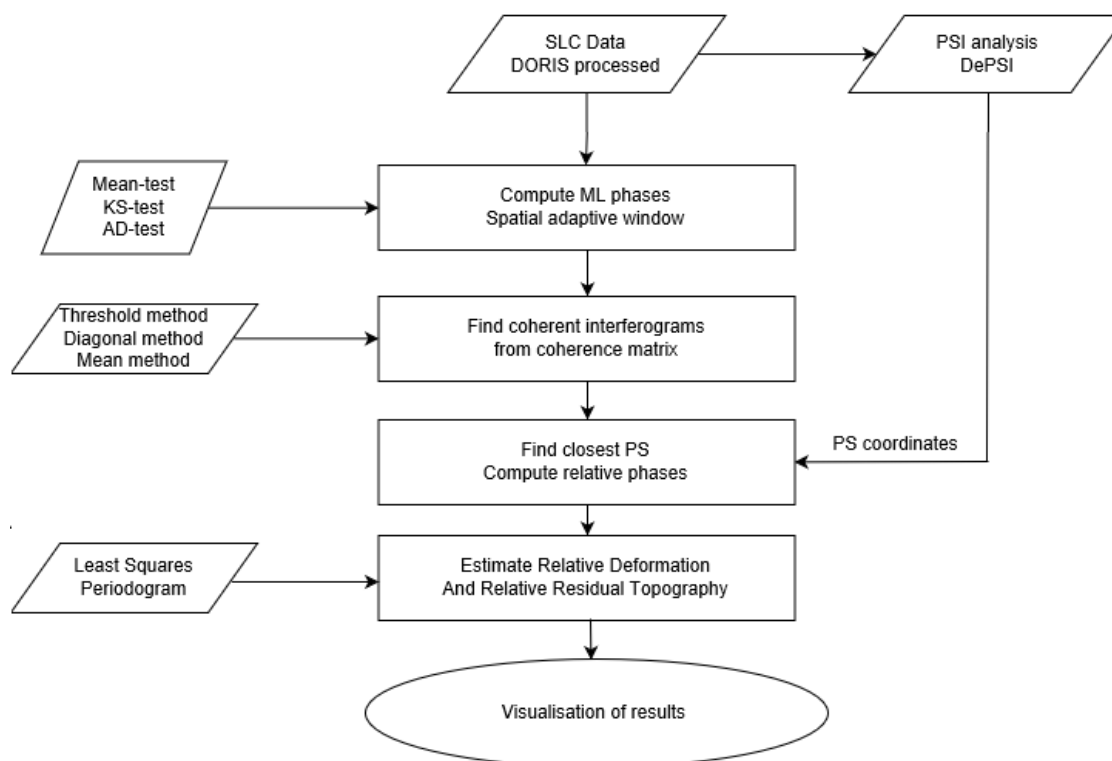


Figure 5.3: Flowchart of the implemented algorithm in Matlab. The input consists of SLC data which is processed by DORIS. In this research, the algorithm is used for TerraSAR-X data and Radarsat-2 data, but other sensors are also possible. The user can specify several options in the software. For multilooking, different statistical tests can be used to compute SHP. Different selection methods are implemented to find coherent interferograms based on the coherence matrix. Finally, the relative deformation is estimated either by using a Least-Squares method or a periodogram method.

As can be observed in Figure 5.3, there are three variables which can be changed (excluding the sensor type of the SLC data), leading to 18 possible combinations. In Section 5.3, a methodology is proposed to compare the different combinations. First, in the next section, the proposed Least-Squares method and periodogram method are tested on PS. The estimated relative deformation is then compared with results of a PSI analysis.

5.2.2. Testing the methods

To test whether the assumption that the terms $\phi_{X,PS}^A$ and $\phi_{X,PS}^O$ in Eq.(5.1) are negligible due to the large correlation over short distances, the Least-Squares method and periodogram function are tested on PS pixels. This means that for pixel X in Eq.(5.2) another PS pixel is chosen. In this way the relative deformation obtained by the two methods can be compared with the relative deformation which was found by DePSI. As a test case, the same crop of the Marken island is chosen as in Figure 4.2. In this crop each PS is chosen as reference pixel once, relative to which the deformation and residual topography is estimated for all other PS pixels in the crop (a total of 23 PS are evaluated). In Figure 5.4a and 5.4b the relative deformation of DePSI is plotted against the relative deformation as estimated by the Least-Squares method and periodogram method, respectively. Similarly, the relative residual topography is plotted for both methods in Figures 5.4c and 5.4d.

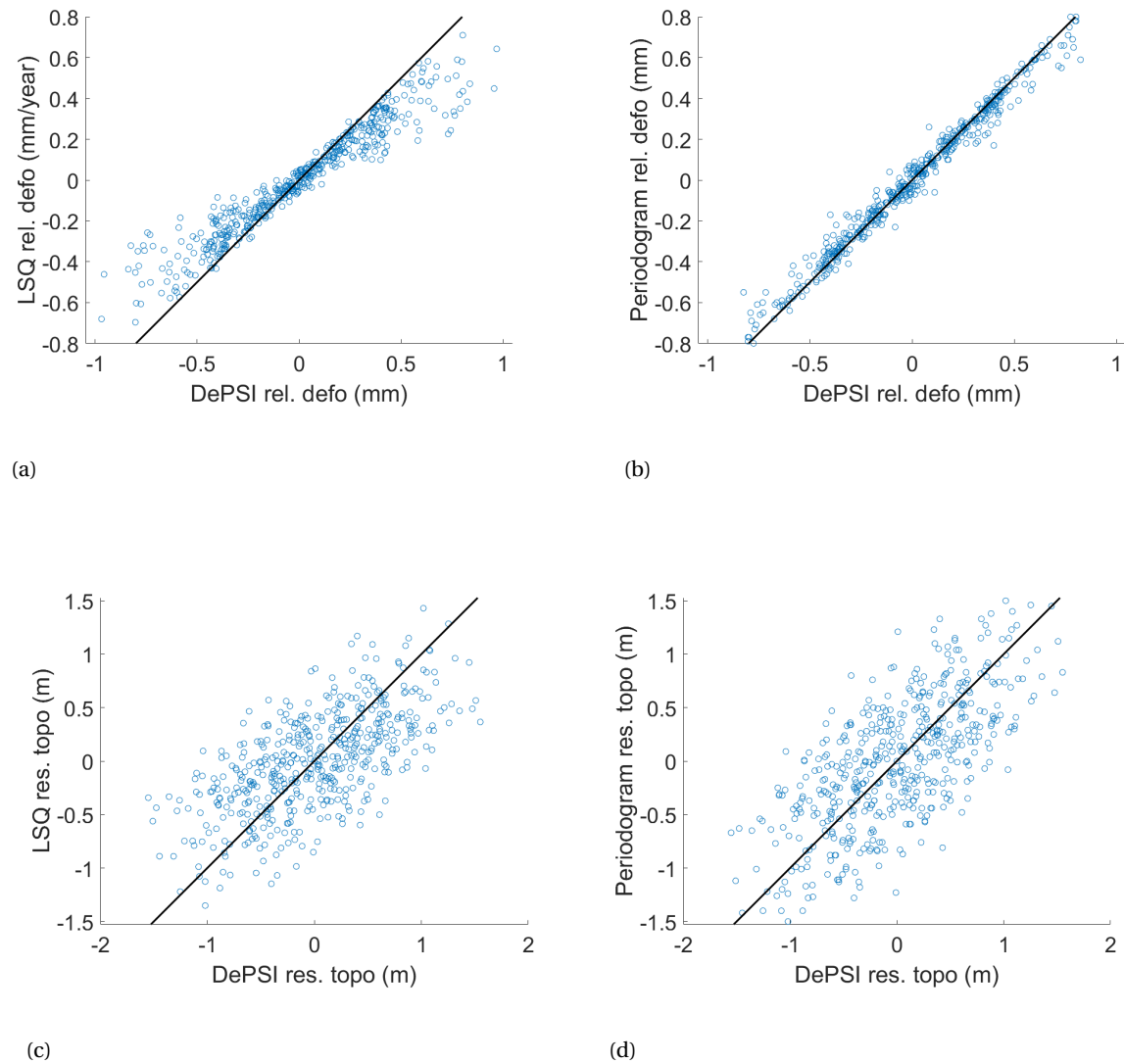


Figure 5.4: Scatterplots of relative deformation/residual topography estimated by DePSI on the x-axis versus periodogram/Least-Squares estimate on the y-axis. **(a)** Relative deformation DePSI vs Least-Squares, **(b)** Relative deformation DePSI vs periodogram, **(c)** Residual topography DePSI vs Least-Squares **(d)** Residual topography DePSI vs periodogram. 23 PS have been evaluated.

Figure 5.4a and 5.4b show that the estimated deformation by both methods are not far off the results of the PSI analysis. Comparing the Least-Squares method with the periodogram method, it can be observed that for the Least-Squares method the difference between estimated relative deformation and DePSI becomes larger as compared to the periodogram method. A hypothesis is that for these estimates, there are ambiguities in the data which are captured by the periodogram method but not by the Least-Squares method. The spread in the estimation of the relative residual topography is somewhat larger but still there is a significant correlation between both models. These results give confidence that the assumptions made in Section 5.2.1 are valid.

5.3. Method evaluation

To evaluate the performance of the methods, the RMSE of the Least-Squares method and periodogram method are compared with each other. For the periodogram method, the RMSE is already computed by the periodogram function (Eq. (5.7)). For the Least-Squares method, it can be computed as the RMSE of the difference between observed phases and estimated phases $\text{RMSE}(y - \hat{A}\hat{x})$. For both the Least-Squares method and the periodogram method, a histogram of the computed RMSE values is depicted in Figure 5.5.

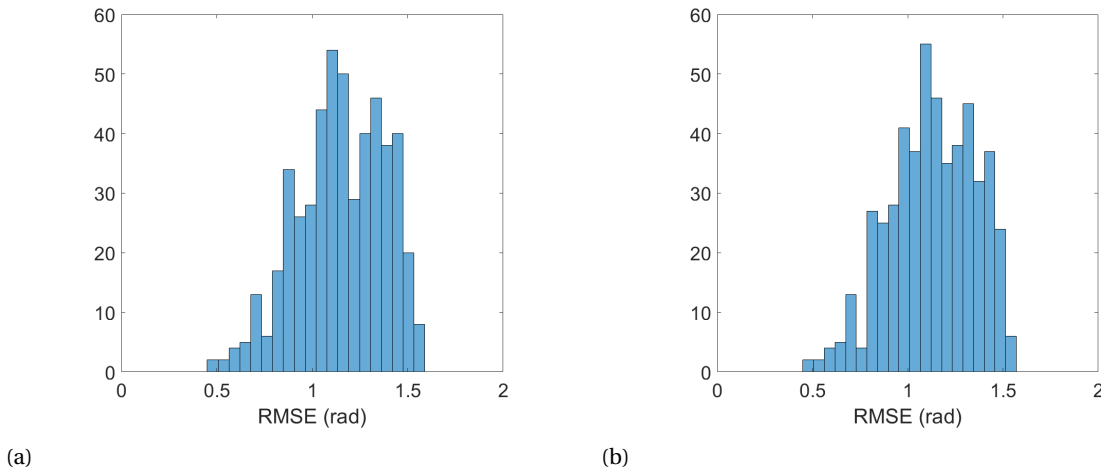


Figure 5.5: Histograms of the RMSE for the estimation of relative deformation and relative residual topography between PS. **(a)** Least-Squares method and **(b)** Periodogram method.

To compare the different methods with each other, the amount of pixels is counted which have a RMSE value below a certain threshold for which it is believed that it still contains information. This threshold is based on the accuracy of the estimated deformation time series by DePSI. A quality measure for the deformation series as obtained by DePSI is the Spatial Temporal Consistency (STC), first introduced by Hanssen and van Leijen (2008a). The STC is defined as

$$\eta_i = \min_{\forall j} \frac{\lambda}{4\pi} \sqrt{\frac{1}{1-S} \sum_{s=1}^{S-1} \left((\phi_j^{0s} - \phi_i^{0s} - (\phi_j^{0s+1} - \phi_i^{0s+1})) \right)^2}, \quad (5.8)$$

where η_i represents the STC for PS and is defined as the minimum RMSE of the double differences between PS i and surrounding PS j .

0 represents the master image, s the slave image and S is the amount of slave images. \forall is the operator that indicates that all pixels j are selected which are close to the considered pixel i . The surrounding PS j are selected within a maximum radius but must also be outside the area specified with the minimum radius to reduce the change of selecting an undetected sub-main lobe (van Leijen, 2014). For the PSI analysis as described in Section 4.1.1 the STC is calculated according to formula 5.8, using a minimum radius of 20 m and a

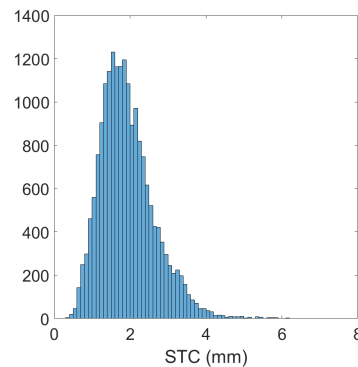


Figure 5.6: Spatial Temporal Consistency for PS on the Marken Island (see Figure 4.2a). The PS are found by using 166 acquisitions between February 2009 until February 2016 in a PSI analysis.

maximum radius of 50 m. The STC is calculated for all PS in the area of interest (see Figure 4.2a), of which a histogram is shown in Figure 5.6. Most of the PS have a STC of 2 mm or less and have a corresponding coherence of 0.6 (applied threshold in DePSI) or higher. In this research, the aim is to obtain deformation time series of pixels which have a lower coherence. The expected accuracy of the obtained deformation time series for pixels with a low coherence value is lower as compared to pixels which have high coherence. As a threshold for the STC for which it is still expected that the considered pixel contains information, 3 mm is applied. For TerraSAR-X, this minimum RMSE of 3 mm is equivalent to a RMSE of 1.25 rad.

Besides the threshold on the RMSE, another threshold is set on the minimum amount of selected interferograms. If, for example, based on the interferogram selection method only four coherent interferograms are selected in the algorithm, the RMSE of the (linear) fit is relatively low because only a few measurements are taken into account. This would result in many pixels having a low RMSE while, if more interferograms were used, the RMSE would be much higher. Therefore, a threshold is applied on the minimum amount of interferograms which have to be used in the algorithm. This threshold should be high enough such that no pixels are used for which the RMSE is underestimated and should be low enough such that no significant estimations are thrown away. To determine the optimal threshold, a numerical experiment is performed as follows. A vector of N phases is simulated which is randomly distributed between $-\pi$ and π . Temporal baselines are simulated and also are randomly distributed on the interval $[0,5]$ years. The deformation (which should be zero) is then estimated with the periodogram method which only takes deformation into account

$$\phi_{\text{model}}(V_{lin}) = \frac{-4\pi}{\lambda} B_T V_{lin}, \quad (5.9)$$

where B_T is the simulated temporal baseline, V_{lin} the linear deformation velocity and λ the wavelength for which 0.031m (X-band) is used.

In Figure 5.7 the result of the experiment is shown. On the x-axis, the amount of measurements (i.e. coherent interferograms) is increased from 1 to 200. On the y-axis, the RMSE is plotted for each estimated linear deformation on the simulated data. The blue points represents the RMSE in radians according to Eq.(5.6) as function of the amount of measurements. To decrease the variability, for each point in the graph the simulation is repeated 200 times of which the mean RMSE is shown on the y-axis. For only one measurement, the RMSE is equal to zero because there is always a perfect linear fit between two data points. The RMSE then quickly increases until approximately 20 measurements after which it steadily increases up to about 100 measurements. As the number of measurements increases the RMSE of the estimation approaches 1.81 radians, which is the standard deviation of the randomly distributed phases between $-\pi$ and π . To determine the optimal threshold, the derivative of the blue curve is plotted in black. At around 60 measurements, the curve stabilizes and therefore this number is chosen as the optimal threshold.

Next, the threshold on RMSE of 1.25 radians and the threshold of 60 on the minimum amount of coherent interferograms is applied on the histogram of the two methods in Figure 5.5a and 5.5b. For the Least-Squares method, 337 estimates have a RMSE of 1.25 radians and a minimum of 60 selected coherent interferograms or lower compared to 357 estimates for the periodogram method (a total of 529 estimates have been made). Apparently there are still some ambiguities in the phase differences between the PS, because otherwise the Least-Squares method would have obtained a better fit compared to the periodogram method.

In the next chapter, the deformation estimation methods as described in this chapter are tested on the case study, using the different methods to select coherent interferograms from the coherence matrix.

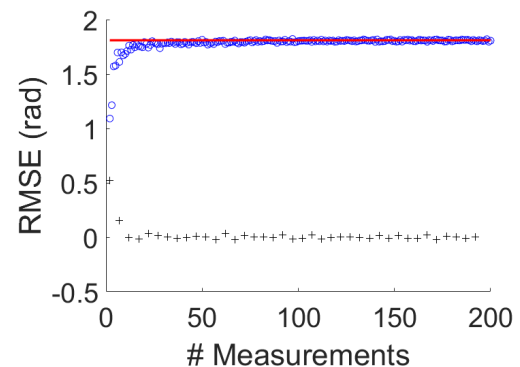


Figure 5.7: Root Mean Square Error for a linear fit on randomly distributed phases between $-\pi$ and π using the periodogram method. On the x-axis the amount of randomly distributed phases is increased from 1 to 200. On the y-axis the RMSE is depicted of the linear fit. In blue, the estimated RMSE according to Eq.(5.6) is shown. In black, the derivative of the blue curve is plotted. The red line represents the standard deviation of a uniform distributed variable between $-\pi$ and π .

6

Results

In this chapter, results of the proposed methods are visualized and interpreted. First, in Section 6.1, results of a PSI and DSI analysis are compared with each other. Next, in Section 6.2, several statistical tests are compared with each other to eventually choose the best statistical test to select Statistical Homogenous Pixels. In Section 6.3, TerraSAR-X data is used to estimate relative deformation. Here the periodogram and Least-Squares methods are compared with each other as well as the different coherent interferogram selection methods. Section 6.4 applies the developed methodologies on the Radarsat-2 stack and Section 6.5 discusses the results.

6.1. State of the art

The goal of this thesis is to be able to estimate deformation time-series on the vegetated part of a dike. Using a PSI analysis, as was shown in Section 4.1.1, it is possible to estimate deformation on a dike but so far only PS on a hard surface have been found. In this section, a DSI analysis is used to investigate whether the InSAR point density on the dike can be improved. For the PSI analysis, DePSI is used (as in Section 4.1.1). For the DSI analysis, the software DS Delft is used as developed by Samiei-Esfahany (2017). The SHP which are used for complex multilooking are obtained based on the KS-test. The phase inconsistency, introduced by complex multilooking, is solved based on a Maximum Likelihood estimator to obtain an Equivalent Single Master stack. The complex values in the original SLC's are replaced with the ESM corrected phases if, for a pixel, 25 or more SHP are found. In this way, the phase of the PS is preserved since (in general) no more than 25 SHP are obtained for a PS (see also Section 3.2 for more information about DSI). The interferograms (with corrected phases for DS) are then processed by DePSI to estimate deformation time-series.

In Figure 6.1, the results of DePSI and DS Delft are compared with each other on a background of the amplitude dispersion. Using the DePSI software, 22 PS are found (black dots), which are mainly situated on the crest and outer slope of the dike (one PS is found on the rubble). After the DS Delft software was applied to reduce the noise of the DS, 10 extra points with a temporal coherence (see Eq.(3.2)) lower than the threshold (threshold is set on 0.5) are obtained. Most of the DS are (like the PS) situated on the crest and outer slope of the dike and a few have been detected on the rubble. No DS have been found on the vegetated part of the dike. This analysis will be used to compare the results obtained by the developed methodology in Chapter 5 with the state of the art.

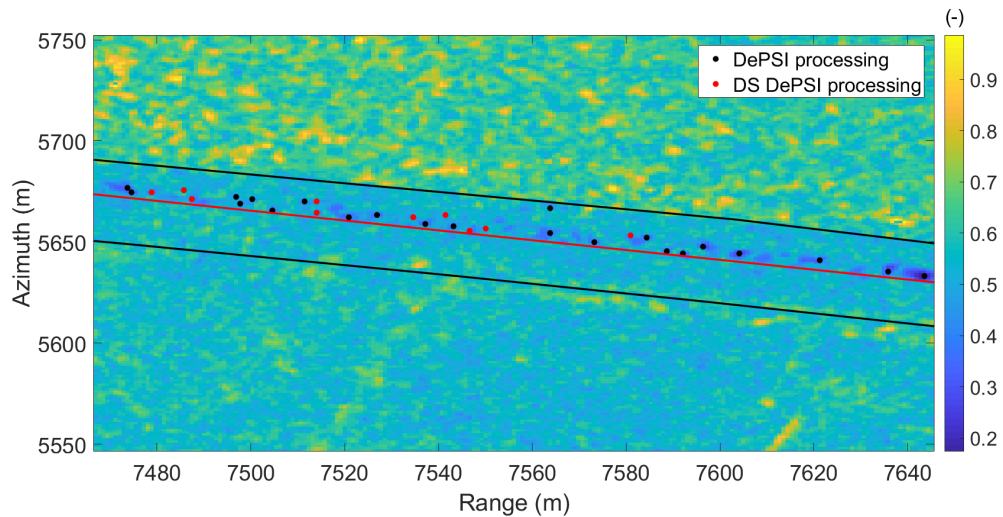


Figure 6.1: Comparison of PSI analysis (using DePSI) and DSI analysis (DS Delft). The black dots indicate the PS which have been found using a PSI analysis. The red dots indicate the pixels that have been found by using a DSI analysis (DS Delft) in which the phases have been multi-looked and on which an ESM step is performed. Using the PSI analysis, 22 PS were found. The DS Delft software was able to find 10 extra DS. the red line represents the intersection between the revetment and grass cover, the black dots the PS, the red dots the DS and the black lines indicate the water boundaries.

6.2. Statistical Homogeneous Pixel selection

As described in Section 3.2.1, statistical tests can be used to find Statistical Homogeneous Pixels (SHP) which show similar amplitude behavior in time. The SHP can then be used to apply a spatial adaptive multilooking step to reduce the phase noise ϕ_N that is present in the data. In this section three statistical tests (Mean-test, Kolmogorov-Smirnov- and Anderson-Darling test) are used on the case study to investigate the amplitude behavior of the pixels. The mean-test uses the difference in mean amplitude between two pixels and compares this value to a threshold. The Kolmogorov-Smirnov (KS) test computes the Empirical Cumulative Distribution Function (ECDF) of two pixels and compares the minimum distance between this functions (the supremum) to the test statistic. Anderson and Darling developed an extension to the KS-test, the Anderson-Darling (AD) test, which places more emphasis on the tail of the distribution (see Section 3.2.1 for more information on these statistical tests). For each pixel, the three tests have been used to find SHP in a 9x9 square window. The results of the three different tests, applied on the case study, are visualized in Figure 6.3 and the corresponding aerial image is depicted in Figure 6.2.



Figure 6.2: Aerial photo of the selected crop (Google Earth). The letters indicate different surface types for which the amount of SHP will be analyzed. A indicates an area on the water surface, B indicates an area on the grassland, C is placed in an urban area and D is placed on the dike itself. The red box approximates the coordinates of the processed cropped radar image.

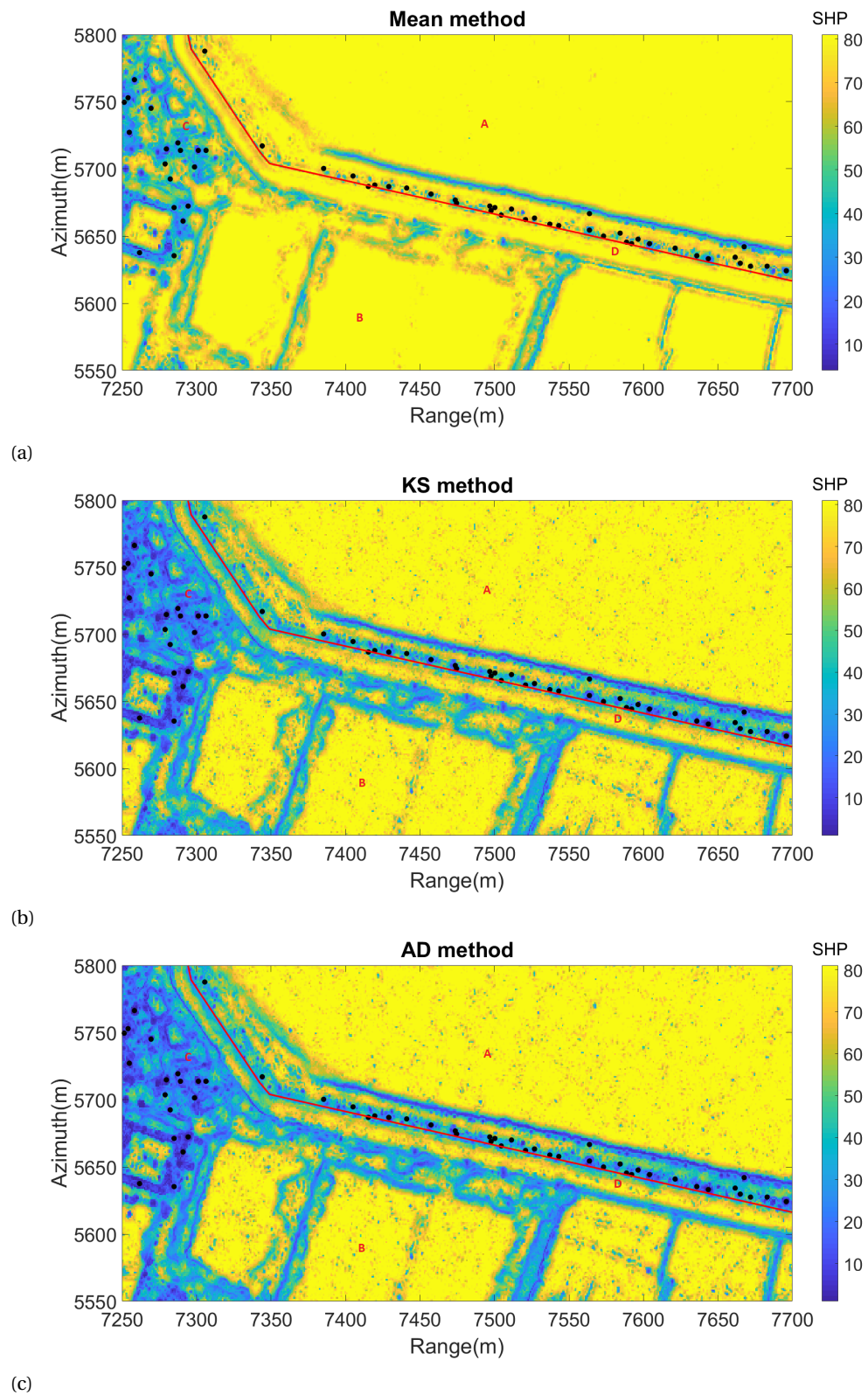


Figure 6.3: Comparison of different SHP selection tests. (a) Mean test, (b) Kolmogorov-Smirnov test, (c) Anderson-Darling test. For each pixel, a square 9x9 window is used to find the SHP for the reference pixel. The colorbar indicates the amount of SHP found for each pixel. the red line represents the intersection between the revetment and grass cover and the black dots indicate the PS as obtained by DePSI.

In the aerial image (Figure 6.2) as well as in the plots of the amount of SHP computed by different statistical tests (Figure 6.3), four letters are placed which indicate different surfaces. For the pixels on the water surface (A), in general 81 SHP are identified (note that the reference pixel is included, so actually 80 SHP are found). This is because the amplitude behavior of pixels on water is similar (although there are differences in amplitude between acquisitions), and therefore the ECDF's of the pixels do not differ more than the threshold. Pixels on the grassland (B) also obtain many SHP (similar to the pixels on water). For a square window of 9 by 9 (about $10 \times 10 \text{m}^2$) the amplitude behavior is about the same, and therefore most often 81 SHP are selected for pixels in grassland. A different behavior can be seen for pixels in the area of (C), which is placed in an area with buildings. Many objects are present in this urban area each with their own scattering behavior. One pixel can be on the roof of a building while the other pixel is on the street, leading to a different amplitude behavior over time. This is the reason why (in general) for a pixel in (C) only a few SHP are found by the statistical tests. On the dike itself (D), the different elements on the dike can be distinguished based on the amount of SHP. Close to the water surface, around 10-20 SHP are identified. In Figure 4.4a it can be seen that these pixels close to the water are situated on the stones which are placed as rubble. These stones are quite small and are randomly placed on and next to each other, leading to differences in reflections and thus a low number of SHP. In between these stones and the top of the dike, there is a relatively smooth surface with relatively many SHP. On the top of the dike, where most PS are found (red circles in Figure 6.3), a small road is situated of a few meters in width (see Figure 4.3). Because the window for finding the SHP is larger than this road, ECDF's of different surfaces are compared with each other, leading to small number of SHP. The inland part of the dike has a smooth surface and is covered with grass, again leading to a large number of SHP.

The computational times of the three different tests differ a lot, as is shown in Table 6.1. The Mean test appears to be the fastest test with a CPU time of 32 minutes. The KS-test is three times as slow as the Mean-test with 107 minutes. The computational time of the AD-test is significantly higher as compared to the KS-test with 2048 minutes. The main reason for the larger CPU time of the AD-test is that it uses the specific distributions to calculate the critical values. This leads to better sensitivity compared to the KS-test but also significantly increases the computation time. In contrast, the KS-test is distribution free in the sense that the critical values do not depend on the distribution. As described in Section 3.2.1, the AD-test is an extended version of the KS-test and was found to be the most powerful test for SAR data (Parizzi and Brcic, 2011). However, in Figure 6.3 it can be seen that the results of the KS-test and AD-test are very similar. In Figure 6.4 the differences between the KS-test and AD-test are shown. While the AD-test has proven to be the most powerful test to compare distributions of amplitude SAR data, in this thesis the KS-test is used. The reason for this is the considerable lower computation time of the KS-test compared to the AD-test while still obtaining similar results.

Type of test	CPU time (minutes)
Mean test	32
Kolmogorov-Smirnov test	107
Anderson-Darling test	2048

Table 6.1: Computation times for the computation of SHP using different statistical tests.

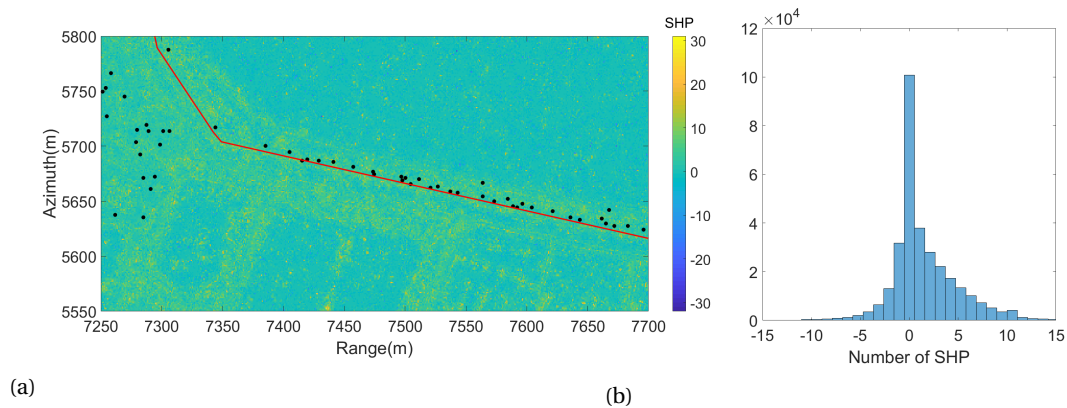


Figure 6.4: Comparison of the Kolmogorov-Smirnov test and Anderson-Darling test. (a) Difference between KS-test and AD-test in selected SHP (b) Histogram of the differences in amount of SHP between the KS-test and AD-test. the red line represents the intersection between the revetment and grass cover and the black dots indicate the PS as obtained by DePSI.

6.3. Application on TerraSAR-X data

In this section, the methods as proposed in Section 5.2 are used to estimate relative deformation. First, the results obtained with the periodogram method are shown and analyzed. Then, the periodogram method is compared with the Least-Squares method and the different methods for coherent interferogram selection are investigated. For the estimation, 166 acquisitions are used from the TerraSAR-X satellite, operating in StripMap mode. The SHP are estimated based on the KS test, which are then used to perform complex multilooking. For the periodogram method, according to Eq.(5.6), the (initial) boundaries for the estimation are set to -5 mm/year up to 5 mm/year for the relative deformation velocity and -2 m to 2 m for the residual topography. Note that for the relative deformation velocity, the implementation allows for an expansion of the boundaries if the obtained solution is close the boundary of the search space. This expansion of the boundaries is not implemented for the residual topography, since it turned out that the method is not very sensitive to this parameter.

The results which have been obtained by the periodogram method are presented in Figure 6.5. Figure 6.5a depicts the estimated relative deformation with respect to the closest PS. The closest PS are found by creating a Voronoi diagram. In Figure 6.5b the amount of SHP for each pixel is visualized which are estimated based on the KS test. Figure 6.5c is a map of the RMSE as estimated by the periodogram method and Figure 6.5d is a plot of the amount of selected interferograms which have a coherence of 0.4 or higher. The RMSE is relatively low for points nearby a PS which means that the proposed deformation model fits good to the data. As the distance to the PS increases, the RMSE increases quickly. There is a strip in the middle of the dike (surrounding the PS points) with relatively low RMSE. This strip corresponds to the small road which is situated on the crest of the dike (see Figure 4.3). Outside this strip, the RMSE quickly increases which indicates that the assumed deformation model does not fit to the data. The maximal RMSE is equal to 1.81 radians which is equal to the standard deviation of a uniform distributed random variable between $-\pi$ and π .

To further analyze the results, the letters A (water), B (intersection outer part of the dike and water, i.e. rubble), C (small stroke of grass between rubble and outer slope of the dike), D (crest and outer slope of the dike) and E (vegetated part of the dike) are placed in the figures to distinguish the different parts of the dike. Point (A) is located on the water surface and has a RMSE of (on average) 1.81 radians. This is to be expected because there is no coherent information in interferograms on water and therefore the RMSE approaches the standard deviation of a uniform distributed random variable between $-\pi$ and π . The estimated relative deformation velocity is noisy, having jumps from -6 mm/year to 6 mm/year. However, there is some correlation between neighboring points because of oversampling and pixel posting (see Section 4.3) as well as multilooking. Point (B) is situated on the intersection of the water and the outer part of the dike (see Figure 4.4a) at which rubble is situated. The number of SHP is relatively low and the amount of selected coherent interferograms is relatively high. On this part of the dike, one PS is selected. The RMSE on this part of the dike is still relatively high but already somewhat lower than 1.81. The estimated relative deformation velocities are less noisy as compared to the water area. (C) represents the area which is covered with grass (see Figure 4.4a). Most of the pixels have a large number of SHP, indicating distributed scattering behavior. The RMSE on this part of the dike decreases as the distance to the PS becomes less. (D) is situated on the crest and outer slope of the dike (Figure 4.3), on which most of the PS are situated. The RMSE close to the PS is often below 1 and many coherent interferograms are selected. Here it has to be noted that pixels close to the PS are not independent measurements with respect to the PS. Oversampling, pixel posting and side-lobes of the PS lead to a similar phase evolution as the PS. Since relative phases are used for the estimation this will lead to phases close to zero for which zero deformation is estimated with close to zero RMSE. Lastly, (E) is situated on the inner part of the dike which is covered with grass (see Figure 4.4b). Both the RMSE and the estimated relative deformation velocity exhibit similar behavior as compared to pixels on the water area (A).

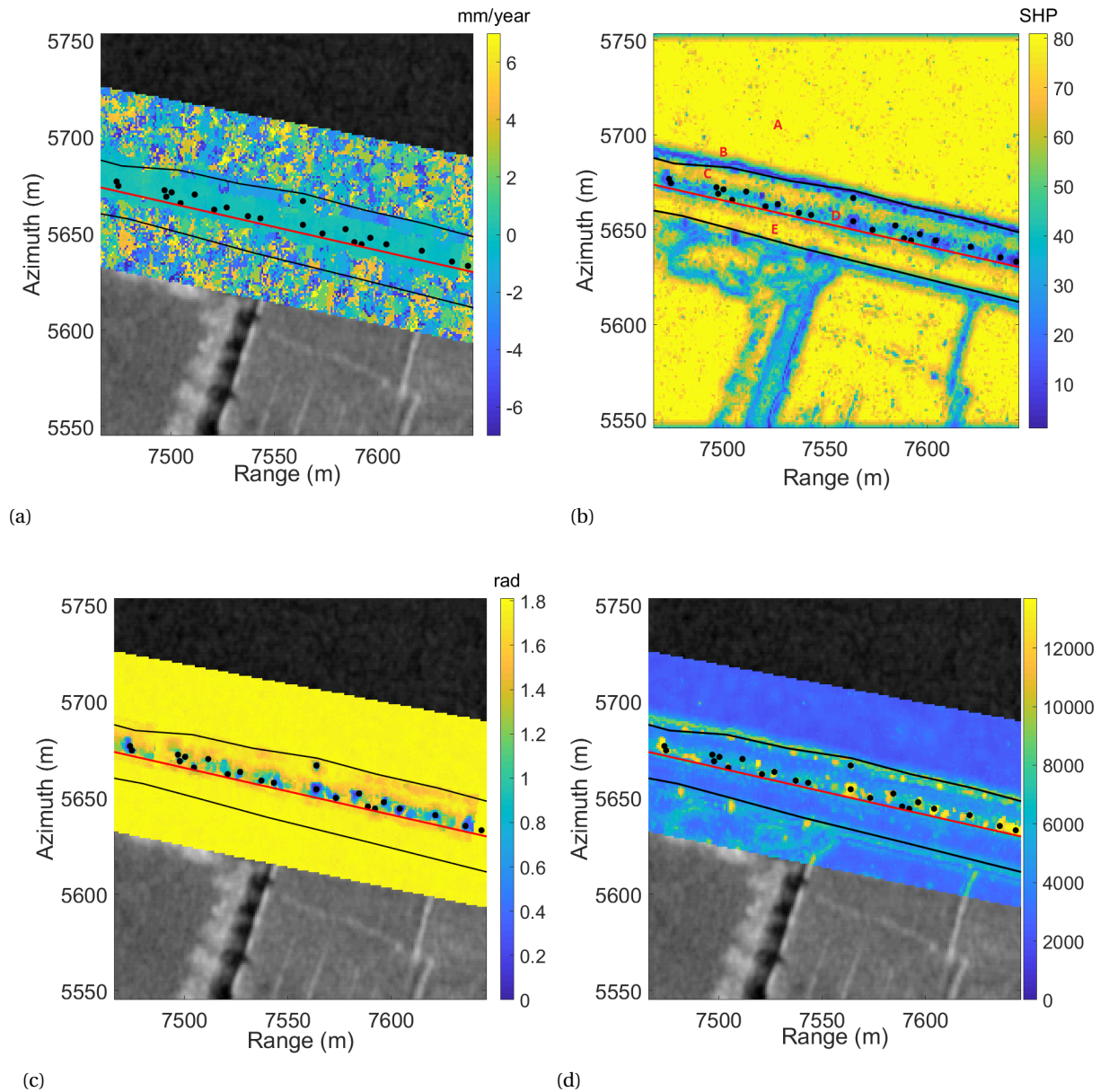


Figure 6.5: Results of relative deformation estimation (with respect to the closest PS) using the periodogram estimator. Only interferograms are taken into account which have a coherence of 0.4 or higher. **(a)** Estimated relative deformation using the periodogram method, **(b)** Amount of selected SHP using the Kolmogorov-Smirnov test with a square window of 9x9. **(c)** The RMSE of the relative deformation estimation. **(d)** Amount of coherent interferograms which have a coherence higher than 0.4. the red line represents the intersection between the revetment and grass cover and the black dots the PS. The black lines indicate the water boundaries of the outer part of the dike (lake) and the inner part of the dike (small ditch). These lines have been obtained by looking at the amplitude dispersion of the crop.

6.3.1. Periodogram VS Least-Squares

A similar analysis as for the periodogram method has been applied on the Least-Squares estimator. The results are compared with each other based on the proposed validation method in Section 5.3. For each pixel, the relative deformation model is estimated for the Least-Squares method (according to Eq.(5.5a)) and the periodogram method (according to Eq.(5.6)). The coherent interferograms are selected by using the threshold method (see Section 5.1) with a coherence threshold of 0.4. In Figure 6.6c and 6.6d, the RMSE is plotted for the periodogram and Least-Squares method, respectively. For the estimated relative deformation (periodogram method in Figure 6.6a and Least-Squares method in Figure 6.6b), only pixels are shown for which the RMSE is smaller or equal than 1.25. Pixels which have a RMSE lower than this threshold are assumed to contain information. Pixels with a RMSE larger than this threshold are considered too noisy.

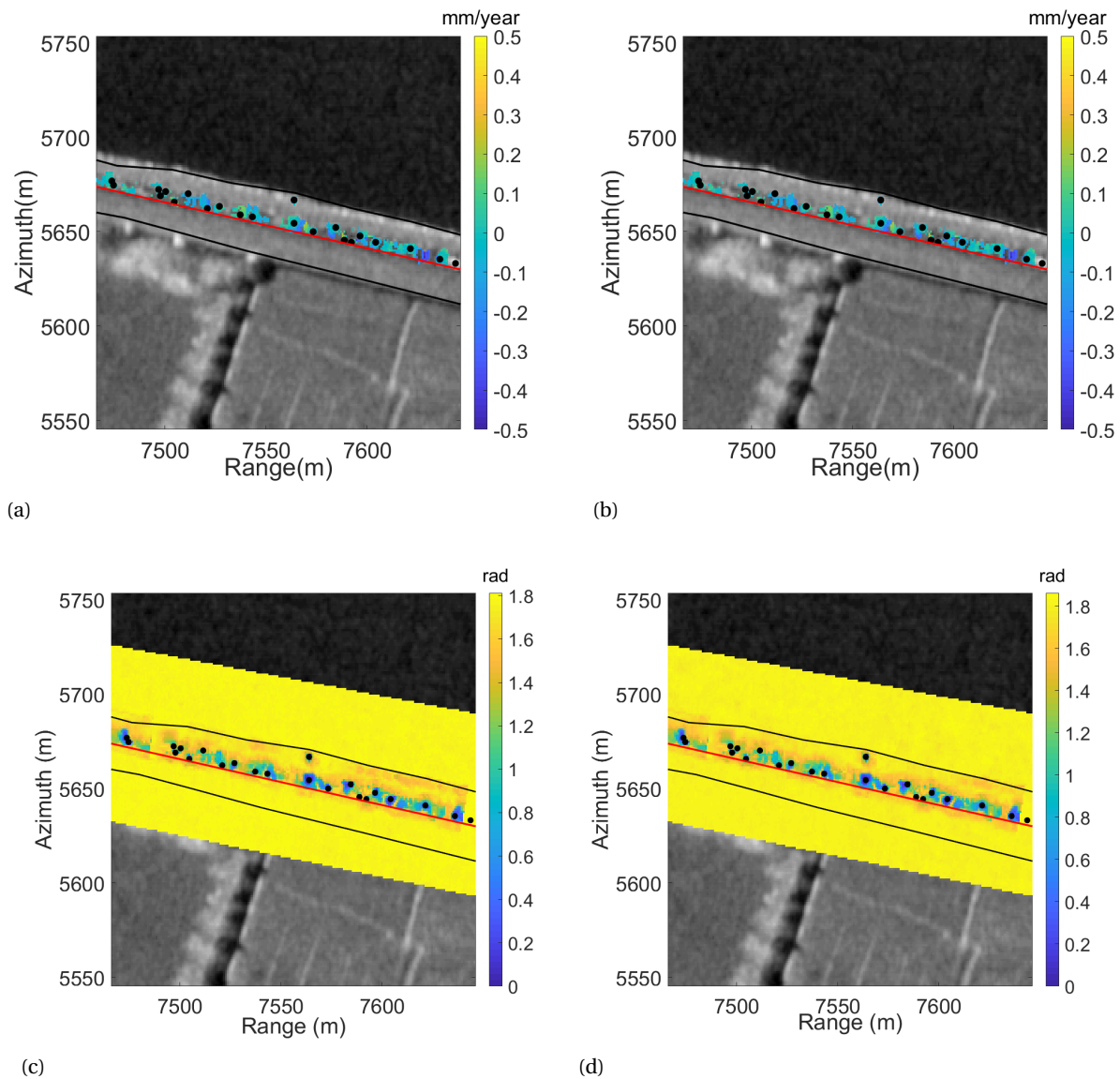


Figure 6.6: Comparison of results for the periodogram method with Least-Squares method. Only interferograms with a coherence higher than 0.4 are used in the estimation (threshold method). **(a)** Estimated deformation relative to the closest PS point using the periodogram method: only pixels are shown which have $RMSE \leq 1.25$, **(b)** Estimated relative deformation to closest PS point using the Least-squares method: only pixels are shown which have $RMSE \leq 1.25$. In **(c)** and **(d)**, the RMSE maps of the periodogram method and Least-Squares method are visualized, respectively. The estimated relative deformation of the periodogram method and Least-Squares method look quite similar. the red line represents the intersection between the revetment and grass cover, the black dots the PS and the black lines indicate the water boundaries.

Both RMSE maps look rather similar, the only difference being that the periodogram has some points close to the water with a lower RMSE as compared to the Least-Squares method. The relative deformation maps of the periodogram and Least-Squares method also look quite similar, indicating that phase ambiguities might not play a significant role. The differences in the relative deformation estimation are visualized in Figure 6.7a of which a histogram is made in 6.7b. The differences between both methods are relatively low and seem to be normally distributed.

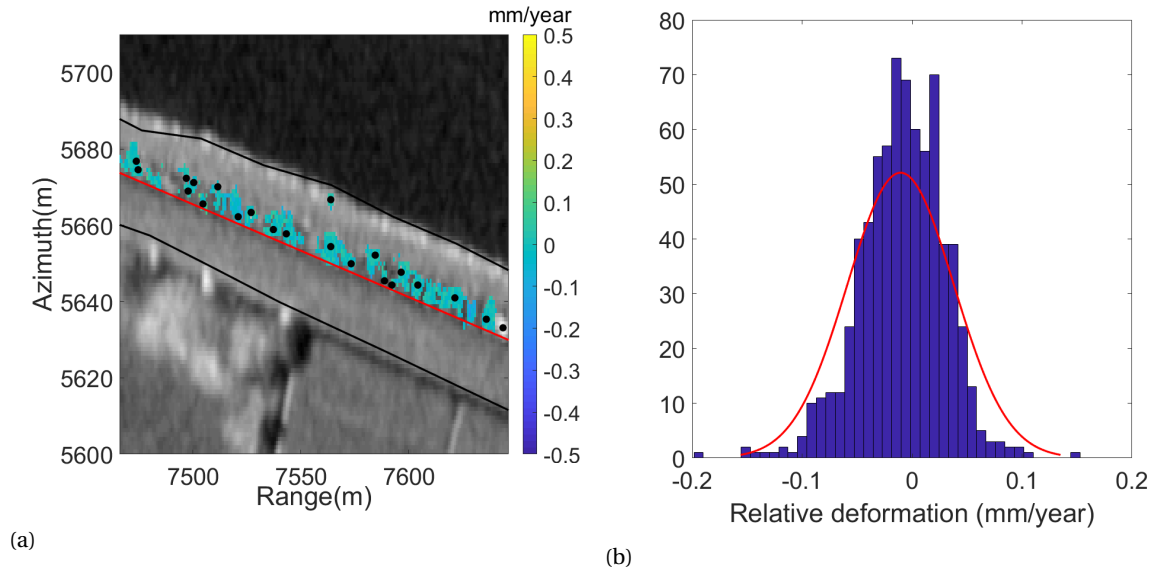


Figure 6.7: Differences of the relative deformation estimation between the periodogram (Figure 6.6a) and Least-Squares method (Figure 6.6b). **(a)** Differences of the estimated relative deformation velocity between the periodogram and Least-Squares method. the red line represents the intersection between the revetment and grass cover, the black dots the PS and the black lines indicate the water boundaries. **(b)** Histogram of the differences in estimated relative deformation between the periodogram and Least-Squares method.

It is interesting to see why for pixels close to a PS the RMSE is low, while for points further away from a PS (on the vegetated part of the dike) the RMSE is higher. In Figure 6.8 the different estimations for the periodogram and Least-Squares method are visualized for a point on the grass side of the dike.

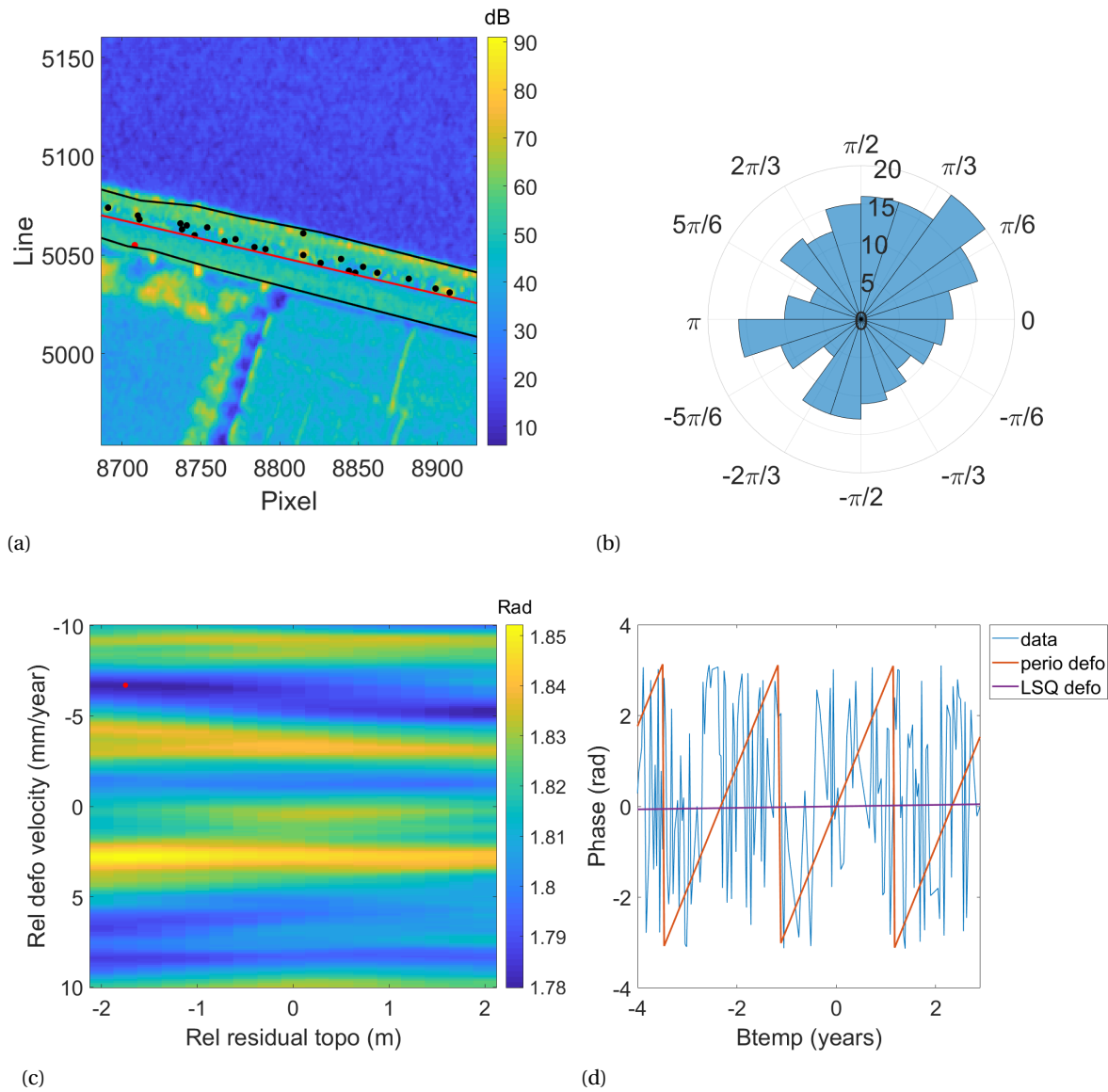


Figure 6.8: Visualization of estimated relative deformation for a point on the grass side of the dike. **(a)** Pixel for which the estimated relative deformation is visualized (in red). the red line represents the intersection between the revetment and grass cover, the black dots the PS and the black lines indicate the water boundaries. **(b)** Polar histogram of the relative (coherence based selected) interferometric phases. **(c)** Search space of periodogram method: The RMSE is for each combination of relative deformation and relative residual topography is plotted. **(d)** Single master phases (master image is 12 March 2013) versus the estimated (wrapped) relative deformation phases of the periodogram and Least-Squares method.

A polar histogram for a point on the vegetated part of the dike is depicted in Figure 6.8b and shows that the phases with respect to the closest PS point are more or less randomly distributed between $-\pi$ and π . In Figure 6.8c, the search space of the periodogram is visualized for a point on the grass side of the dike. For each combination of residual topographic height and relative deformation velocity, the RMSE is estimated according to Eq.(5.6). First, it is observed that the RMSE values of the different estimations has a minimum at 1.78 radians which can be considered as noise. The periodogram method (for TerraSAR-X data) is more sensitive to (relative) deformation as compared to (relative) residual topography. Increasing or decreasing the residual topographic height will not lead to much difference in the RMSE, while increasing or decreasing the relative deformation velocity results in a larger change in RMSE. Furthermore, for the considered point on the grass side of the dike, there are multiple minimums in the search space of the periodogram. For example, in Figure 6.8c, the solution with a relative deformation of 9 mm/year and a relative residual topography of -2m has a RMSE of 1.79 radians which is only a little higher as compared to the obtained solution (RMSE=1.78

radians) but the solutions differ a lot. This implies that the obtained solution has no physical meaning.

The estimated phase time series of the periodogram and Least-Squares method are based on the selected coherent interferograms. However, it is difficult to compare and interpret these results as there is no common master image. Therefore the phase time series are converted to a single master (12 March 2013) configuration in Figure 6.9d to be able to better visually interpret the results.

It can visually be seen that both methods do not fit well to the data. As described in Section 5.2.1 and 5.2.1, the difference between the Least-Squares and periodogram method is that the periodogram method accounts for ambiguities in the relative phases. The periodogram method tries to add ambiguities to the deformation model while the Least-Squares method finds a minimum RMSE for zero relative deformation.

For a pixel which is relatively close to a PS, the solutions of the Least-Squares and periodogram method do not differ that much, as is depicted in Figure 6.9.

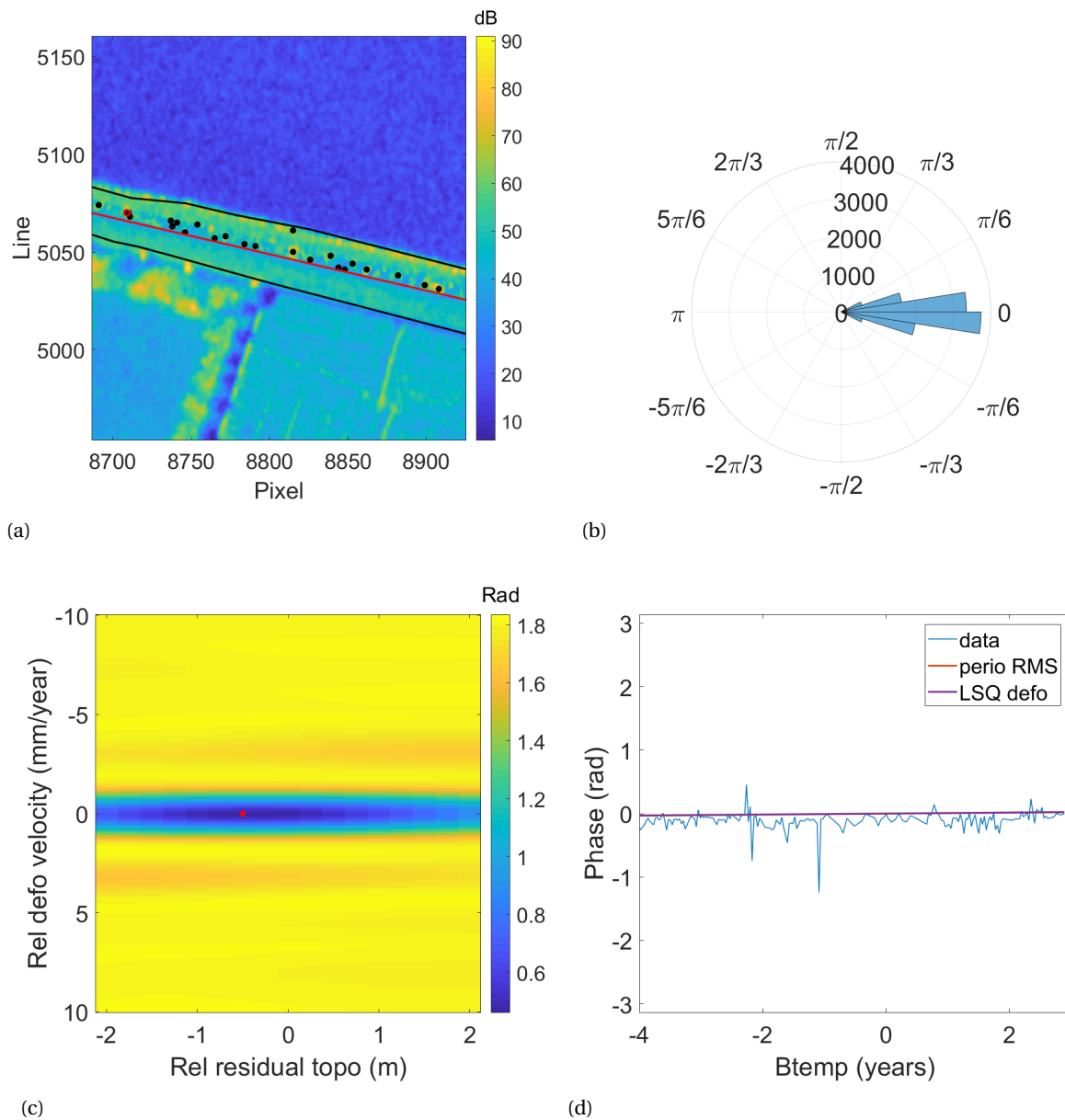


Figure 6.9: Visualization of estimated relative deformation for a point close to a PS. **(a)** Pixel for which the estimated relative deformation is visualized (in red). the red line represents the intersection between the revetment and grass cover, the black dots the PS and the black lines indicate the water boundaries. **(b)** Polar histogram of the relative (coherence based selected) interferometric phases. **(c)** Search space of periodogram method: The RMSE for each combination of relative deformation and relative residual topography is plotted. **(d)** Single master phases (master image is 12 March 2013) versus the estimated (wrapped) relative deformation phases of the periodogram and Least-Squares method.

The polar histogram in Figure 6.9b shows that the relative phases of this point with respect to the PS are close to zero. In contrast to Figure 6.8b, where the phase differences are randomly distributed, this means that the relative phases show (approximately) the same behavior over time. The search space of the periodogram method (Figure 6.9c) clearly shows only one minimum. Figure 6.9d again shows the phase time series with respect to the master image together with the estimated deformation based on the Least-Squares method and periodogram method. In this case, both methods have estimated the same solution. However, the distance of this pixel with respect to the reference PS is only a few pixels. This means that there is correlation between this pixels due to oversampling and pixel posting and the measurements are not independent.

In Figure 6.10, the estimations for the Least-Squares method and periodogram method are visualized for a point which is situated on the revetment of the outer slope of the dike, but has a larger distance to the PS

as compared to Figure 6.9. For this point, the search space of the periodogram obtains one minimum (as in Figure 6.9c), but also begins to look like the search space of the point on the grass side of the dike (Figure 6.8c).

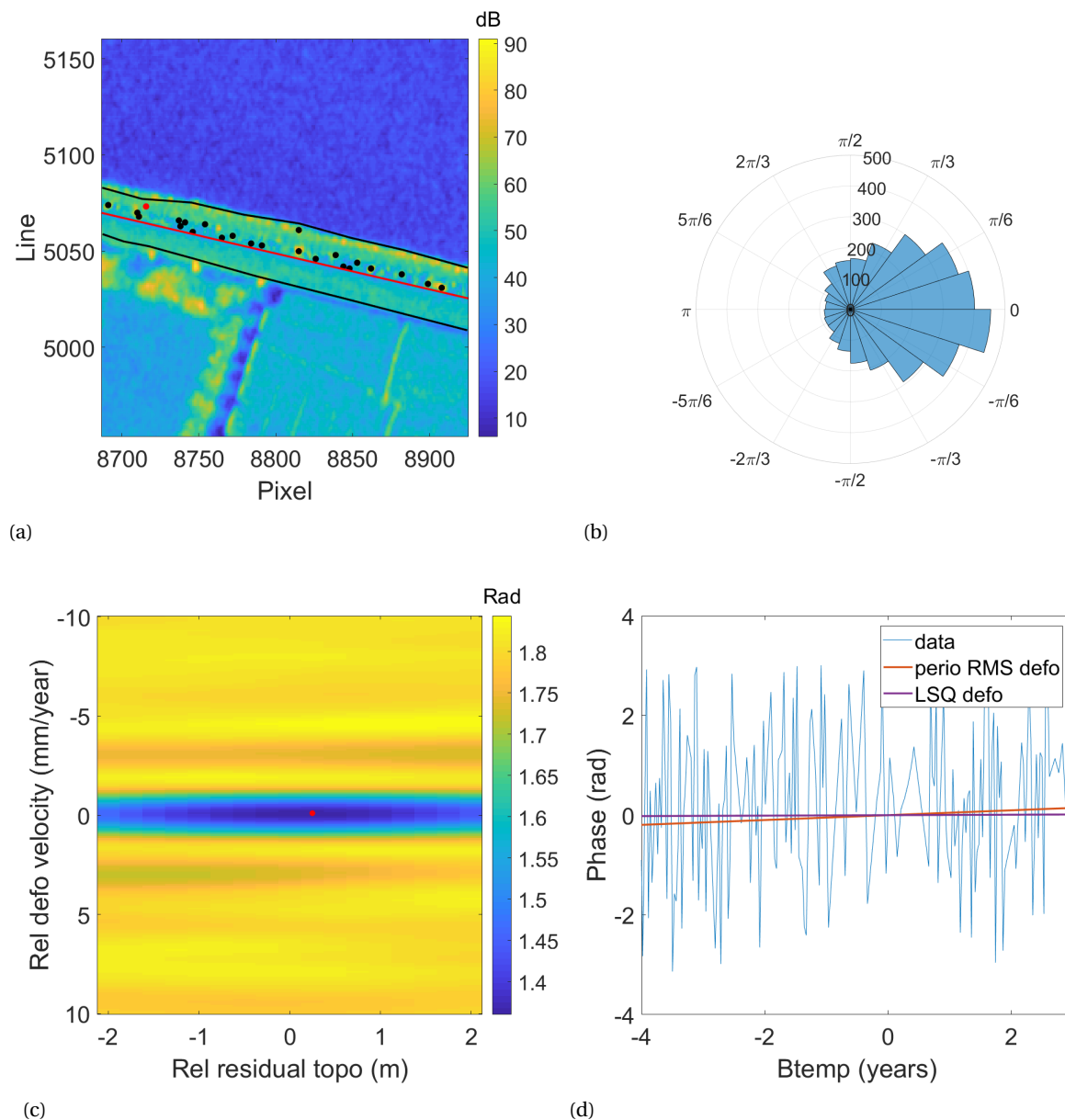


Figure 6.10: Visualization of estimated relative deformation for a point close to a PS. **(a)** Pixel for which the estimated relative deformation is visualized (in red). the red line represents the intersection between the revetment and grass cover, the black dots the PS and the black lines indicate the water boundaries. **(b)** Polar histogram of the relative (coherence based selected) interferometric phases. **(c)** Search space of periodogram method: The RMSE is for each combination of relative deformation and relative residual topography is plotted. **(d)** Single master phases (master image is 12 March 2013) versus the estimated (wrapped) relative deformation phases of the periodogram and Least-Squares method.

Although the periodogram and Least-Squares method obtain approximately the same results for pixels with a RMSE below the selected threshold of 1.25 rad, the periodogram has 742 pixels with RMSE equal to or smaller than the threshold compared to for 737 the Least-Squares method. Furthermore, in Section 5.2.2 the periodogram method performed better on the validation on as PSI analysis. Therefore, the periodogram is used in the next section to investigate the consequence of using different interferogram selection methods.

6.3.2. Comparison of interferogram selection methods

In Section 5.1, several methods were proposed to select coherent interferograms. The threshold method uses a threshold on the coherence value to select only those interferograms which have a higher coherence than the threshold. The Diagonal method only uses the first N diagonals of the coherence matrix and the Mean method applies a threshold on the mean coherence of the rows and columns of the coherence matrix. In Figure 6.11, the amount of pixels in the selected crop which have a RMSE of 1.25 radians or lower are plotted for increasing coherence thresholds. For each coherence value, the coherent interferograms are selected based on the threshold method, the relative deformation and relative residual topography are estimated according to Eq.(5.6). For each pixel in the crop, the RMSE is estimated of the estimated phases with respect to the observed phases. Then, the amount of pixels are summed which have a RMSE of 1.25 radians or lower while simultaneously having more than 60 measurements (selected coherent interferograms).

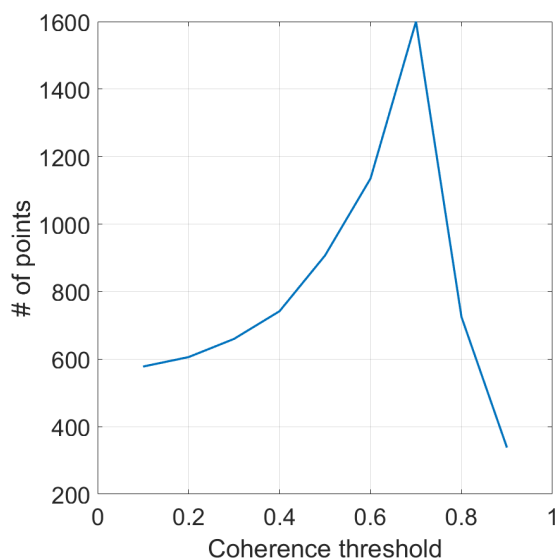


Figure 6.11: Amount of pixels in the selected crop which have a RMSE value lower or equal than 1 for the periodogram method. The selection of interferograms is based on a threshold (threshold method) which increases on the x-axis. On the y-axis the amount of pixels are shown for each threshold which have a RMSE value of 1.25 rad or less. For both methods, the periodogram method is used for the estimation of relative deformation and relative residual topography. Only pixels for which more than 60 interferograms are selected are taken into account.

The amount of pixels with RMSE lower than 1.25 rad increases up to a coherence threshold of 0.7 and then decreases as the coherence threshold increases to 0.9. For high coherence thresholds, too much interferograms are thrown away to obtain a good estimate of the relative deformation. For lower coherence thresholds, it might be that too many interferograms are taken into account which are not coherent. Lower coherent interferograms often have a larger temporal baseline which increases the temporal decorrelation. In Figure 6.12, the relative deformation map and RMSE map are visualized for a coherence threshold of 0.2 and 0.7, respectively. In Figure 6.12b, it can be seen that some estimates of relative deformation are on the vegetated part of the dike (i.e. below the red line). Comparing Figure 6.12c and 6.12d, it can be noticed that for the coherence threshold of 0.7 the range to which the pixels with low RMSE extent (with respect to the closest PS) is further as compared to the estimation with coherence threshold of 0.2. This can also be observed in the relative deformation maps (Figure 6.12a and 6.12b).

Another observation which can be made is that the extent to which the low RMSE pixels spread is anisotropic, see Figure 6.12d. If the distance to the PS increases, the RMSE of the estimation increases as well. However, the extent to which low RMSE estimations are obtained on the revetment is larger as compared to the extent to which low RMSE estimates are found on the vegetated part of the dike. If only good estimates were to be found because of spatially correlated data (originating from data pre-processing), the spread would be isotropic. This anisotropic behavior gives confidence that there is information in the estimations.

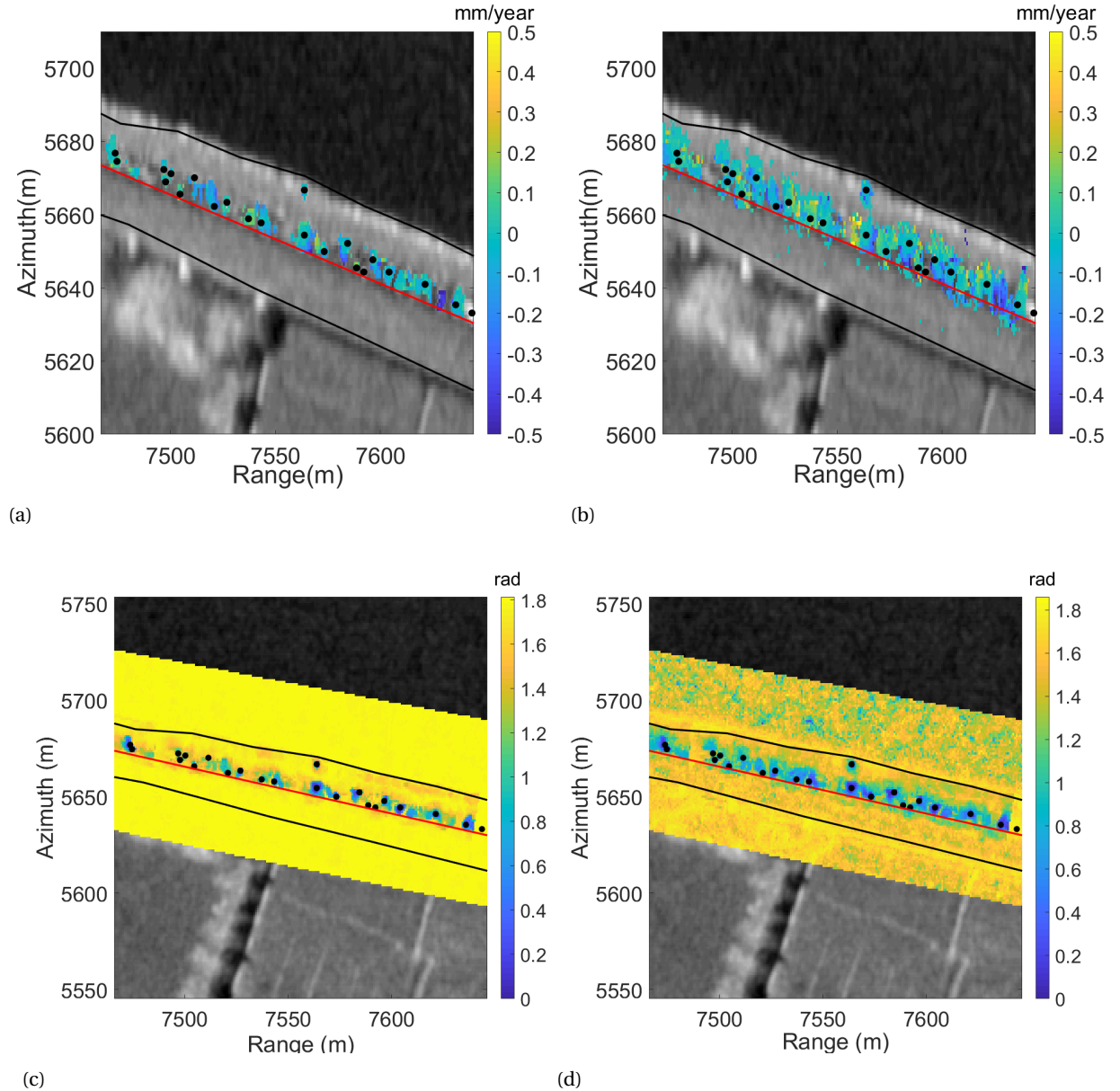


Figure 6.12: Comparison of results for the periodogram method with different coherence thresholds (threshold method). (a) Estimated deformation relative to the closest PS point for a coherence threshold of 0.2: only pixels are shown which have $RMSE \leq 1.25$ (b) Estimated deformation relative to the closest PS point for a coherence threshold of 0.7: only pixels are shown which have $RMSE \leq 1.25$. In (c) and (d), the RMSE maps of the are visualized for a coherence threshold of 0.2 and 0.7, respectively. the red line represents the intersection between the revetment and grass cover, the black dots the PS and the black lines indicate the water boundaries.

Similar plots as Figure 6.11 can be made for the Diagonal method (Figure 6.13a) and the Mean method (Figure 6.13b). For Figure 6.13a, the amount of diagonals which are used to select coherent interferograms is increased on the x-axis. On the y-axis, the amount of pixels (with the condition that more than 60 coherent interferograms are found by the selection method) which have a RMSE of 1.25 rad or lower are plotted. Here, the periodogram method is used to estimate the relative deformation and relative residual topography. The x-axis in Figure 6.13b depicts the mean threshold which is used to select only interferograms for which the mean of the coherence matrix is higher than the threshold.

The number of diagonals which are used for coherent interferogram selection is an indirect way of applying a threshold on the temporal baseline of an interferogram. The further the interferogram in the coherence matrix is away from the main diagonal, the larger the temporal baseline. The amount of pixels with

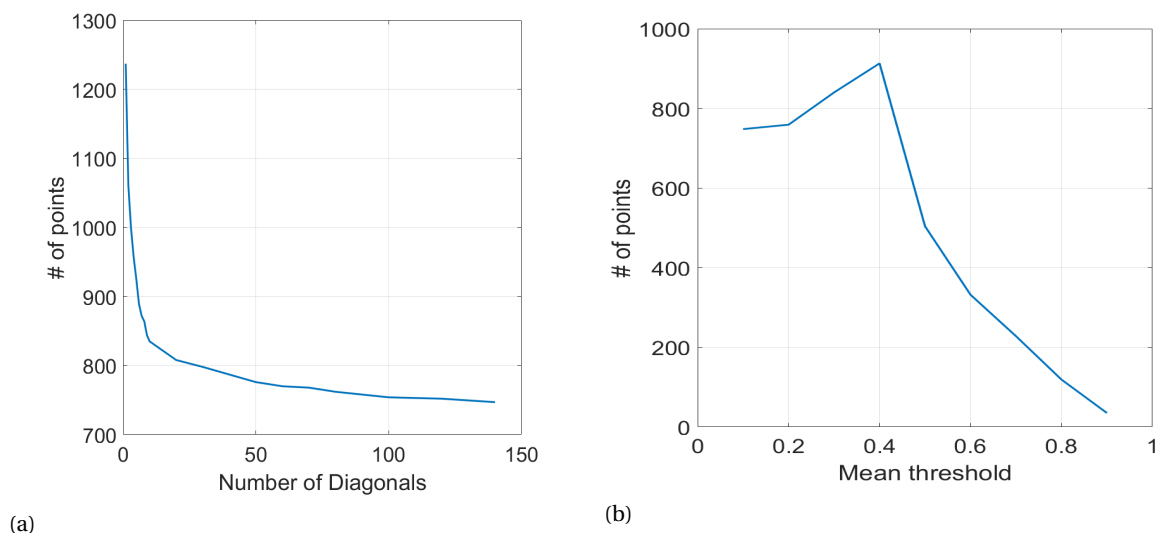


Figure 6.13: Visualization of the results of the validation method as proposed in Section 5.3. **(a)** Amount of pixels with a RMSE of 1.25 rad or lower for different number of diagonals with respect to the main diagonal (as described in Section 5.1). **(b)** Amount of pixels with a RMSE of 1.25 rad or lower for different thresholds on the mean coherence of the coherence matrix (as described in Section 5.1). For both methods, the periodogram method is used for the estimation of relative deformation and relative residual topography. Only pixels for which more than 60 interferograms are selected are taken into account.

a RMSE lower than or equal to 1.25 rad is maximal for 1 diagonals. If more than 1 diagonal is selected from the coherence matrix, the amount of pixels with $\text{RMSE} \leq 1.25$ rad decreases. The reason for this might be that if interferograms are used with a large temporal baseline, they are influenced by temporal decorrelation and only add noise to the estimation. The mean threshold implies that the mean coherence of one image with all other images should be higher than a certain threshold. In this way, a more severe threshold is applied and it is less likely that an interferogram is selected which has a accidentally high coherence. For the mean method (Figure 6.13b), a mean threshold of 0.4 on the coherence matrix will lead to the most pixels with $\text{RMSE} \leq 1.25$ rad.

The validation method applied on the different selection methods lead to maximum of 1600 estimates for the Threshold method (coherence threshold of 0.7), 1237 estimates for the Diagonal method (10 diagonals) and 913 estimates for the Mean method (mean threshold of 0.4). The optimal method (in this case study) therefore is the Threshold method with a coherence threshold of 0.7. A few estimates have been obtained on the vegetated part of the dike with $\text{RMSE} \leq 1.25$ rad and have more than 60 selected interferograms. However, the RMSE decreased rapidly with increasing distance to the PS (but the decrease is an-isotropic, see Section 6.3.2). This might have the following reasons

- There is too much noise in the data: It might be that, because of the rapid decorrelation of the vegetation on the dike, the data is too noisy to obtain a reliable estimate. For the estimation of relative deformation, in this chapter, TerraSAR-X data is used. While the resolution of this satellite is very suitable for the dike, the sensor operates at X-band wavelength. As described in Section 3.2.3, smaller wavelengths are not suitable for penetration of vegetation and therefore the temporal decorrelation term is large for X-band.
- The assumed deformation model is wrong: The RMSE is a measure of how well the data fits the assumed deformation model. If the assumed deformation is not linear, but for example is superimposed with an season dependent effect, the RMSE will be high even if there is information present in the data.

In subsection 6.3.3, the size of the multilook window is increased with the aim of reducing the phase noise. In subsection 6.3.4, an Equivalent Single Master (ESM) step is performed to reduce the noise of the phases after which the interferograms are unwrapped by taking the cumulative sum of the daisy chain phases. In Section 6.4, Radarsat-2 data is used to investigate the influence of the radar wavelength on the estimated relative deformation. Radarsat operates at C-band and therefore should be less susceptible to decorrelation.

6.3.3. Increasing multilook window

The size of the multilook window was chosen as a 9x9 window to reduce the noise in the phase observations. This relatively small window was chosen because of the small size of the dike. The multilook operation assumes ergodicity (statistical properties of neighboring pixels are the same), which may become invalid with a larger window. However, a larger window may be able to reduce more noise in the data which in the end may lead to better estimations. Therefore in this section, the size of the multilook window is increased to investigate what the influence is on the relative deformation estimates. The KS-test to select SHP is used to select only those pixels with the same amplitude behavior in time. In Figure 6.14, results of an estimation with the periodogram method using a multilooking window of 20 by 20 pixels are visualized. The results obtained with a window of 9x9 are added for comparison.

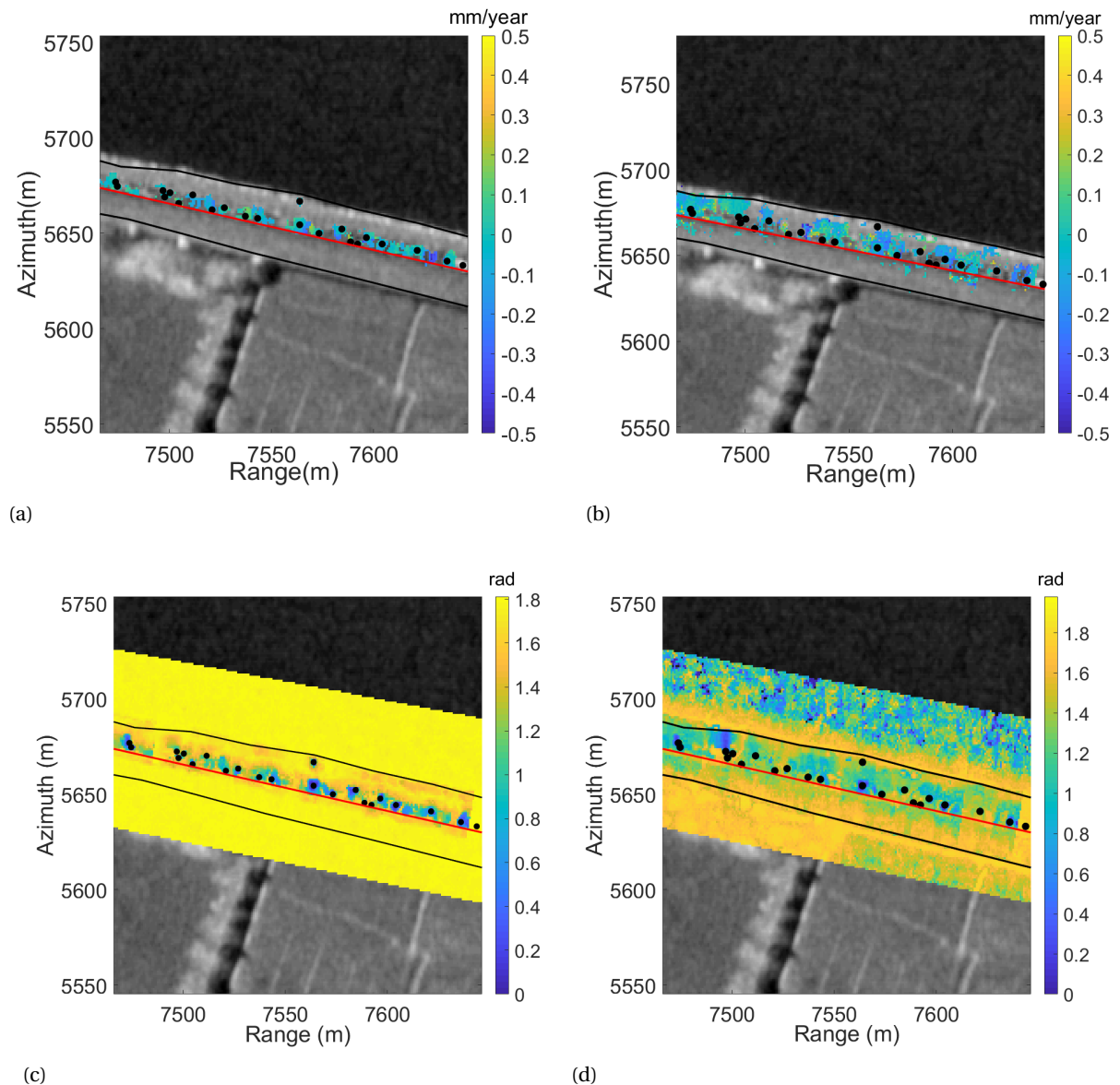


Figure 6.14: Comparison of the results obtained by the periodogram method applied on TerraSAR-X data, using different sizes of the multilook window. In (a) and (b) the estimated relative deformation (with respect to the closest PS) velocity maps for the 9x9 and 20x20 multilook window, respectively. In (c) and (d), the corresponding RMSE maps of the estimated phases with respect to the observed phases for the 9x9 and 20x20 multilook window, respectively. For both configurations, a coherence threshold of 0.4 is applied on the coherence matrix to select coherent interferograms, the red line represents the intersection between the revetment and grass cover, the black dots the PS and the black lines indicate the water boundaries.

Comparing the relative deformation maps of the 9x9 window with the 20x20 window, it can be noted that for the larger multilook window there are more estimates which are considered significant (based on the RMSE and amount of coherent interferograms). For the 20x20 window, 1510 pixels are found which have $RMSE \leq 1.25$ and simultaneously have more than 60 selected coherent interferograms. For the 9x9 window, this is 429 pixels. The amount of significant estimates is increased by more than a factor of three with increasing the multilook window from 9x9 to 20x20. Furthermore, the amount of significant estimates on the vegetated part of the dike increased for the 20x20 multilook window compared to the 9x9 window. However, compared to the 9x9 window with coherence threshold 0.7 (see Figure 6.12b), there is no significant improvement on the amount of estimates on the vegetated part of the dike. In Figure 6.15a, the amount of SHP are plotted for each pixel. Compared to the amount of SHP for the 9 by 9 window (Figure 6.5b), much more SHP are identified for the 20 by 20 window (about four times as much). With more selected SHP, the phase noise should be further reduced. In Figure 6.15b, an example of an SHP estimation window of 20 pixels in range and azimuth direction is depicted. Yellow indicate pixels which show a similar amplitude behavior over time according to the KS test. Blue pixels do not show similar amplitude behavior with respect to the reference pixel (black dot). The Kolmogorov Smirnov test does not take contextual information into account which may lead to selected SHP which do not fulfill the ergodicity condition. In Figure 6.15b, the reference pixel is situated on the inner part of the dike but also SHP are selected on the outer part of the dike. Also, SHP are selected which are not even a part of the dike. While the amplitude behavior of these pixels may be considered similar based on the KS test, the deformation behavior can be different. If these pixels are then used to compute the multi-looked phase for this pixel, they might introduce noise to this pixel instead of reducing the noise.

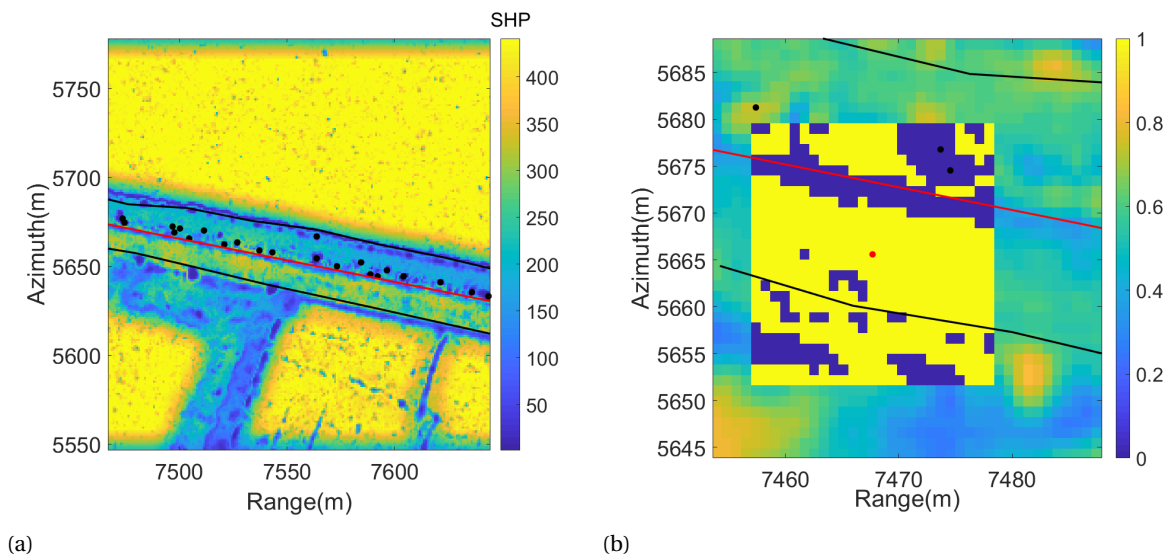


Figure 6.15: Visualization of the amount of selected SHP using the Kolmogorov-Smirnov test with a multilook window of 20 by 20 pixels. **(a)** Number of SHP for each pixel **(b)** Example of a SHP selection window of 20 pixels in range and 20 pixels in azimuth with in red the reference pixel. Pixels with a yellow color indicate pixels which show similar amplitude behavior over time with respect to the reference pixel. Pixels in blue are pixels which have amplitude behavior which is different with respect to the reference pixel. The SHP selection method does not take into account contextual information and therefore (for this grass pixel on the inner part of the dike) also SHP are selected on the outer part of the dike and outside the dike. the red line represents the intersection between the revetment and grass cover, the black dots the PS and the black lines indicate the water boundaries.

The statistical test for selecting SHP takes into account amplitude behavior over time but fails to exclude pixels which are not part of the dike. With the knowledge of the geometry of the dike, a geometric restriction can be applied such that only pixels on the vegetated part of the dike are taken into account for complex multilooking.

6.3.4. Equivalent Single Master

In the previous sections, the unwrapping of the phases was performed based on a defined deformation model. This model is an approximation of the truth but does not exactly resembles the physical deformation. If the assumed deformation model differs too much from the real deformation, the fit to the data is not good and the RMSE is high. To analyze the phase as function of time without a pre-defined deformation model, the phases can be unwrapped by the cumulative summation of the double differences over time. The closest PS is again chosen as a reference and the assumption is that there are no ambiguities between subsequent acquisitions. To reduce the noise in the data (and therefore reduce the risk of unwrapping errors), an Equivalent Single Master step is performed (see Section 3.2.5). The difference with respect to the developed methodology in Chapter 5, is that the ESM optimization step uses the full coherence matrix to estimate a new phase time-series referred to a single master image.

For this, the software of DS Delft is used as implemented by Samiei-Esfahany (2017). To solve the phase inconsistency introduced by the complex multilooking operation, the system of non-linear equations in Eq.(3.37) is solved by using a maximum likelihood (ML) estimator. This estimator was originally introduced by Guarneri and Tebaldini (2008) and was also used in the SqueeSAR algorithm by Ferretti et al. (2011). For each pixel in the crop, the ESM phase is estimated if the pixel has more than 25 SHP identified by the Kolmogorov-Smirnov test. This threshold is set because in this way the phases of the PS remain unchanged. The ESM phases are then converted to daisy chain phases and are cumulative summed to obtain a time series of unwrapped phases. Next, for each pixel, the closest PS is found which is used as a reference for the phase time series. For each time series, a linear deformation velocity (relative to the closest PS) is estimated based on a Least-Squares fit of which the RMSE is visualized in Figure 6.16a and the relative deformation map is shown in Figure 6.16b.

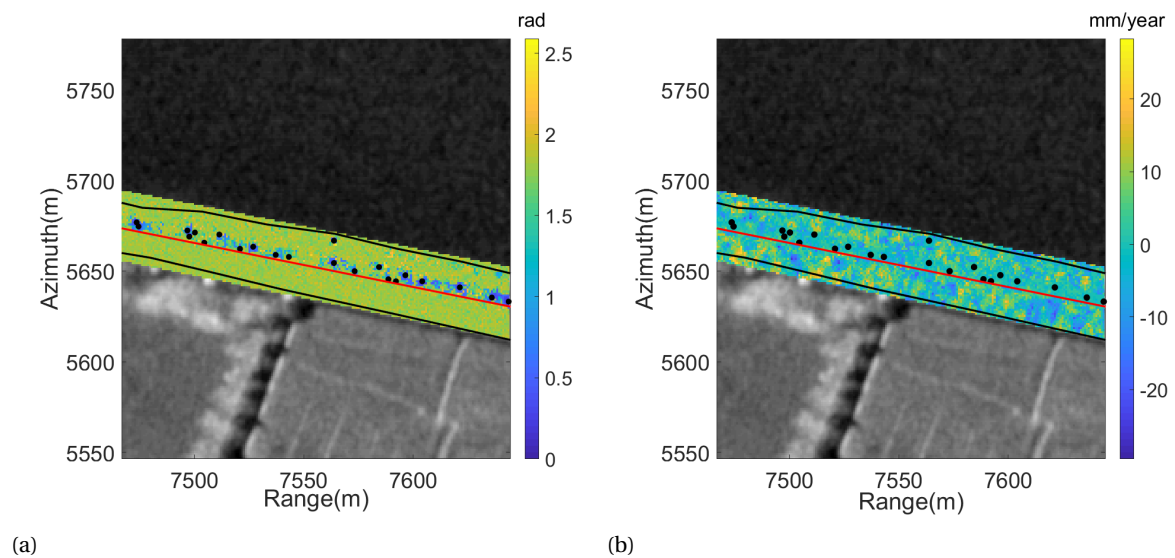


Figure 6.16: Visualization of cumulative sum of the Equivalent Single Master phases. **(a)** RMSE of a linear fit of the cumulative phases. **(b)** Estimated relative deformation velocity with respect to the closest PS. the red line represents the intersection between the revetment and grass cover, the black dots the PS and the black lines indicate the water boundaries.

The RMSE is low only close to the PS but quickly increases as the distance to the PS becomes larger. The estimation of the relative deformation is noisy and has estimations of ± 20 mm/year which is unrealistic.

In Figure 6.17, an example is shown of the unwrapped ESM phases. Figure 6.17b is an example of an estimated linear deformation for the selected point in Figure 6.17a. As can be seen, the unwrapped ESM phases do not represent a linear deformation and subsequently the estimated relative deformation of -8 mm/year is not a good representation of the unwrapped data (RMSE is 1.80 radians).

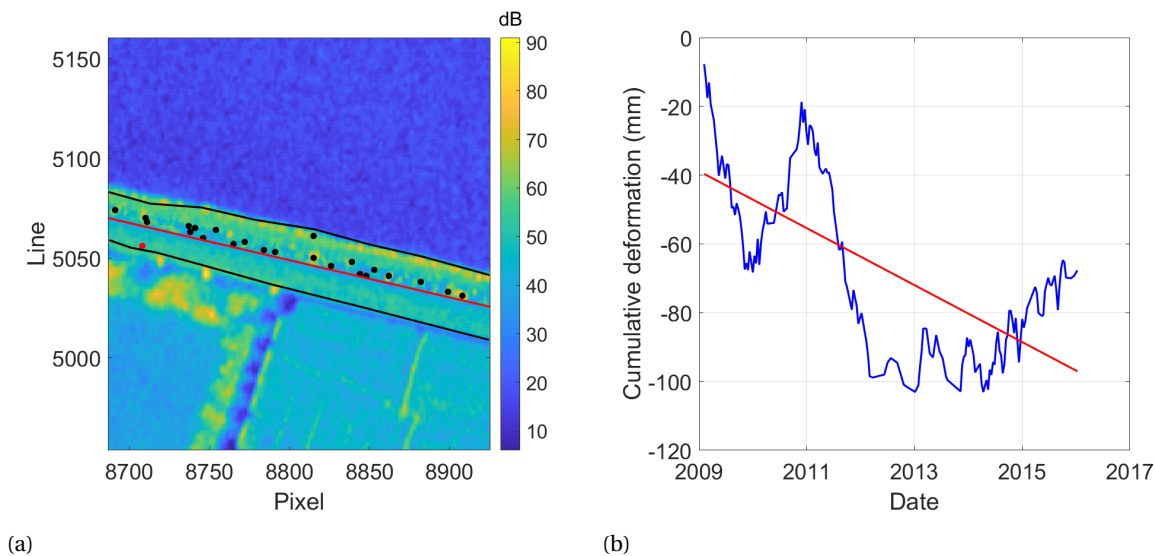


Figure 6.17: Example of an unwrapped time series, cumulatively summing the ESM phases. (a) Selected pixel in red. the red line represents the intersection between the revetment and grass cover, the black dots the PS and the black lines indicate the water boundaries. (b) Cumulative sum of the ESM phases which have been converted to daisy chain phases. A linear fit to the data has been made of which the linear term equals -8.3 mm/year with respect to the closest PS. The RMSE is equal to 1.80 radians.

Influence of temperature

To investigate the influence of temperature on the phase time series, hourly data from the KNMI is converted to a daily average in degrees Celsius for the used acquisitions. The KNMI has 35 weather stations on land and 10 on sea to measure temperature, humidity, wind, precipitation, cloudiness, radiation and fog. There are two stations which are about on equal distance to the Marken island which are the Schiphol station and Berkhout station. The Berkhout station is chosen as a reference because it is situated at the same lake (IJsselmeer lake) as the Marken island. The pixels on the dike are referenced to a PS outside of the dike. This is because, when using reference PS on the dike, the signal caused by the temperature may be canceled out. In Figure 6.18 one example of an unwrapped time series is shown. The reference PS (in red) as well as the considered pixel (in black) are shown. The reference PS is situated on a tennis court, probably a fence which acts as a stable scatterer.

An example of the unwrapped ESM daisy chain phases is depicted in Figure 6.19. In blue, the relative phase is plotted between the selected pixel and reference PS. In red (on the right y-axis), the temperature is plotted on the same date as the acquisition date. No clear correlation can be observed between the unwrapped phases and the temperature time series. This may have several reasons. One explanation is that the phase time series of the selected pixel is too noisy and therefore no temperature signal is visible in the time series. Another possible explanation is that the temperature related motion is too large to be unwrapped correctly (which is however not visible in Figure 6.19).

Multiple combinations of reference and selected points (Figure 6.18 have been tried, which all show similar behavior.

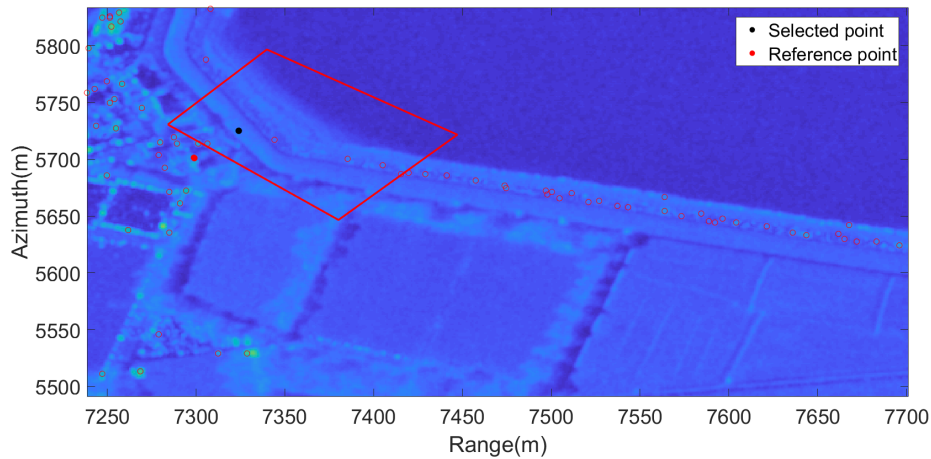


Figure 6.18: Reference point (in red) to which the phases of the selected point are related. The reference point is situated on a tennis court (probably a fence which acts as a stable scatterer). The distance between the selected point and reference point is 35 meters.

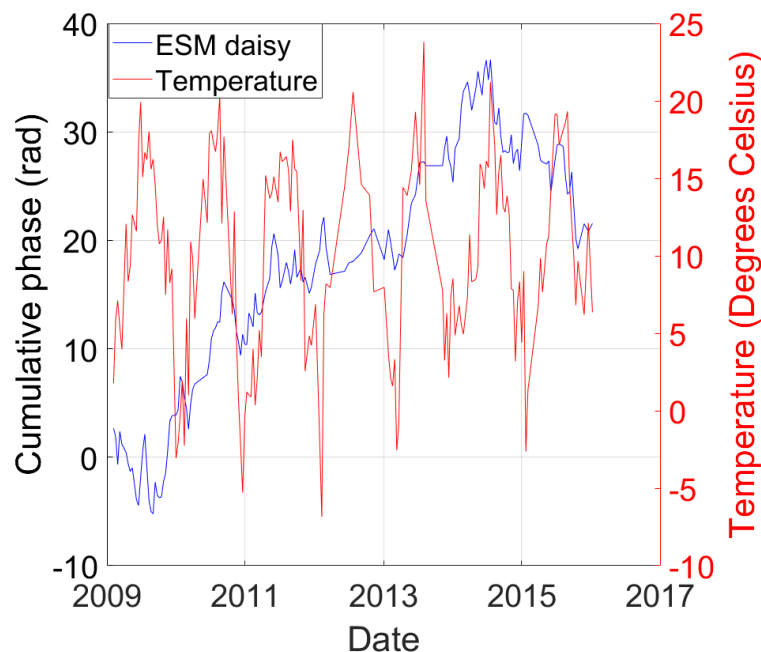


Figure 6.19: Visualization of cumulative phases together with temperature. In blue, the cumulative sum of the ESM processed relative phases between the red point and black point in Figure 6.18. On the right y-axis, the daily temperature is computed based on hourly measurements obtained from the KNMI of station Berkhout.

6.4. Application on Radarsat-2 data

As described in Section 3.2.3, the temporal decorrelation rate increases quadratic with the wavelength. For X-band this means that already after 11 days (the revisit time of TerraSAR-X), the correlation has decreased from 1.0 to 0.4. Using C-band, this decorrelation happens after 56 days (using $\sigma_0 = 1 \text{ mm}^2/\text{year}$ (Samiei-Esfahany, 2017)). Because a large part of the dike is covered with grass and thus is susceptible for decorrelation, in this section Radarsat-2 data (using a C-band sensor) is used to estimate relative deformation. A Radarsat-2 data set of 48 images ranging from March 2015 until August 2018 is available, with a revisit time of 24 days. The resolution in slant range is 5.0 m and the resolution in azimuth direction is equal to 2.8 m. Compared to the data stack of TerraSAR-X (January 2009 until January 2016), there is almost no overlap and therefore the results of TerraSAR-X and Radarsat-2 cannot be compared directly. However, the quality of the estimations can be compared. As with the TerraSAR-X stack, the SHP are computed using the KS test. These SHP are then

used to compute the multi-looked phase as well as an estimate for the coherence. A threshold is then set on the coherence matrix to select coherent interferograms. The periodogram method estimates the relative deformation with respect to the closest PS by using these coherent interferograms. In Figure 6.20a and 6.20b the maps of the estimated RMSE and relative deformation are shown, respectively.

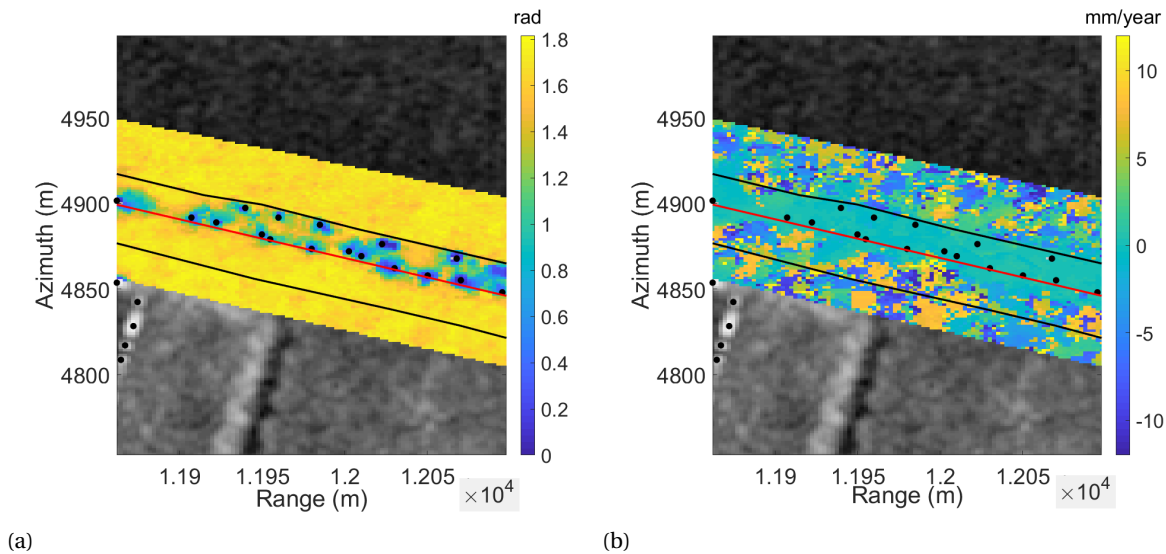


Figure 6.20: Results of the periodogram method applied on the Radarsat-2 data, using a coherence threshold of 0.4 for the selection of coherent interferograms. (a) RMSE of the estimated phases with respect to the observed phases (b) Estimated relative deformation with respect to the closest PS, using the periodogram method. the red line represents the intersection between the revetment and grass cover, the black dots the PS and the black lines indicate the water boundaries.

Most PS are found on the crest of the dike and the outer slope of the dike. Close to these PS (blue area's), the RMSE is relatively low which means that the fit with the assumed deformation model is relatively good. Further away from these points (especially on the inner part of the dike), the RMSE increases quickly and approaches 1.81 radians. The water surface serves as a good reference for indicating noisy pixels. The RMSE on the water surface is close to 1.81 radians and the estimated relative deformation has jumps from -10 to 10 mm/year. Similar behavior can be seen on some parts of the inner part of the dike. In Figure 6.21, the amount of pixels with a RMSE ≤ 1.25 is visualized for increasing coherence thresholds. On the x-axis, the coherence threshold as applied on the coherence matrix using the threshold method (Section 5.1) with on the y-axis the amount of pixels which have a RMSE ≤ 1.25 and at least 60 selected interferograms as estimated by the periodogram method.

According to Figure 6.21, a coherence threshold of 0.5 leads to most pixels with an estimated RMSE ≤ 1.25 rad for the Radarsat-2 stack. In Figure 6.22, the results for the optimal threshold for Radarsat-2 and TerraSAR-X are visualized. For TerraSAR-X this threshold is equal to 0.7 (Section 6.3.2), and for Radarsat-2 0.5. The estimated relative deformation velocity maps for the Radarsat-2 stack and TerraSAR-X stack are shown in Figure 6.22a and 6.22b, respectively. Only estimates are shown which have a RMSE ≤ 1.25 rad and for which more than 60 coherent interferograms are selected. Compared to TerraSAR-X, there are more PS on the outer slope of the dike and rubble for the Radarsat-2 data set (Figure 4.4a). There are no major differences in the location of the estimated relative deformation. For both stacks the estimates of relative deformation are mainly situated on the outer slope of the dike, in close range of the PS. However, a few estimates are obtained on

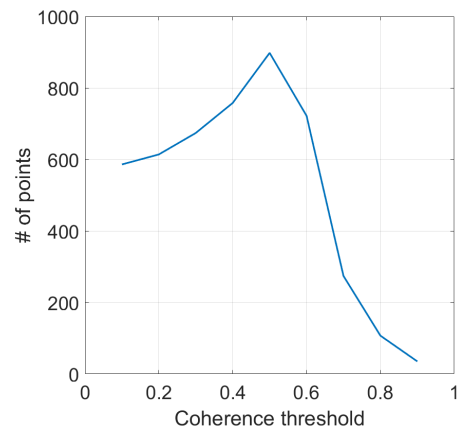


Figure 6.21: Amount of pixels in the selected crop which have a RMSE ≤ 1.25 for the periodogram method applied on Radarsat-2 data. The selection of interferograms is based on a threshold (threshold method) which increases on the x-axis. On the y-axis the amount of pixels are shown for each threshold which have a RMSE value of 1.25 or less. Only pixels for which more than 60 interferograms are selected are taken into account.

the vegetated part of the dike (i.e. below the red line) which have a $RMSE \leq 1.25$ rad and have more than 60 selected interferograms. For both stacks these points are only situated close to the crest of the dike, no estimates are obtained on the actual slope of the inner part of the dike.

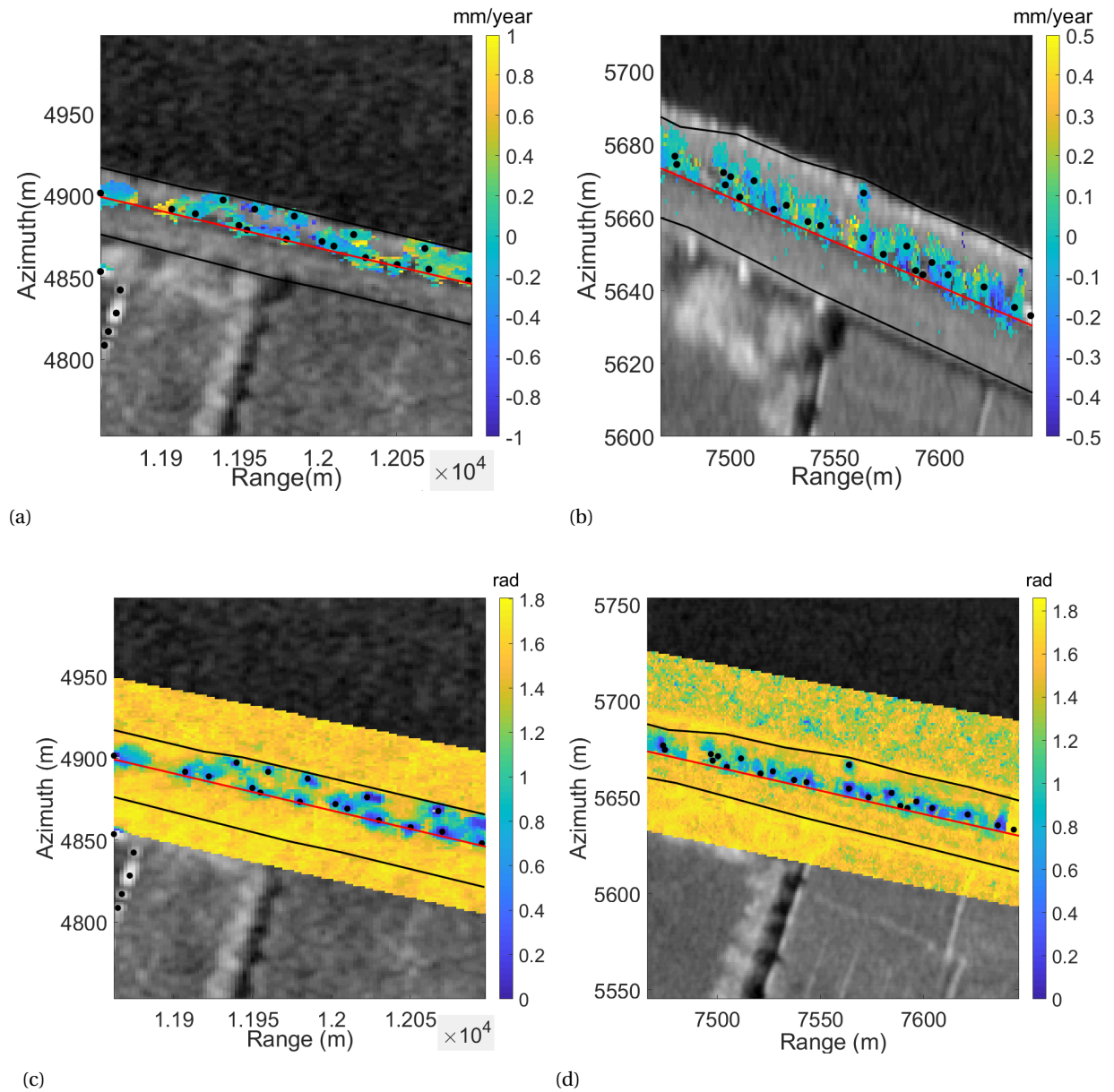


Figure 6.22: Comparison of results of TerraSAR-X data and Radarsat-2 data, using the periodogram method with a coherence threshold of 0.7 on the TerraSAR-X data and 0.5 on the Radarsat-2 data. (a) Estimated deformation relative to the closest PS point using Radarsat-2: only pixels are shown which have $RMSE \leq 1.25$ rad and more than 60 selected coherent interferograms (b) Estimated deformation relative to the closest PS point using TerraSAR-X. In (c) and (d), the RMSE maps are visualized for the TerraSAR-X stack and Radarsat-2 stack, respectively. Note that the estimations are based on a different time interval due to data availability. The TerraSAR-X uses 166 SLC images from 5 February 2009 until the first of February 2016 and the Radarsat-2 stack uses 48 SLC images ranging from 7 March 2015 until the 30th of August, 2018. the red line represents the intersection between the revetment and grass cover, the black dots the PS and the black lines indicate the water boundaries.

6.5. Discussion

In this chapter, the developed methodology in Chapter 5 was applied on two data stacks, the TerraSAR-X stack and Radarsat-2 stack. First, different statistical tests to compute SHP were compared with each other. Comparing the tests on both effectiveness and computational time, the KS test was chosen as the optimal test. Next, the Least-Squares and periodogram methods were applied on the TerraSAR-X data stack. The RMSE of the estimated deformation appeared to be relatively low for pixels close to the PS, indicating a good fit of the data to the assumed deformation model. It is important to take into account the spatial correlation due to oversampling and pixel posting (Section 4.3) in interpreting these results. Estimates of relative deformation for pixels close to a PS are not based on independent measurements and therefore have a low estimated RMSE. For both TerraSAR-X and Radarsat-2 stacks, a number of estimates are obtained on the vegetated part of the dike. These points are situated close to the crest of the dike, on the actual slope of the inner part of the dike, only a few estimates are obtained for the TerraSAR-X stack.

The estimated relative deformation map clearly showed a strip of smooth estimates on the crest of the dike. The RMSE of the estimates on this strip decreases rapidly towards the inner part of the dike (there is a clear line separating low RMSE with high RMSE) but decreases much slower towards the outer part of the dike. This anisotropic behavior indicates that there is information in the data on the outer slope of the dike. If the low RMSE estimates would only have been the result of the spatial correlation due to data processing, the spread of the RMSE would be isotropic around the PS. On the vegetated part of the dike, only a few estimates have been obtained with a $RMSE \leq 1.25$. Most estimates on the vegetated part of the inner slope have a RMSE of around 1.8 radians which can be considered noise.

The results of the Least-Squares and periodogram method were very similar. The differences between the estimated relative deformation were small and could for the large part be attributed to the resolution of the periodogram method. Close to the lake, on the rubble, the RMSE of the periodogram was lower as compared to the Least-Squares method. The benefit of the periodogram method is that it can deal with ambiguities (which is assumed to be the reason the periodogram method performed better than the Least-Squares method in the validation on a PSI analysis, see Section 5.2.2), and therefore this method was used in further analysis.

Different methods to select coherent interferograms from the coherence matrix (Section 5.1) were compared with each other based on the proposed evaluation method in Section 5.3. For every selection method, the threshold was increased and the amount of pixels in the crop were summed which had a $RMSE \leq 1.25$ and more than 60 selected coherent interferograms. Based on this method, the Threshold method with a coherence threshold of 0.7 appeared to be most effective in estimating relative deformation.

The effect of high RMSE on the vegetated part of the dike is most likely caused by temporal decorrelation. To reduce this temporal decorrelation, two approaches have been investigated. First, the multilook window was increased from 9 by 9 pixels to 20 by 20 pixels. According to Section 3.2.3, increasing the multilook factor L reduces the standard deviation of the interferometric phase (although for larger L it becomes less effective). However, for a pixel on the inner part of the dike with a multilook window of 20 by 20 pixels, the KS test also selected SHP on the outer part of the dike and even selected SHP outside the dike boundaries. This could be prevented by taken into account the contextual information of the boundaries of the dike (i.e. the boundaries could be used to exclude SHP being selected outside these boundaries).

The second approach was to reduce the temporal decorrelation by using data of a satellite with a longer wavelength. As described in Section 3.2.3, smaller wavelengths decorrelate faster as compared to longer wavelengths. Data of the Radarsat-2 satellite, which operates at C-band, was used to see whether the noise could be reduced by using a longer wavelength. Comparing the results of the Radarsat-2 stack with the TerraSAR-X stack, no significant improvements were observed. For both Radarsat-2 and TerraSAR-X, a few estimates have been obtained on the vegetated part of the dike close to the crest, but almost no estimates on the inner slope of the dike. While the longer wavelength of Radarsat-2 should reduce the decorrelation, the longer revisit time (24 days for Radarsat-2 and 11 days for TerraSAR-X) increases the temporal decorrelation (see Section 3.2.3). A satellite which possibly has a better combination of wavelength/revisit time is ALOS-2 (Advanced Land Observing Satellite-2). ALOS-2 is launched in 2014 and operates at a wavelength of 24 centimeters (L-band), which is about 8 times larger as TerraSAR-X and 4-5 times larger as compared to Radarsat-2. ALOS-2 is the follow-up mission of the ALOS mission which was in orbit between 2006 and 2012. Besides the longer wavelength increases the decorrelation time (and therefore decrease the temporal decorrelation), the ALOS-2 satellite has a revisit time of 14 days (compared to 11 days for TerraSAR-X and 24 days

for Radarsat-2) and a resolution of 3 m x 10 m in spotlight mode. In future research, it would be interesting to see whether data of the ALOS-2 satellite could lead to coherent distributed scatterers on the vegetated part of the dike.

Besides the developed methodology in which the phases were unwrapped by using a deformation model, another approach was taken in which the phases were unwrapped without using a predefined deformation model. The phases were multi-looked by using the KS-test and the DS Delft software was used to reduce the noise by using an ESM estimation step. The single master phases were then converted to a daisy chain configuration and were related to the closest PS. The phases were then cumulatively summed, assuming no ambiguities between the subsequent acquisitions. The phase time-series were very noisy and looked similar to a random walk process. To investigate whether there is a temperature signal in the phase time-series, temperature data obtained from the KNMI was used. The ESM phases were related to a nearby building outside the boundaries of the dike (which is assumed to be stable). No correlation was found between the temperature and the ESM time-series.

Comparison with State of the art

In Section 6.1, it was shown that a DSI analysis leads to 32 coherent estimates for the selected crop. Using the developed methodology, the optimal model configuration was able to find 1600 estimates with a RMSE ≤ 1.25 radians and for which more than 60 coherent interferograms were used in the estimation.

However, the correlation of pixels due to data processing (oversampling, pixel posting) is not taken into account. In Section 4.3 it was shown that, using an empirical variogram, pixels are correlated with each other over a length of six meters for TerraSAR-X data. Therefore, estimations in a range of six meter from a PS are not based on independent measurements. In fact, besides the threshold on the RMSE and the amount of selected coherent interferograms (see Section 5.3), a third threshold should be applied on an estimation of relative deformation based on the distance to the PS. In Figure 6.23, this third threshold is applied on the periodogram method with a coherence threshold of 0.7 (Threshold method). Besides the threshold of 1.25 radians on the RMSE and a minimum of 60 selected coherent interferograms, the third threshold only takes estimates into account which are on a distance of 6 m or further from the reference PS. After applying the three thresholds, 365 estimates of relative deformation have been obtained (compared to 1600 without taken into account the spatial correlation) of which 71 are situated on the vegetated part of the dike. Compared to the DS Delft method, this are more estimates. However, a few notes have to be made here. First, the restriction which is applied on the RMSE is less strict (see Section 5.3), and therefore the quality of the time-series is less as compared to DePSI (which is to be expected, since otherwise for these pixels an estimate would have been made with DePSI). Second, many of the estimates are clustered into groups of DS. The estimates within a group often show similar relative deformation patterns (partly because of multilooking) which make their estimates correlated. In Figure 6.24b and 6.24a, the deformation estimates for both the TerraSAR-X stack and Radarsat-2 stack are shown on a Google Satellite map. Here it can be seen that for both satellites, a few estimates are obtained on the vegetated part of the dike.

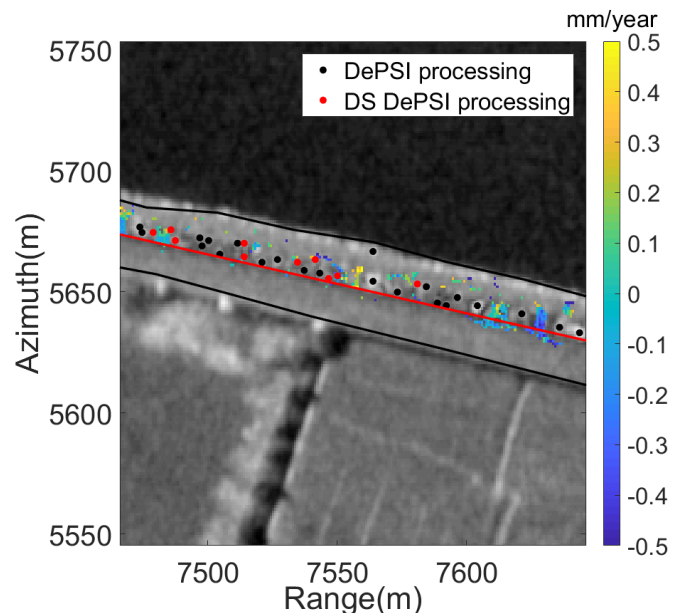
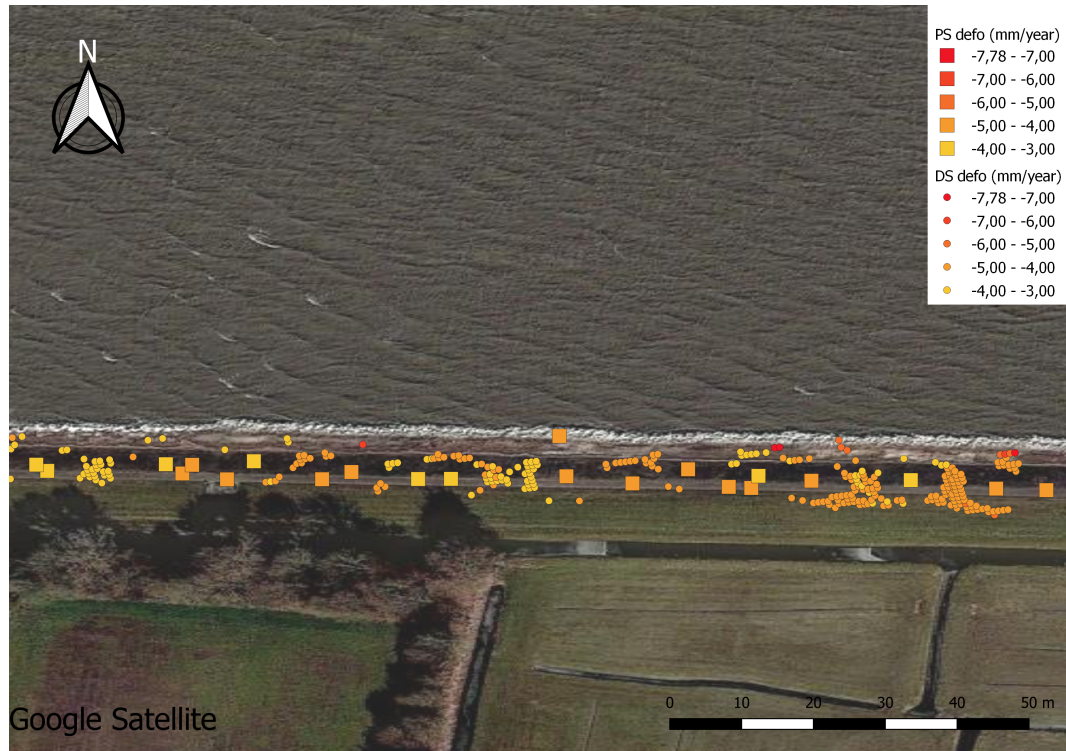


Figure 6.23: Estimates of relative deformation with respect to the closest PS obtained with the periodogram method applied on TerraSAR-X data, using a coherence threshold of 0.7 on the coherence matrix. Only estimates are visualized which have a RMSE ≤ 1.25 , have 60 or more selected coherent interferograms and have a distance of 6 m or more to the closest PS. 365 estimates are obtained after applying the thresholds (of which 71 on the vegetated part of the dike). The black dots indicate the PS as found by DePSI and the red dots indicate the DS which were obtained with the DS Delft algorithm. The red line represents the intersection between the revetment and grass cover and the black lines show the water boundaries.

quality of the time-series is less as compared to DePSI (which is to be expected, since otherwise for these pixels an estimate would have been made with DePSI). Second, many of the estimates are clustered into groups of DS. The estimates within a group often show similar relative deformation patterns (partly because of multilooking) which make their estimates correlated. In Figure 6.24b and 6.24a, the deformation estimates for both the TerraSAR-X stack and Radarsat-2 stack are shown on a Google Satellite map. Here it can be seen that for both satellites, a few estimates are obtained on the vegetated part of the dike.



(a)



(b)

Figure 6.24: Deformation visualized on a Google Satellite map. (a) TSX stack with the periodogram model and a coherence threshold of 0.7 on the coherence matrix. (b) Radarsat-2 stack with the periodogram model and a coherence threshold of 0.5 on the coherence matrix.

Conclusions and Recommendations

7.1. Conclusions

In this research a study is performed to estimate deformation time-series on grass-covered dikes. This is done by relating the phase of pixels on the dike to a Point Scatterer (PS) to eliminate a large part of the spatially correlated noise components. Different statistical tests have been implemented and compared to investigate which method is best suited to find Statistical Homogenous Pixels (SHP). Several methods have been implemented to extract coherent interferograms from the coherence matrix. Based on these coherent interferograms, relative deformation has been estimated by using two methods: the Least-Squares method and periodogram method. Another method which is implemented reduces the phase noise in the multi-looked data by performing an Equivalent Single Master (ESM) step, using full information of the coherence matrix. These steps have been performed to obtain an answer to the research question

How can InSAR techniques be optimized to detect coherent distributed scatterers and estimate their deformation time series on grass-covered dikes?

To provide an answer to the research question, this section is divided in three parts in which the sub-questions will be answered, finally leading to the answer to the main research question. First, the amount of noise in the data and the extent of spatial correlation is assessed. Next, the different implemented methods for selecting coherent interferograms and the estimation of relative deformation will be discussed as well as the influence of the radar wavelength on the results. The last part provides an answer to the main research question.

SAR Data analysis

As a point of departure, an assessment was made about the properties of the data. For this, TerraSAR-X data was used on a part of the Marken dike. The magnitude of the relative atmospheric phase and orbital phase errors in double differences was investigated by performing a PSI (Persistent Scatterer Interferometry) analysis. The deformation and residual topography, as estimated by DePSI, were subtracted from the original SLC data to obtain the relative terms of the atmospheric phase and orbital errors. It was found that the magnitude of these double differences of atmosphere and orbital errors were relatively small (standard deviation of 0.23 radians) over small distances. This conclusion (answer to sub-question 1) proofed that, using double differences over small arcs, the majority of the contributions of the atmosphere and orbital errors are canceled out. When using double differences, it is important to have independent measurements. Pixels are spatially correlated with neighboring pixels because of the oversampling and overlapping of resolution cells (pixel posting). The extent of this spatial correlation was assessed by computing empirical variograms on both an area on land and on water. Pixels which correspond with a water surface are expected to be uncorrelated with each other because of the rapid changing water surface. The range over which pixels are correlated due to processing steps, is then found by looking at the point at which the variogram stabilizes. For the TerraSAR-X data this distance appeared to be six meters (answer to sub-question 2). This result is useful in the interpretation of the results as presented in Chapter 6.

Estimating relative deformation

Building upon the answers to sub-questions 1 and 2, a method was developed to detect coherent distributed scatterers and estimate their relative deformation. This relative deformation is estimated by subtracting the phase of the closest PS from the considered pixel to reduce the atmospheric phase and orbital errors as much as possible. Different statistical tests (mean test, Kolmogorov-Smirnov (KS) and Anderson-Darling (AD) test), which were used to compute the amount of SHP for each pixel, were compared with each other. According to literature, the AD test is the most powerful (which is an extension of the KS test). The AD test and KS test proved both to be powerful in estimating SHP, while the results of the mean test deviated significantly from these tests. Based on a comparison in computation time, it was decided to use the KS test in further analysis because of its faster computation time (about 20 times faster) compared to the AD test (sub-question 3).

To estimate the relative deformation based on the observed phase differences, a Least-Squares method and periodogram method were used. In these methods, the linear relative deformation as well as the relative residual topography were estimated. To determine if an estimate is significant, three requirements were imposed on the results. First, the RMSE of the estimated fit with respect to the data must be lower than or equal to 1.25 radians. Second, at least 60 coherent interferograms must be selected from the coherence matrix to prevent a low RMSE for few data points. Third, the distance of the considered point to the PS should be smaller than six meters (to take spatial correlation into account). The Least-Squares method and periodogram method were then compared with each other based on the number of significant deformation estimates. Both methods produced similar results, the periodogram obtaining 742 significant estimates and the Least-Squares method 737 significant estimates. Because in Section 5.2.2, the periodogram method performed better (as compared to the Least-Squares method) on the validation on a PSI analysis, the periodogram method was chosen to be the best method to estimate relative deformation (sub-question 5).

Three methods have been implemented to extract coherent interferograms from the coherence matrix. The Threshold method implies a coherence threshold on the coherence matrix. All interferograms with an estimated coherence higher than this threshold are used to estimate relative deformation. The Diagonal method only uses the first N diagonals from the coherence matrix (indirectly implying a threshold on the temporal baseline). Lastly, the mean method applies a threshold on the mean coherence along the columns and rows of the coherence matrix. Only columns and rows which have a mean coherence higher than this threshold are used to estimate relative deformation. The three coherent interferogram selection methods were compared as follows. For each method, the threshold was increased and the number of significant estimates were counted for each calculation. The threshold which lead to most significant estimates, was considered to be most powerful (i.e. to extract the most information from the coherence matrix). For the TerraSAR-X data stack, the Threshold method with a coherence threshold of 0.7 turned out to be most powerful (sub-question 4). For the Radarsat-2 data stack, the Threshold method with a coherence threshold of 0.5 was found to be optimal.

Most coherent scatterers were obtained on the outer slope of the dike (covered with revetment). On the vegetated part of the dike, a number of estimates were obtained close to the crest of the dike. However, as the distance from the crest increased, the RMSE quickly increased and no DS could be detected with the developed methodology. One explanation for this is that the sensor of the TerraSAR-X satellite operates at X-band which has a small wavelength (0.031 m). Smaller wavelengths are not able to penetrate the vegetation and therefore the decorrelation time of these vegetated areas is very short. Using a satellite with a larger wavelength could lead to a slower decorrelation rate. To investigate this hypothesis, Radarsat-2 data was used to estimate relative deformation. Radarsat-2 operates at C-band which has a wavelength of 0.056 m. Downsides of Radarsat-2 with respect to TerraSAR-X are that the revisit time is longer (24 days for Radarsat-2 and 11 days for TerraSAR-X) and the resolution of Radarsat-2 is lower as compared to the TerraSAR-X satellite. The results of the Radarsat-2 data could not directly be compared with the TerraSAR-X satellite due to data time spans (data for TerraSAR-X was available from February 2009 until 2016 and Radarsat-2 from March 2015 to August 2018). However, by visually inspecting the results it could be concluded that there was no significant improvement. Using the Radarsat-2 stack, most estimates were obtained on the outer slope of the dike, while a few estimates were obtained on the vegetated part of the dike close to the crest. Just as with the TerraSAR-X stack, the RMSE increased rapidly for pixels further away from the crest. A satellite which could perform better on the vegetated part of the dike is the ALOS-2 mission. This satellite operates at L-band (wavelength of 24 cm), has a revisit time of 14 days and approximately has the same resolution as the TerraSAR-X mission. However, due to the limited time-span of this thesis, no data of the ALOS-2 mission has been applied to the

developed methodology.

Another explanation of the high RMSE for most of the pixels could be the choice of a wrong deformation model. Using a wrong deformation model to fit the data will also result in a high RMSE. To analyze this hypothesis, the phases were unwrapped without using a defined deformation model. This unwrapping was performed by taking the cumulatively sum of the daisy chain phases. The assumption for this unwrapping method is that the temporal baselines between subsequent acquisitions is short enough such that there are no jumps in the phase between acquisitions. To further reduce the noise in the data, an Equivalent Single Master (ESM) step was performed on the data. The purpose of this ESM step is to estimate a single master stack of consistent phases based on a stack of inconsistent multi-looked interferograms. From a physical perspective, this means that the decorrelation noise is reduced. The unwrapped time series, using the ESM phases, did not show a consistent behavior. Relative deformation rates of ± 20 mm/year were estimated which is unrealistic. By visually inspecting the unwrapped time series for several pixels, it was observed that the cumulative sum of the phases showed random behavior. Therefore this analysis of cumulatively unwrapping the interferometric phases could neither prove nor disprove the hypothesis that a wrong deformation model was used to fit the data.

Overall conclusions

Having formulated an answer to the sub-questions, the most important points are listed below which are considered most important to answer the main research question

How can InSAR techniques be optimized to detect coherent distributed scatterers and estimate their deformation time series on grass-covered dikes?

The short answer to this question is that, during this research, it was possible to detect coherent DS on some parts of the vegetated part of the Marken dike. However, as the distance from the crest of the dike increased, the RMSE increased and therefore no DS could be detected. The most important points are listed below which have led to the answer to the research question.

- Several methods have been used to estimate relative deformation. Two methods have been implemented to estimate relative deformation (Least-Squares method and periodogram method). Also, three different methods to select coherent interferograms have been investigated. These different methods have been analyzed by changing the threshold which was applied on the coherence matrix. Eventually, a threshold of 0.7 applied on the Threshold method was considered to be most effective in estimating relative deformation. With this method, it was possible to estimate deformation time series for some pixels on the vegetated part of the dike. Two approaches have been used to increase the amount of estimates on the vegetated part of the dike. The multilook window was increased from 9x9 to 20x20 which did not improve the capability of detecting coherent DS on the vegetated part of the dike. With larger dimensions for the multilook window, it appeared that for a pixel on the vegetated part of the dike also SHP were selected on the revetment and even outside the boundaries of the dike. Using contextual information about the dike (surface properties and dike boundaries), the complex multilooking could be improved which may lead to more detected DS on the vegetated part of the dike. Another approach to decrease the scattering noise is by using a sensor with a larger wavelength. Radarsat-2 data was used (which operates at C-band), but the results did not lead to an increase in detected DS on the vegetated part of the dike. Next to the developed methodology, another unwrapping method was investigated which does not use a pre-defined deformation model but unwraps the phases cumulatively after the noise was reduced with an ESM optimization step. This led to noisy unwrapped time-series which showed similar behavior as a random walk. By relating the ESM phases of pixels on the dike to a stable scatterer on a nearby building, the influence of temperature was investigated. However, no correlation could be found between the unwrapped time-series and the temperature.

- Scattering noise is the dominant factor in the double differences. Scattering noise appeared to be of large influence on the estimation of relative deformation. While a few DS were detected on the vegetated part of the dike, for most pixels the RMSE of the estimated phases with respect to the observed phases was too high (close to 1.81 radians). Temporal decorrelation is proportional to the wavelength of the signal as well as the time interval between acquisitions. TerraSAR-X operates at a small wavelength of 3.1 cm (X-band) and is thus susceptible to the decorrelation phenomena. Using Radarsat-2 data, which is acquired with a C-band ($\lambda = 5.3$ cm) sensor, no significant change in the amount of coherent scatterers on the vegetated part of the dike was observed. While the wavelength of Radarsat-2 is larger as compared to TerraSAR-X, the revisit time is longer (24 days for Radarsat-2 and 11 days for TerraSAR-X) which increases the decorrelation. Another option, which was not investigated in this research due to the limited time span, is to use the ALOS-2 satellite. ALOS-2 operates at L-band ($\lambda = 24$ cm), has a 14 day revisit time and has comparable resolution to TerraSAR-X.
- Spatial correlation must be taken into account in assessing the results. The developed method estimates pixel-wise relative deformation with respect to the pixels closest PS. If the distance to the PS becomes small, the phase time-series of the considered pixel and PS are correlated to each other because of oversampling and pixel posting. The phase difference between the pixel and PS becomes close to zero. If then a linear deformation model is fitted to the data, it estimates a trend of zero relative deformation with a small RMSE. The spatial correlation of the TerraSAR-X data stack was assessed by computing an empirical variogram of a cropped area on the water surface. Pixels in water are assumed to be uncorrelated and their phases uniformly distributed between $-\pi$ and π . A correlation length of six meters was found (based on the variogram), which can be attributed to oversampling and pixel posting. This correlation length was applied as a threshold on the estimated relative deformation. Only pixels of which the distance to the reference PS is larger than six meters are taken into account.

For the selected crop on the Marken Island, 365 estimates were obtained of which 71 were situated on the vegetated part of the dike. However, many of these pixels are clustered into groups of pixels which show similar behavior (i.e. are correlated to each other). These estimates could be averaged to obtain one estimate per clustered group of pixels.

7.2. Recommendations

The conclusions which have been formulated in the previous section have led to the following recommendations for future research

- Apply the developed algorithm on a larger crop. In this study only a small crop of the Marken island was studied to decrease computation time. On this crop, two groups of DS were detected on the vegetated part of the dike. It would be interesting to see if on other parts of the dike similar groups of DS could be detected.
- Analyze unwrapped phases of estimates on vegetated part of the dike. Due to the limited time span of this thesis, no analysis was performed for the unwrapped phases of the detected DS on the vegetated part of the dike. More insight on why these pixels were detected as coherent DS could improve the understanding of results and settings of the algorithm.
- Compare Radarsat-2 with TerraSAR-X using equal time spans. The available data sets of TerraSAR-X and Radarsat-2 have only a few months of overlap, making a direct comparison of the results not feasible. It would be interesting to compare the results of TerraSAR-X and Radarsat-2 with the same time frame to investigate the influence of a different sensor and longer revisit time.
- Take contextual information into account in the estimation of SHP. When increasing the amount of looks which are used for complex multilooking, the multilook window overlaps the different surface types of a dike. In principle, the statistical tests should be able to select those pixels which show similar amplitude behavior. However, in some cases the statistical test also selects pixels which are situated outside the boundaries of the dike. Instead of reducing the noise, these pixels only introduce noise and should be excluded for complex multilooking. With the known boundaries of the dike, these pixels could be excluded in advance. Furthermore, the optimal size of this multilook window should be investigated. In this research, several sizes were used but no study was done with respect to the optimal size of this window together with the applied threshold on the coherence matrix.

- Apply the developed methodology on ALOS-2 data. It was found that temporal decorrelation has a large influence on the estimation of relative deformation. Temporal decorrelation is dependent on the wavelength of the sensor (smaller wavelengths decorrelate quicker) and the revisit time (longer revisit times lead to more temporal decorrelation) of the satellite. The ALOS-2 (L-band, 24 cm) satellite operates at a longer wavelength as compared to TerraSAR-X (X-band, 3.1 cm) and Radarsat-2 (5.6 cm) and has a relatively short revisit time (14 days). This combination of wavelength and revisit time should reduce the temporal decorrelation and possibly improves the estimation on the vegetated part of the dike.
- Include covariances of selected interferograms in covariance matrix. In the developed methodology, coherent interferograms are selected which are taken into account to estimate relative deformation. The standard deviation of the interferometric phase is estimated for these observations and is used to properly weight the observations. However, the covariances between the different selected interferograms are neglected in this thesis. For example, if one interferogram is used between image 2 and 5 and another image between 2 and 4, there is correlation between these interferograms because of the same image being present in both interferograms.
- Use spatial correlation length to reduce data and obtain multiple data sets: The length over which pixels are correlated was estimated to be six meters, which is equal to a length of around four pixels. This means that every fifth pixel is an independent measurement. The original data set could thus be reduced to every fifth pixel. In this way different data sets could be obtained for which four examples are depicted in Figure 7.1. These different data sets could for example be used to obtain multiple unwrapped deformation time series.

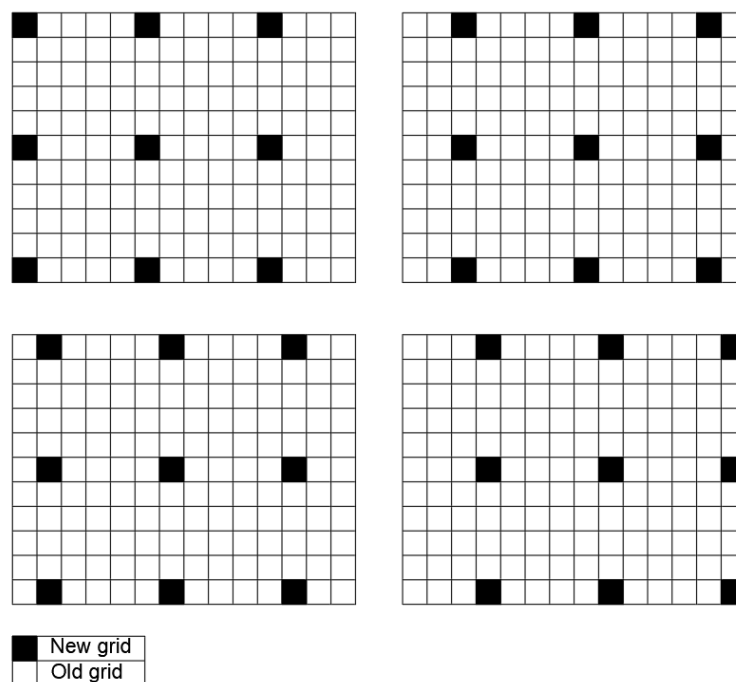


Figure 7.1: Different examples of selecting every fifth pixel in a data set to obtain independent measurements. A correlation length of four pixels is assumed.

Bibliography

- Airbus (2014). TerraSAR-X Image Product Guide. *Airbus Defense and Space*.
- Anderson, T. and Darling, D. (1952). Asymptotic theory of certain "Goodness of Fit" Criteria Based on Stochastic Processes. *JSTOR*, 1:193–212.
- Baars, S. V. (2004). Dutch Dike Breach, Wilnis 2003. *Fifth International Conference on Case Histories in Geotechnical Engineering*.
- Baars, S. V. and van Kempen, I. (2009). The Causes and Mechanisms of Historical Dike Failures in the Netherlands. *European Water Association*.
- Barends, F., Dillingh, D., Hanssen, R., and van Onselen, K. (2005). *Bodemdeling langs de Nederlandse Kust, 'Case Hondsbossche en Pettemer Zeewering'*.
- Berardino, P., Fornaro, G., Lanari, R., and Sansoti, E. (2002). A New Algorithm for Surface Deformation Monitoring Based on Small Baseline Differential SAR Interferograms. *IEEE Transactions On Geoscience And Remote Sensing*, 40:2375–2383.
- Bermon, T. (2008). The consequences of adjoining pixel processing in persistent scatterer interferometry. Master's thesis, Delft University of Technology.
- Bähr, H. and Hanssen, R. (2012). Reliable estimation of orbit errors in spaceborne SAR interferometry. *Journal of Geodesy*, 86:1147–1164.
- Bock, Y. and Melgar, D. (2016). Physical applications of GPS geodesy: a review. *Reports on Progress in Physics*, 79:1–119.
- Ciampalini, A., Bardi, F., Bianchini, S., Frodella, W., Ventisette, C. D., Moretti, S., and Casagli, N. (2014). Analysis of building deformation in landslide area using multisensor PS-InSAR technique. *Elsevier*, 33:166–180.
- Clementini, C. (2014). A geotechnical based approach for dike monitoring by permanent scatterer interferometry. Master's thesis, Politecnico Di Milano.
- CSA (2015). Satellite characteristics Radarsat-2. <http://www.asc-csa.gc.ca/eng/satellites/radarsat/radarsat-tableau.asp>. Accessed January 2, 2019.
- Danisch, L., Chrzanowski, A., Bond, J., and Bazanowski, M. (2008). Fusion of Geodetic and MEMS Sensor For Integrated Monitoring and Analysis of Deformations. *Symposium on Deformation Measurement and Analysis*.
- Dentz, F., van Halderen, L., Possel, B., Esfahany, S. S., Slobbe, C., and Wortel, T. (2006). On the potential of satellite radar interferometry for monitoring dikes of the Netherlands. *POSEIDON Project final report, Faculty of Aerospace engineering, TU Delft*.
- Dutchdikes.net (2018). Dike History. <http://dutchdikes.net/history/>. Accessed November 28, 2018.
- Engdahl, M. (2013). *Multitemporal InSAR in land-cover and vegetation mapping*. PhD thesis, Aalto University.
- Fern, J., de Lange, D., C.Zwanenburg², and Teunissen², J. A. M. (2015). Centrifuge Tests of Dyke Collapses on Soft Subsoil. *International Symposium on Geohazards and Geomechanics*.
- Ferretti, A., Fumagalli, A., Novali, F., Prati, C., Rocca, F., and Rucci, A. (2011). A New Algorithm for Processing Interferometric Data-Stacks: SqueeSAR. *IEEE Transactions On Geoscience And Remote Sensing*, 49:3460–3470.

- Ferretti, A., Prati, C., and Rocca, F. (2000). Nonlinear subsidence rate estimation using permanent scatterers in differential SAR Interferometry. *IEEE Transactions On Geoscience And Remote Sensing*, 38:2202–2212.
- Ferretti, A., Prati, C., and Rocca, F. (2001). Permanent Scatterers in SAR Interferometry. *IEEE Transactions On Geoscience And Remote Sensing*, 39:8–20.
- Fornaro, G., Verde, S., Reale, D., and Pauciuolo, A. (2015). CAESAR: An Approach Based on Covariance Matrix Decomposition to Improve Multibaseline-Multitemporal Interferometric SAR Processing. *IEEE*, 53:2050–2065.
- Goel, K. (2012). *Advanced Stacking Techniques and Applications in High Resolution SAR Interferometry*. PhD thesis.
- Guarnieri, A. M. and Tebaldini, S. (2008). On the Exploitation of Target Statistics for SAR Interferometry Applications. *IEEE*, 46:3436–3443.
- Hanssen, R. (2001). *Radar interferometry, Data interpretation and error analysis*. PhD thesis, Delft University of Technology.
- Hanssen, R. (2004). Stochastic modeling of time series radar interferometry. *IEEE*.
- Hanssen, R. and van Leijen, F. (2008a). Monitoring water defense structures using radar interferometry. In *Proceedings of Radar Conference IEEE*.
- Hanssen, R. and van Leijen, F. (2008b). Monitoring water defense structures using radar interferometry. *IEEE*.
- H.J.Verhagen (1998). *Revetments, Sea-dikes and River-Levees*. Delft University of Technology.
- Hoes, O. and Hut, R. (2018). Blog 3: One meter of sea level rise: 2.6 million additional Dutch people living below sea level. <https://www.tudelft.nl/citg/over-faculteit/afdelingen/watermanagement/research/chairs/water-resources/water-resources-management/blog/blog-3-one-meter-of-sea-level-rise-26-million-additional-dutch-people-living-below-sea-level/>. Accessed March 04, 2018.
- Hooper, A., Segall, P., and Zebker, H. (2007). Persistent scatterer interferometric synthetic aperture radar for crustal deformation analysis, with application to Volcán Alcedo, Galápagos. *Journal Of Geophysical Research*, 112.
- Hooper, A., Zebker, H., Segall, P., and Kampes, B. (2004). A new method for measuring deformation on volcanoes and other natural terrains using InSAR persistent scatterers. *Geophysical Research Letters*, 31.
- Huang, Q., Crosetto, M., Monserrat, O., and Crippa, B. (2017). Monitoring and Evaluation of a Long-Span Railway Bridge Using Sentinel-1 Data. *ISPRS*, IV-2/W4:457–463.
- H.Verheij, G.Hoffmans, B.Hardeman, and M.Paulissen (2012). Erosion at transitions in landward slopes of dikes due to wave overtopping. *International Conference on Scour and Erosion (ICSE)*, 224.
- Idris, F. A., Buhari, A. L., and Adamu, T. U. (2016). Bessel Functions and Their Applications: Solution to Schrödinger equation in a cylindrical function of the second kind and Hankel Functions. *International Journal of Novel Research in Physics Chemistry and Mathematics*, 3:17–31.
- Infomil.nl (2018). Normering regionale waterkeringen. <https://www.infomil.nl/onderwerpen/lucht-water/handboek-water/thema%27s/waterveiligheid-0/normering-regionale/>. Accessed November 28, 2018.
- Jonkman, S. N., Hillen, M. M., Nicholls, R. J., Kanning, W., and van Ledden, M. (2013). Costs of Adapting Coastal Defenses to Sea-Level Rise—New Estimates and Their Implications. *Journal of Coastal Research*, 29:1212–1226.
- Just, D. and Bamler, R. (1994). Phase statistics of interferograms with applications to synthetic aperture radar. *Applied optics*, 33:4361–4368.
- Kanning, W. (2005). Safety format and calculation methodology slope stability of dikes. Master's thesis, Delft University of Technology.

- Kanning, W. (2012). *The Weakest Link - Spatial Variability in the Piping Failure Mechanism of Dikes*. PhD thesis, Delft University of Technology.
- Kolmogorov, A. (1933). Sulla determinazione empirica di una legge di distribuzione. *G. Inst. Ital. Attuari*, 4:83–91.
- Leijen, F. V. (2018). Failure mechanisms and visual inspection. University Lecture.
- Liu, S. (2012). *Satellite radar interferometry: estimation of atmospheric delay*. PhD thesis, Delft University of Technology.
- Matlab (2018). Symbolic Math Toolbox User's Guide. *MathWorks*.
- M. Born, Wolf, E., and Bhatia, A. (1959). *Principle of optics*. New York: Pergamon Press.
- Morishita, Y. and Hanssen, R. (2015a). Deformation Parameter Estimation in Low Coherence Areas Using a Multisatellite InSAR Approach. *IEEE Transactions On Geoscience And Remote Sensing*, 53:4275–4283.
- Morishita, Y. and Hanssen, R. (2015b). Temporal Decorrelation in L-, C-, and X-band Satellite Radar Interferometry for Pasture on Drained Peat Soils. *IEEE Transactions On Geoscience And Remote Sensing*, 53:1096–1104.
- Ozer, I. E., van Leijen, F., Jonkman, S., and Hanssen, R. (2018). On the Use of Satellite Radar Imaging to Monitor the Conditions of Levees (in progress).
- Parizzi, A. and Brcic, R. (2011). Adaptive InSAR Stack Multilooking Exploiting Amplitude Statistics: A Comparison Between Different Techniques and Practical Results. *IEEE*, 8:441–445.
- Pettitt, A. (1976). A two-sample Anderson-Darling rank statistic. *Biometrika*, 63:161–168.
- Pinel, V., Poland, M., and Hooper, A. (2014). Volcanology: Lessons learned from Synthetic Aperture Radar imagery. *Journal of Volcanology and Geothermal Research*, 289:81–113.
- Rijkswaterstaat (2009). Waterwet. *Ministry of Infrastructure and Water*.
- Samiei-Esfahany, S. (2017). *Exploitation of Distributed Scatterers in Synthetic Aperture Radar Interferometry*. PhD thesis, Delft University of Technology.
- Smirnov, N. (1936). Sur la distribution de w^2 (criterium de M.R. v. Mises). *Com. Rend. Acad. Sci*, 202:449–452.
- Tofani, V., Raspini, F., Catani, F., and Casagli, N. (2013). Persistent Scatterer Interferometry (PSI) Technique for Landslide Characterization and Monitoring. *MDPI*, 5:1045–1065.
- Tough, R. J. A. (1991). Interferometric Detection of Sea Ice Surface Features. *Memorandum Royal Signals and Radar Establishment*, 4446.
- Tough, R. J. A., Blacknell, D., and Quegan, S. (1995). A statistical description of polarimetric and interferometric synthetic aperture radar data. *Sheffield Centre for Earth Observation Science*, pages 567–589.
- Touzi, R., Lopes, A., Bruniquel, J., and Vachon, P. (1996). Unbiased estimation of the coherence function: Implications in SAR interferometry. *IEEE*.
- van den Berg, F. P., Heaton, J., and Moen, W. (2013). Real time monitoring of levees through sensor technology along the Yellow River. *Deltares, Delft*.
- van Geel, B., Hallewas, D., and Pals, J. (1982). A late Holocene Deposit Under the Westfrieze Zeedijk Near Enkhuizen (prov. of Noord-Holland, the Netherlands): Palaeoecological and Archaeological. *Review of Palaeobotany and Palynology*, 38:269–335.
- van Goor, B. (2011). Change detection and deformation analysis using terrestrial laser scanning. Master's thesis, Delft University of Technology.
- van Haegen, M. S. (2017). Regeling veiligheid primaire waterkeringen. *Ministry of Infrastructure and Environment*.

- van Hoven, A., Hardeman, B., van der Meer³, J., and Steendam⁴, G. (2010). Sliding Stability of Landward Slope Clay Cover Layers of Sea Dikes Subject to Wave Overtopping. *Deltares*.
- van Leijen, F. (2014). *Persistent Scatterer Interferometry based on geodetic estimation theory*. PhD thesis, Delft University of Technology.
- Vergouwe, R. (2015). De veiligheid van Nederland in kaart.
- Wei, M. and Sandwell, D. (2010). Decorrelation of L-Band and C-Band Interferometry Over Vegetated Areas in California. *IEEE*, 48:2942 – 2952.
- Weijers, J., Elbersen, G., Koelewijn, A., and Pals, N. (2009). Macrostabieleit IJkdijk: Sensor- en meettechnologie. *Rijkswaterstaat*.
- Zebker, H., Rosen, P., and Hensley, S. (1996). Atmospheric effects in interferometric synthetic aperture radar surface deformation and topographic maps. *Journal of Geophysical Research*, 102:7547–7563.
- Zebker, H. and Villasenor, J. (1992). Decorrelation in Interferometric Radar Echoes. *IEEE*, 30:950–959.
- Özer, E., van Damme, M., Schweckendiek, T., and Jonkman, S. N. (2016). On the importance of analyzing flood defense failures. *FLOODrisk 2016 - 3rd European Conference on Flood Risk Management*.